Summer 2021

Enhancing Plasmonic Nanomaterials: Colorimetric Sensing and SERS

John Crockett
Western Washington University, johnrc5@illinois.edu

Enhancing Plasmonic Nanomaterials:
Colorimetric Sensing and SERS

By

John R. Crockett

Accepted in Partial Completion
of the Requirements for the Degree
Master of Science

ADVISORY COMMITTEE

Dr. Ying Bao, Chair

Dr. Mark Bussell

Dr. Amanda Murphy

GRADUATE SCHOOL

David L. Patrick, Dean

Master's Thesis

In presenting this thesis in partial fulfillment of the requirements for a master's degree at Western Washington University, I grant to Western Washington University the non-exclusive royalty-free right to archive, reproduce, distribute, and display the thesis in any and all forms, including electronic format, via any digital library mechanisms maintained by WWU.

I represent and warrant this is my original work and does not infringe or violate any rights of others. I warrant that I have obtained written permissions from the owner of any third party copyrighted material included in these files.

I acknowledge that I retain ownership rights to the copyright of this work, including but not limited to the right to use all or part of this work in future works, such as articles or books.

Library users are granted permission for individual, research and non-commercial reproduction of this work for educational purposes only. Any further digital posting of this document requires specific permission from the author.

Any copying or publication of this thesis for commercial purposes, or for financial gain, is not allowed without my written permission.

John R. Crockett

8/09/2021

Enhancing Plasmonic Nanomaterials: Colorimetric Sensing and SERS

A Thesis
Presented to
The Faculty of
Western Washington University

In Partial Fulfillment
Of the Requirements for the Degree
Master of Science

by
John R. Crockett
August 2021

Abstract

Nanomaterials, materials with at least one dimension on the nanoscale have become an area of extreme scientific interest due to their many unique properties with applications in catalysis, optics, and sensing, just to name a few. Metal nanoparticles are particularly interesting because of the interactions between light and surface electrons in the metal's conduction band, called localized surface plasmons. In anisotropic metal nanoparticles these plasmons are especially exciting due to the highly responsive quality of the plasmonic resonance associated with their varied nano dimensions. Gold nanorods and nano dendrites in particular exhibit electromagnetic effects which are specifically associated to the shape and environment surrounding the tips of the particles. The singular plasmonic properties of these materials were explored for their properties as signal transducers to enhance detection of metal ions and as signal amplifiers to enhance the production of Raman shifted light from small molecules. Specifically, the first of these projects explored the detection of mercury (II) ions using gold nanorods the surface of which have been modified with polyethylene glycol thiol ligands, this resulted in both a moderate enhancement in ion detection along with significant enhancement of nanoparticle stability. In another project gold nano dendrites were grown under varied conditions to examine how the complexity of the particles could be tuned in order to supplement their use in surface-enhanced Raman Spectroscopy.

Acknowledgements

I would like to thank my parents Linda and Timothy Crockett for their support in what, to them, must often seems a strange endeavor.

When I returned to school I started at my local community college, Centralia College, and I thank the faculty there for giving me an excellent foundation in Chemistry, Math and Physics, most notably Karen Goodwin, Dan Taylor and Michael Threapleton.

I would like to thank the faculty and staff of the chemistry department at Western Washington University. In particular, Dr. Raymond for her good advice and Dr. Emory for being so generous with his time and knowledge.

Dr. Michael Kraft from Sci-Tech for his help in imaging and his innate humanism.

Kyle Mikkelsen from AMSEC for his expert assistance and guidance on a plethora of instruments.

Dr. Hla Win-Piazza for her masterful understanding of all things ^{1}H NMR.

My advisors Dr. Bussell and Dr. Murphy for their excellent advice and depth of knowledge.

My fellow lab mates to whom my gratitude cannot be expressed with words. I will be forever grateful for how welcome I was made to feel at WWU but in the Bao group especially.

Maggie Wang, I will always admire her hard-working nature, her direct attitude, and, most of all, her ability to laugh at herself, a highly under-rated quality in our current culture.

Sullivan Cohen-Pope, a truly kind soul, always taking care of the people around him, involved in the world but not warped by it, and with the capacity to accept the joy in every moment of life.

Eli Doebler, an excellent scientist, an excellent man, I wish we had more time together.

Alexandra Hoff, Eddy Santamaria, Teagan Hamlett, Wynn Wee, Baily Klinger, and Chloe Anderson. Thank you for your hard-work and at least pretending to listen to my rambling explanations.

And, of course, Dr. Bao without whom none of this would have been possible. Thank you for teaching me to be less afraid. Thank you for teaching me to ask for the things I want. Thank you for pushing me to do better than I thought I could. Thank you for helping me in the many small ways to become better, not only at science, but at life.

Table of Contents

List of Tables and Figures

Chapter 1

Metal Anisotropic Nanoparticles

1.1 Introduction to Nanoscales and Nanomaterials

Nanotechnology has the potential to revolutionize every area of human enterprise. Fields being affected by nanotechnology include, drug delivery,[1] optical engineering,[2] communication,[3] and energy storage.[4] Complete understanding of the principles governing nanotechnology requires interdisciplinary work in a broad range of fields, including chemistry, physics, biology, materials science and engineering. The earliest application of this knowledge was the production of computer processors with nanoscale architecture providing massive reductions in computer size and energy requirements.[5] These incredible results led to a slew of scientists and researchers striving to expand our understanding of nanotechnology in other scientific fields in hopes of creating similar groundbreaking discoveries. This thesis is most concerned with the use of nanotechnology in sensing applications, particularly the selective detection of toxic ions and proteins at or below the nanomolar scale. Detecting metal ions at this level will have a profound effect on the monitoring of toxins, particularly those such as mercury (II) ion, which can accumulate in the body over time.[6] The detection of proteins at such small concentrations will allow for the diagnosis of diseases, such as cardiovascular disease[7] or even Alzheimer's,[8] at a much earlier stage when preventative treatment could save lives and memories.

The nano- prefix is used to define a unit which is one-billionth of a meter. It can be difficult to conceptually understand how large such nanoscale objects are in relation to the everyday world. Figure 1.1 shows a map of the continental United States superimposed on a Scanning Transmission Electron Microscopy (STEM) grid (commonly used in analyzing nanoscale materials). If a meter was a nanometer

this STEM grid would have the same surface area as the contiguous United States and a dime would have a surface area about twice that of the land surface of the earth.

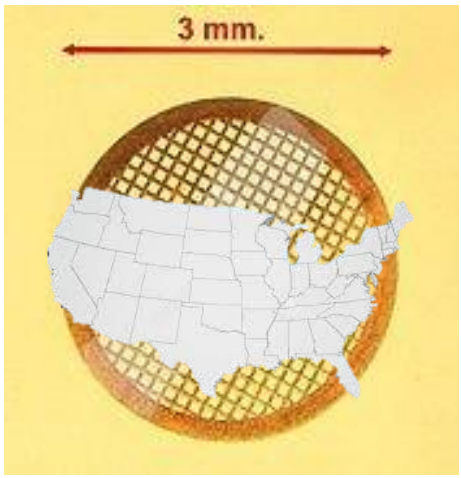

Figure 1.1 A comparison of the surface area of the Continental United States to the surface of a STEM grid.

One of the first developments that came from the study of nanoscale objects was the discovery of nanomaterial properties which are different from their macroscale objects. Nanomaterials are materials that have at least one dimension which is about 100 nm or less. This class of materials include: 1) a thin film which might be 100 nm or less thick but extend in its other dimensions to any size, 2) nanowires which might have diameter of 100nm or less but length extending into the macroscale, 3) nanoparticles with all three dimensions of 100 nm or less.[9] Varying the geometry of the nanomaterials can selectively affect their properties which selectively effects their various applications such as optics,[10] magnetics[11] or chemical reactivity.[12]

Nanoparticles can be composed of many different materials and each of them is useful in different applications, Figure 1.2 shows a variety of organic and inorganic nanoparticles. Organic nanoparticles include lipids, polymers, and proteins such as keratin or chitosan.[13] These nanomaterials are especially common in biomedical applications in due to their biocompatibility,

flexibility in different environments and ability to be easily functionalized with peptides or antibodies for bioconjugation.[14]

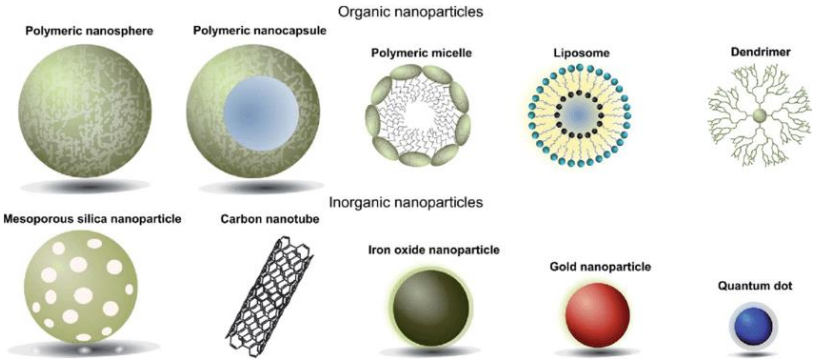

Figure 1.2 Illustration of a variety of different organic and inorganic nanoparticles. Reproduced with permission from Royal Society of Chemistry: Chudasama, V.; Richards, D.; Maruani, A. Antibody Fragments as Nanoparticle Targeting Ligands: A Step in the Right Direction. *Chem. Sci.* **2016**, *8*. https://doi.org/10.1039/C6SC02403C.

Inorganic nanoparticles can be composed of many different materials, such as silicon or iron oxides, carbon nanotubes, or conductive metals such as gold and silver. Inorganic nanoparticles are some of the most interesting as their properties can vary drastically from the properties of their bulk material counterparts. The most direct consequence of creating particles on the nanoscale is the significant increase in the surface to volume ratio of the particle. If particles are composed of oxides, or metals, then the increased surface area will make them more available for catalysis. This can potentially be used to generate a regime between traditional heterogenous and homogenous catalysis tuned to take advantage of the benefits of both methodologies.[15] Beyond the effect of enhanced surface area, nanoparticles also demonstrate many other novel properties. For example, due to their small size iron oxide nanoparticles exhibit unique superparamagnetic properties based on the ability for nanoscale single crystal moieties to be affected by small thermal variations.[11] Noble metal nanoparticles exhibit a host of features such as enhancing the production of Raman scattering, tunable fluorescence, and localized surface plasmons.[9,16]

1.2 Metallic Nanomaterials and Their Anisotropic Features

Among all kinds of nanomaterials, noble metal nanomaterials possess unique properties because of surface plasmon- polaritons, colloquially called surface plasmons. These surface plasmons are the quantum term used to describe the interaction of photons with conduction band electrons on the surface of metal nanomaterials. In objects such as thin metal films this produces an evanescent field which extends a short distance from the metal surface and can be used as a sensor in various applications. In metal nanoparticles these plasmons exhibit a simultaneous displacement of the charge along the particle's nano dimension, as seen in Figure 1.3.[17] Photons of specific wavelength cause oscillations in resonance with the size of the particles called a localized surface plasmon resonance, this produces an increased absorbance for light in those wavelengths. In other words, these particles behave like a short dipole antenna for light in the visible to near-infrared region allowing for a new means for the manipulation of light as well as the exchange of information from between the nano- and macroscales. Wang et al. have explored

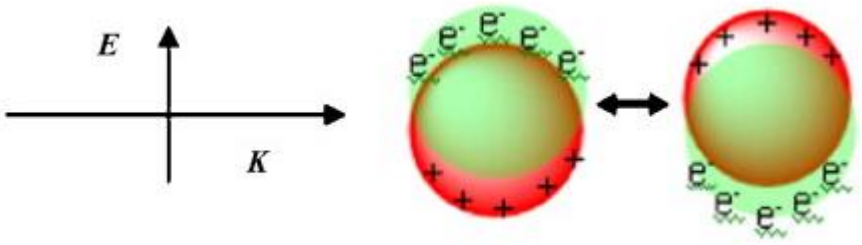

Figure 1.3 A diagram of the localized surface plasmon resonance in a 10 nm gold nanoparticle. Reproduced with permission from: Huang, X.; El-Sayed, M. A. Gold Nanoparticles: Optical Properties and Implementations in Cancer Diagnosis and Photothermal Therapy. *Journal of Advanced Research* **2010**, *1* (1), 13–28. https://doi.org/10.1016/j.jare.2010.02.002.

light manipulation using nanoparticles to devise a new lasing medium, by arranging gold

nanoparticles into arrays on a glass surface they were able not only to manipulate the wavelength of laser light emitted with fine control but to produce a medium with Q-factors in excess of 200[2]. This technology could soon make it possible to drastically reducing the size and energy requirements of any device that uses a laser.

As can be seen in Figure 1.4 the electromagnetic field surrounding a gold nanoparticle demonstrates significant enhancement in the near-field region of the nanoparticle.[18] This property has led to significant interest in uses including drug delivery,[19] surface enhanced Raman spectroscopy (SERS),[20] for chemical mapping of biomaterials,[21] and even light driven catalysis.[22]

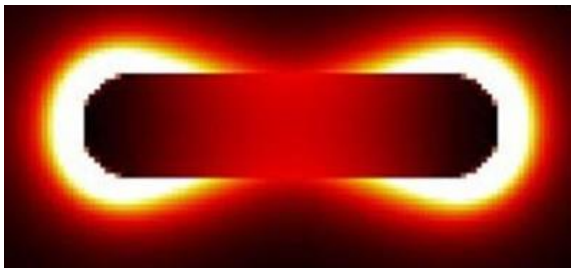

Figure 1.4 A simulation of the electromagnetic field strength surrounding a gold nanorod. Reproduced with permission from: Abbas, A.; Tian, L.; Morrissey, J. J.; Kharasch, E. D.; Singamaneni, S. Hot Spot-Localized Artificial Antibodies for Label-Free Plasmonic Biosensing. *Adv Funct Mater* **2013**, *23* (14), 1789–1797. https://doi.org/10.1002/adfm.201202370.

Anisotropic nanoparticles such as gold nanorods have localized surface plasmon resonances associated with both the transverse and longitudinal plasmon resonance (TSPR and LSPR) as shown in Figure 1.5A each of these resonances also has a distinct absorbance at a specific wavelength as indicated in Figure 1.5B.[23]

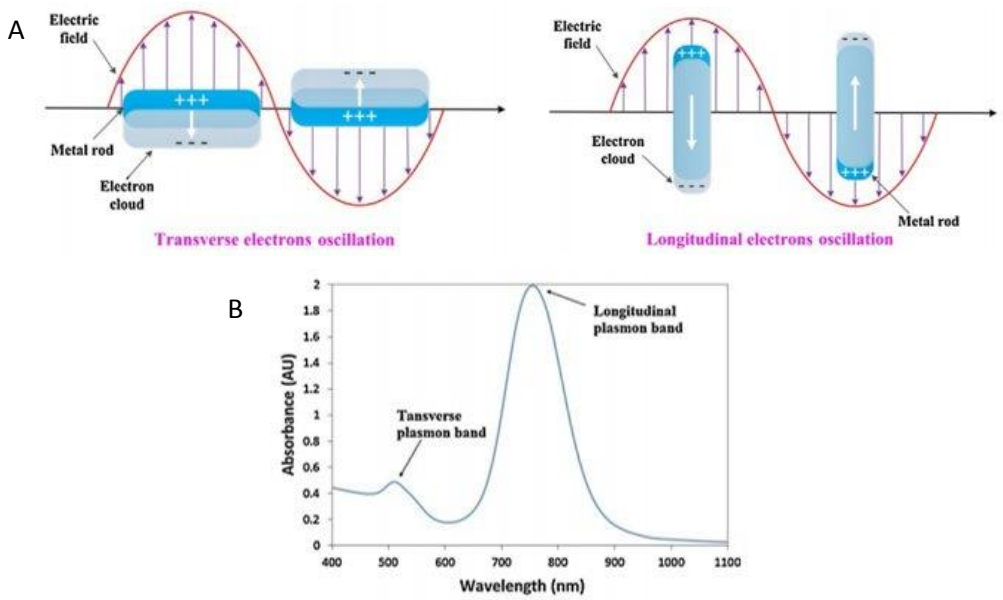

Figure 1.5 A) Transverse (left) and Longitudinal (right) oscillation of electrons in a metal nanorod. B)A plot of wavelength vs. absorbance for a typical solution containing gold nanorods, with the TSPR and LSPR indicated. Reproduced with permission from: Cao, J.; Sun, T.; Grattan, K. T. V. Gold Nanorod-Based Localized Surface Plasmon Resonance Biosensors: A Review. *Sensors and Actuators B: Chemical* **2014**, *195*, 332–351. https://doi.org/10.1016/j.snb.2014.01.056.

1.3 "Bottom Up" Synthetic Methods

The earliest known synthesis of metal nanoparticles was the production of gold nanoparticles by pounding gold into thin sheets and suspending it in molten glass. This technique was used in the 4th century A.D. to produce the well-known Lycurgus Cup (shown in Figure 1.6) and a similar technique has been used for the production of red stained glass up to today.[24] Modern techniques are generally divided into "top down" and "bottom up" synthetic techniques.

"Top down" techniques begin with a large piece of material which is cut down to the nanoscale. This is much like modern machining techniques in which large blanks composed of a material are carved to form shapes such as an engine block. In "top down" nanoscale synthesis this "machining" is usually accomplished using a variety of lithographic techniques, either optical, such as Extreme Ultraviolet Lithography (EUVL)[25] or Ion Beam Lithography (IBL).[26] The benefit of "top down" techniques is the extreme uniformity of the products, the drawbacks include fundamental problems using the technique for 3-dimensional architecture, and a high cost due to low synthetic efficiency.

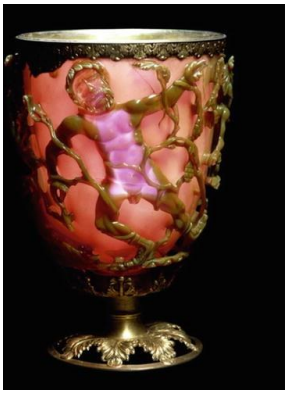

Figure 1.6 The fourth century A.D. Lycurgus cup produced for King Lycurgus of Thrace. Reproduced with permission from: Savage, N. Photonics: Trick of the Light. *Nature* **2013**, *495* (7440), S8–S9. https://doi.org/10.1038/495S8a.

There is also a variety of "bottom up" synthetic techniques such as wet-chemical, electrochemical and photochemical reduction to name a few. In these methods, metal salts are suspended in a colloidal solution (sometimes containing shape directing agents) and reduced to metal using a variety of methods.

In a typical seedless synthesis using photoreduction gold (III) chloroauric acid is solvated with a mixture of cetyltrimethylammonium bromide (CTAB) and tetradodecylammonium bromide (TDAB), acetone and cyclohexane are added to loosen the micellar structure produced by CTAB and TDAB and silver nitrate is added as a shape directing agent, the mixture is then reduced using ultraviolet light (UV) as shown in Figure 1.7A.[27] These techniques were once quite common but have fallen out of favor due to their low synthetic yield, the reliance on undesirable organics such as cyclohexane, and the use of a UV light source.

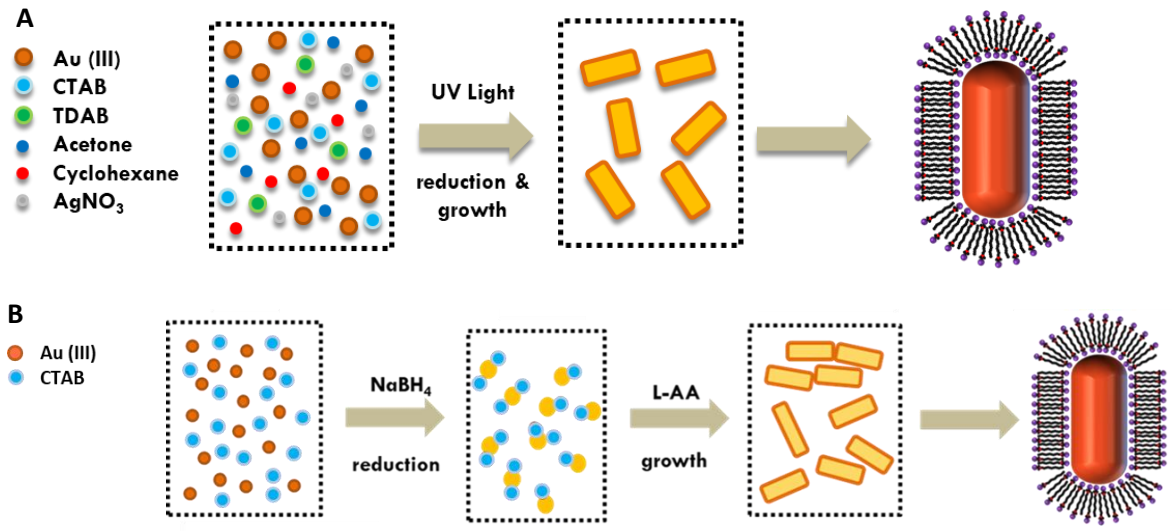

Figure 1.7 A) Schematic illustration of a typical photoreduction synthesis of gold nanorods, **B**) Schematic illustration of a seed-mediated synthesis of gold nanorods.

By far the most common method currently in use for the synthesis of gold nanorods is the seed-mediated method developed by El Sayed et. al. as depicted in Figure 1.7B. In this method gold (III) chloroauric acid is suspended in a CTAB solution at concentration high enough to form rod shaped CTAB micelles and reduced using $NaBH_4$ to produce small gold nanoparticles. These small gold nanoparticles are then used in a growth solution containing gold (III) chloroauric acid in a similar CTAB solution along with silver nitrate, where the silver ion acts as a shape directing

agent by adsorbing onto <100> and <110> gold surfaces resulting in favorable growth of gold in the <111> direction. The gold in the solution is then reduced using ascorbic acid (AA). AA, a relatively weak reducing agent, is further weakened by lowering the pH of the solution with hydrochloric acid, until it is only capable of reducing the gold (III) to gold (I) in solution. On the surface of the gold seeds, however, AA can complete the reduction to gold metal slowly growing them into gold nanorods. This method is preferred because of its high yields and relative chemical simplicity.[28]

1.4 Surface Modification

Surface modification is a useful and often essential tool in the use of metal nanoparticles. A ligand or other stabilizing material is necessary to prevent metal nanoparticles aggregating in solutions or changing shape if deposited on a surface in order to minimize their surface energy. The most common ligand used in the preparation of anisotropic nanoparticles is CTAB which is problematic for biomedical applications as it is highly cytotoxic. CTAB is also problematic due to its tendency to form bilayers which become unstable at low concentrations and to prevent contact with the analyte at high concentrations. Because of these problems most applications for AuNRs require surface modification before use, the most common modification is a ligand exchange.

1.4.1 Ligand Exchange

The process of ligand exchange is quite simple when incorporating molecules containing a thiol moiety due to the strong affinity of sulfur to form bonds with noble metals and particularly gold. All that is required is a to remove as much CTAB as possible without aggregation and then incubate in a solution of for example PEG-thiol for at least 14 hours then thoroughly clean rinse the particles with ethanol to remove any traces of CTAB as show in the Figure 1.8 This exchange produces many benefits, increasing the stability of the gold nanoparticles in a variety of solvents as well as fortifying them against heat induced shape change.[29]

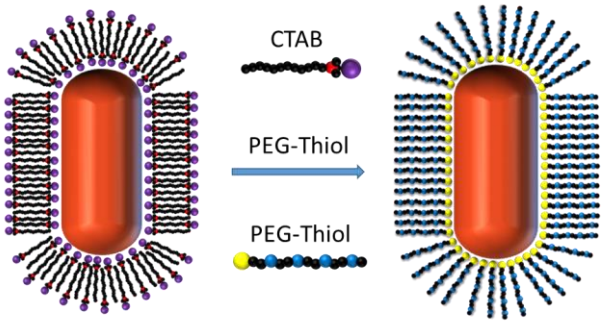

Figure 1.8 Schematic illustrating the exchange of CTAB with PEG-Thiol.

1.4.2 Silica Coating

Silica coated particles have many advantages over traditional ligand stabilized nanoparticles: 1) they are stable in most solvents, 2) they have an easily controllable porosity allowing size selected small molecules to interact with the nanoparticle surface and 3) they are quite simple to synthesize at least in the case of full encapsulation[30] or end encapsulation.

Tips of AuNRs are the most useful area with regards to sensing applications and it is therefore desirable to have a method which exclude materials from the sides of AuNRs. The

benefits of a silica coating have already been elaborated above. If such a coating could be directed to the sides only of AuNRs then it would function perfectly to exclude material from the sides forcing it to interact only with the tips of the AuNRs. As with full silica coating the side coating should enhance stability of the AuNRs in highly ionic environments to which silica is practically inert. Side coating of AuNRs with silica has been previously investigated by several groups using a strategy of partial exchange of CTAB with PEG-Thiol this only produced moderate success having low yields of fully Side-Coated Gold Nanorods (SCAuNR) and having poor reproducibility.[31,32] Recently a new method was proposed in which PEG-disulfide is substituted for PEG-Thiol producing better yields.[33] Both methods rely on the selective exchange of CTAB on the tips of AuNRs with PEG-thiol or PEG-disulfide respectively. In order to make this exchange the surface of AuNR must be relatively depleted of CTAB in order to create space for the PEG to approach the surface. PEG-thiol (5000 MW) being a long thin molecule, with a contour length approximately 31 to 40 nm, (using the segment length calculated by Oesterhelt et.al) [34] and a very high affinity for gold has a low selectivity for the location of exchange onto the AuNR. The weaker bonding larger PEG-disulfide is better directed to the tips of the AuNR where surface curvature will produce a larger space between CTAB molecules as shown in Figure 1.9.[33] The reaction of tetraethylorthosilicate (TEOS) to form silica is favored on the CTAB modified surface over the PEG modified surface and with control of the reactants will forms only on the side of the AuNRs.

These side-coated nanoparticles have been explored for the overgrowth of different metals on the tips of anisotropic particles. Zhu et al. demonstrated that gold nanobipyramids (AuNBP) overgrown with palladium directed to the tips using this method had higher photocatalytic activity than AuNBP fully overgrown with palladium.[32] This should allow the design of catalytic reactors tuned to light in the solar spectrum and thus able to directly absorb sunlight to drive reactions.

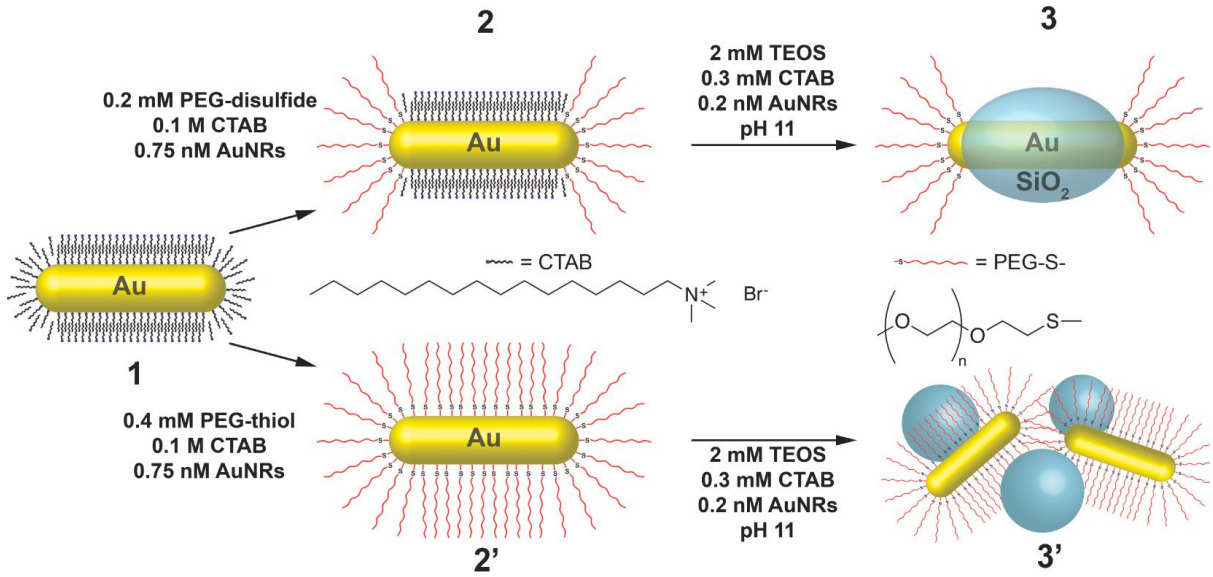

Figure 1.9 Schematic of the site-specific synthesis of a silica coating on gold nanorods using PEG-disulfide. Reproduced with permission from: Hinman, J. G., et.al; Oxidation State of Capping Agent Affects Spatial Reactivity on Gold Nanorods. *J. Am. Chem. Soc.* **2017**, *139* (29), 9851–9854. https://doi.org/10.1021/jacs.7b06391.

1.5 Applications of Anisotropic Metal Nanoparticles

The plasmonic property of metal nanoparticles can be used to enhance sensing or detection in a variety of ways. These can generally be divided into methods in which the material acts as a signal transducer or a signal amplifier. Signal transducers translate information from one domain into another, metal nanoparticles are very effective at transducing information because small

changes over short ranges near the particle surface can change the wavelength or absorbance of the nanoparticle's plasmon resonance. Signal amplifiers act to enhance the intensity of a signal in order to make it more apparent against background noise. The electromagnetic field enhancement surrounding the metal nanoparticles is very strong and can be harnessed to boost the intensity of fluorescence and Raman emissions.

1.5.1 Signal Transducers

Anisotropic metal nanoparticles are most interesting as signal transducers due to the sensitivity of the LSPR associated with their aspect ratio. The LSPR in gold nanorods has sparked interest for several reasons. It is easily adjusted by varying the aspect ratio of the gold nanorods.[35] Also, the plasmonic properties associated with the gold nanorod tips can be changed by materials in near proximity causing the wavelength absorbed by the nanorods to shift quite dramatically. These properties of gold nanorods have led them to be investigated in a myriad of applications for detection of metal ions[36–39] and proteins.[40,41]

A particularly interesting method for manipulating the plasmonic property is the nonpermanent aggregation of the nanoparticles themselves. This aggregation can be adjusted to have different effects from quenching the plasmonic properties of the materials, lowering their absorbance, to combining the plasmons to shift the LSPR of the particles. This is particularly interesting in anisotropic materials if the aggregation can be controlled to select for tip-to-tip attachment. This concept has been explored for the detection of mercury(II) ion by Dr. Merkoçi et.al,[42] AuNRs produced in CTAB, were decorated with a pyrazole-derived amino ligand (PyL)

with high selectivity for binding with mercury (II). Due to the generally accepted property of CTAB@AuNRs to have lower CTAB density on the tips of the AuNRs addition of low amounts

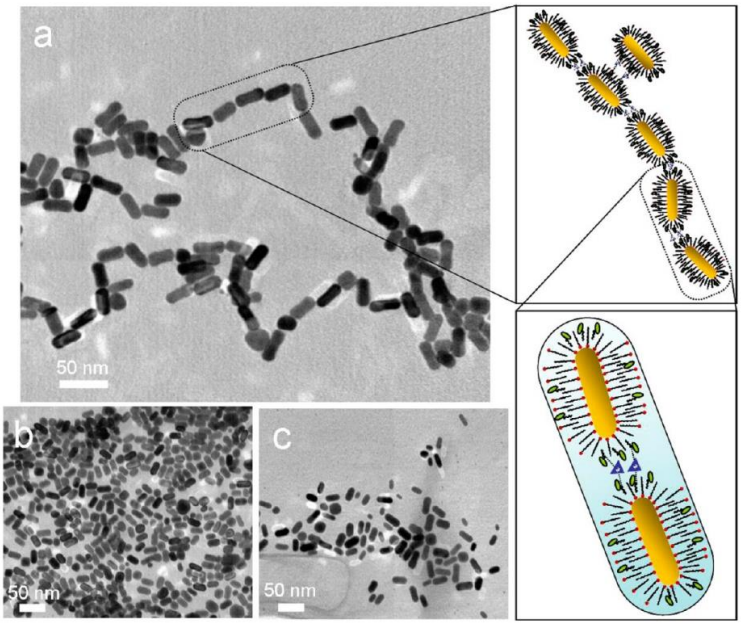

Figure 1.10 a) STEM image of PyL-functionalized AuNRs with 30 ppb $Hg^{2+}$and diagram describing the assembly process b) STEM image of Pyl-functionalized gold nanorods with no Hg^{2+} c) As-prepared AuNRs with 30 ppb Hg^{2+}. Reproduced with permission from Placido, T. et. al; *ACS Appl. Mater. Interfaces* **2013**, *5* (3), 1084–1092.

of PyL will cause it to be located predominantly on the ends, addition of mercury (II) which is captured by PyL located on multiple rods will then cause the gold nanorods to assemble end-to-end as shown in Figure 1.10, above. The subsequent self-assembly will cause the LSPR observed in UV-Vis spectroscopy to shift to much higher wavelength as the particles surface electrons are freed from confinement in the short AuNRs. These PyL decorated AuNR were found to have high sensitivity, 3 ppt of Hg^{2+}, and very good selectivity against competing ions such as copper (II), lead (II), and arsenic (III). Which, although they did present a loss of intensity demonstrated almost no change in resonance wavelength as observed with mercury (II).

Another interesting application of the properties of anisotropic nanoparticles is their possible use as an orientation sensor which could have exciting significance in biological imaging.

It was mentioned above that nanorods have SPR for both the transverse and longitudinal dimensions, which can be excited individually using light of a corresponding wavelength. Link et. al examined both the TSPR and LSPR of gold nanorods and determined that although both could be used to determine orientation the LSPR were superior because of a much higher polarization contrast.[43] They confirmed that the LSPR acts as a single dipole absorber and that the surface plasmon oscillates parallel to the longitudinal orientation of the AuNR. The photothermal intensity of individual AuNRs deposited on a glass surface was observed to increases strongly when the polarization of the light is parallel to the longitudinal axis of the AuNR demonstrating the feasibility of using such a strategy for resolving the orientation of AuNRs. This technique has great potential to leverage AuNRs as an optical probe for the study of the orientation and dynamics of macromolecules, the local structure of synthetic and biological materials, and even the diffusion and conformation of proteins in cells.

1.5.2 Signal Amplifiers

An interesting method for the measurement of energy levels associated with molecular vibrations is the use of Raman light scattering. Raman spectroscopy is unencumbered by many of the issues that vex traditional infrared spectroscopy such as the complicated instrument design required to compensate for the long wavelength of infrared light, and the opacity of glass, and water to infrared light. The significant drawback to Raman spectroscopy is the extremely low intensity of Raman light, only 1 in every 10 million photons is likely to exhibit Raman scattering. It has long been known that molecules adsorbed to a metal surface can demonstrate surface-enhanced Raman (SER) but exploiting the plasmonic properties of metal nanoparticles can boost this enhancement by several orders of magnitude.

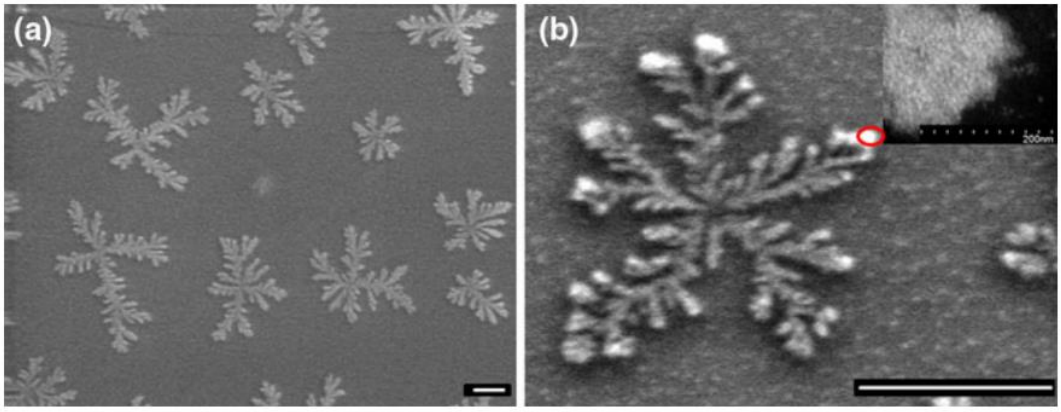

Figure 1.11 a) An SEM image of a group of gold snowflakes, b) a magnified SEM image of a single gold snowflake. Reproduced with permission from: Parab, H.; Jung, C.; Woo, M.-A.; Park, H. G. An anisotropic snowflake-like structural assembly of polymer-capped gold nanoparticles. *J. Nanopart. Res* **2011**, *13* (5), 2173–2180.

One area of interest to produce materials with strong electric field enhancement are dendritic particles often called nanosnowflakes. These particles as seen in Figure 1.11[44] have numerous sharp branches which confine the plasmons moving on the surface of metal particles focusing and intensifying the electric field on the edges and tips of the dendrites. It is of particular interest to produce such materials efficiently and with control of morphology using the "bottom

up" methodologies referred to above rather than the electrochemical methods which have been previously explored.

A relatively recent innovation in nanocomposite particles: nanorattles are nanoparticles composed of a hollow nanocage enclosing a solid nanoparticle. The synthesis of these particles (a simplified scheme shown in Figure 1.12[45]) begins with the production of a AuNBPs. The AuNBPs are then overgrown with silver and the resulting silver overgrown gold nanobipyramidals (Ag@AuNBPs) are then heated to boiling and subjected to a slow galvanic exchange by the

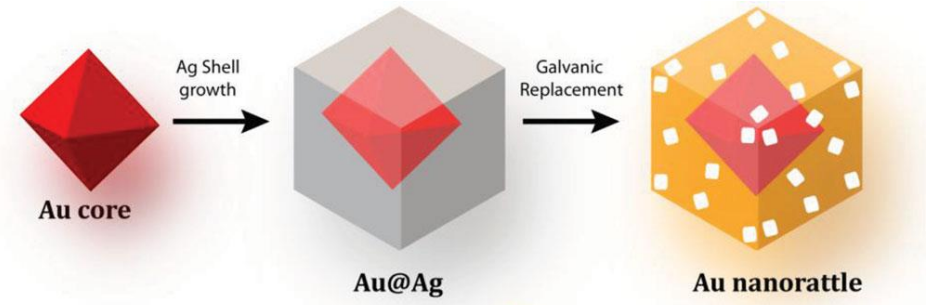

Figure 1.12 A schematic of a typical synthesis for a gold nanorattle. Reproduced with permission from: Jaiswal, A.; Tian, L.; Tadepalli, S.; Liu, K.; Fei, M.; Farrell, M. E.; Pellegrino, P. M.; Singamaneni, S. Plasmonic Nanorattles with Intrinsic Electromagnetic Hot-Spots for Surface Enhanced Raman Scattering. *Small* **2014**, *10* (21), 4287–4292.

addition of gold (III) chloroauric acid. The result is the original AuNBP enclosed in a gold cage the porosity of which can be controlled by the ratio of gold (III) chloroauric acid used in the galvanic exchange. In a galvanic exchange the silver metal atoms are oxidized to Ag (I) by the gold (III) ions as such three silver atoms are required for the complete reduction of every gold atom. If a 1:3 ratio of gold to silver is used in a galvanic reaction, then a solid gold cage is formed. If a higher ratio of gold is used, then the excess gold will rapidly oxidize the silver before it can all be fully reduced leading to a mixed gold ion product and a porous gold shell. These gold cages can produce extreme increases in both the intensity of Raman peaks as well as diminishing the

background fluorescence as observed in Figure 1.13 which shows the enhancement of Raman in Nile Red loaded into gold nanocages.

These AuNRTs have interesting plasmonic properties due to the extreme difference in environment between their exterior and interior surfaces which can be further compounded by the plasmonic properties of the enclosed AuNBP. These properties along with their interior cavity are

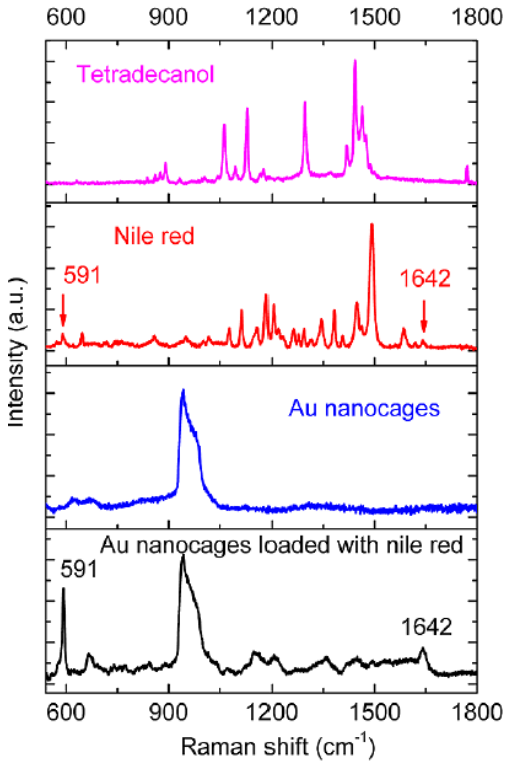

Figure 1.13 a) Raman spectra of Nile Red and Tetradecanol in bulk form along with Au Nanocages with indicated enhancement of Nile Red peaks at 591cm^{-1} and 1642cm^{-1}. Reproduced with permission from: Tian, L. et. al; *ACS Nano* **2013**, *7* (5), 4252–4260.

capable of being loaded with various materials have led to a great deal of interest in using such particles for SERS imaging,[45] drug delivery[19] and photothermal cancer therapies[46]. Some groups have explored combining several of the objects and techniques so far described to build devices which can fulfill multiple goals. Hu et al. have synthesized AuNRTs coated in silica which were then hollowed out to produce a AuNRT in a silica rattler. Thiol capped molecules with high raman

signal were attached to the AuNRT while the the silica was loaded with cancer fighting drugs and decorated with peptides attracted to breast cancer cells. This configuration allowed the location of the particles to be traced using SERS imaging, so that the drug could be delivered to a specific location where it could then be released using the photothermal conversion of near-infrared light. Similar complex structures may soon transform the methodology for treatment of a myriad of diseases[19].

1.6 Challenges and Goals

One of the primary challenges associated with the use of AuNRs for the sensing is the CTAB used in synthetic methods. The CTAB bilayer on the surface of gold nanoparticles acts as a significant barrier preventing particles of interest from approaching near to the surface of the nanoparticle where it can interact with the plasmonic properties of the nanoparticle. Lowering the CTAB concentration to remove the CTAB bilayer is also problematic as the bilayer has a tendency towards sudden collapse rather than gradual removal and this results in permanent aggregation of the AuNRs rendering them useless. Further once the problem of CTAB is overcome either by ligand exchange or surface modification it is still necessary to find a way to direct the analyte of interest towards the tips of the AuNRs where they can cause the strongest change to the LSPR.

This thesis proposes to address these problems by exploring surface modification of gold nanorods first by exchanging CTAB for PEG-thiol on AuNRs used for mercury (II) sensing in order to increase the stability of the gold nanorods and hopefully direct the mercury (II) to the ends of the AuNRs.

Side-specific silica coating will also be explored to enhance stability of the AuNRs while also blocking analytes from interacting on the side of the AuNRs focusing them to the tips. Further

a silica based molecular imprinting technique will be explored for its ability to not only direct material to the sensitive region of the AuNRs but to also select analytes with high specificity.

1.7 Thesis Overview

This thesis research describes work to develop hybrid anisotropic nanoparticles with enhanced plasmonic properties as well as directed surface modification to enhance selectivity and sensitivity to specific analytes. This work is sub-divided into four chapters each dealing with a specific project dealing with enhancing the functionality of anisotropic gold particles for sensing applications.

Chapter 1 focuses on developing an understanding of the fundamental properties of nanomaterials, the formation and properties of composite nanomaterials formed from anisotropic gold nanoparticles as well as the synthesis and plasmonic qualities of anisotropic gold nanoparticles, along with their surface modification. The second chapter explores the properties AuNRs which have been modified with PEG-Thiol. These modified nanoparticles were examined for changes in colloidal stability, as well as sensitivity and selectivity in the detection of mercury (II) ion. Chapter 3 begins with a detailed discussion of the mechanism involved in the formation of site-directed silica formation on AuNRs and AuNBPs using PEG-disulfide in order to form side-coated gold nanoparticles (SCNPs). These SCNP are then used to produce site-specific molecularly imprinted particles. The steps of this formation are examined using a variety of analytical techniques to confirm the location and chemical properties of the imprinted surface sites. These imprinted particles are then investigated for their ability to selectively detect the presence of specific proteins particularly in solution with multiple competing proteins. In chapter 4 the

formation of gold nanosnowflakes is explored with special focus on the mechanism of control for the morphology of fractal features by varying the pH of the synthetic medium.

Chapter 2

Plasmonic Detection of Mercury via Amalgamation on Gold Nanorods Coated with PEG-Thiol

Reproduced with permission from Crockett, J.R.; Plaza-Win, H.; Doebler, J.E.; Luan, T.; Bao, Y. Plasmonic Detection of Mercury via Amalgamation on Gold Nanorods Coated with PEG-Thiol. *ACS Appl. Nano Mater.* **2021**, *4* (2), 1654–1663. https://doi.org/10.1021/acsanm.0c03134.

2.1 Introduction

Mercury, as one of the most toxic metals, is not biodegradable and can accumulate in living organisms, where even trace amounts can accrue to cause damage to brains, kidneys, lungs, and the nervous system. [47–49] Mercury pollution, especially from the water-soluble divalent mercury ion (Hg^{2+}), which is one of the most stable inorganic forms, continues to be a serious issue of concern on the global scale.[50] Great efforts have been devoted to exploring various approaches for monitoring Hg^{2+} in aqueous samples. Currently, various techniques including atomic fluorescence spectroscopy, gas chromatography inductively coupled mass spectrometry, atomic absorption spectrometry, and cold vapor mercury analysis, are available for the determination of Hg^{2+}.[51,52] However, these techniques are restricted by the cost of equipment, complexity of sample pre-treatment and the necessity of a laboratory setting. Therefore, a highly sensitive and

selective approach to detecting Hg^{2+} that avoids the need for advanced instruments is urgently needed.

Due to their sensitive optical response arising from localized surface plasmon resonance, novel metal nanomaterials have been frequently used to construct sensors for detecting Hg^{2+}.[53–55] Among potential sensing techniques, the colorimetric method using metal nanomaterial for Hg^{2+} detection allows the analyte recognition event to be converted to naked-eye sensitive color change and are often favored due to its simplicity, speed, and low cost.[56–60] In order to make the colorimetric detection of Hg^{2+} possible, many studies have applied the aggregation-based method, which relies on Hg^{2+} directly or indirectly changing the distance between metal nanoparticles resulting in a strong plasmon coupling of these metal nanoparticles and a color change in the colloidal solution. DNA, organic molecules and peptides are functional ligands often used to detect Hg^{2+} using the aggregation method.[61–64] For example, mercapto derivatives with sulfhydryl group molecules often functionalize the surface of metal nanoparticles due to the strong Au/Ag-S bond. The introduction of Hg^{2+} will induce the aggregation of nanoparticles by forming interparticle complexes between Hg^{2+} and labelling ligands which then leads to the color change.[65] However, there are intrinsic disadvantages in such methods, including unpredictable auto-aggregation and the necessity of labelling steps on the surface of nanoparticles.

To overcome these issues, the morphology transition-based method has been developed which recognizes the target Hg^{2+} by inducing the surface chemical reaction by a certain analyte. Chen and co-workers demonstrated a novel sensor for Hg^{2+} detection based on the morphology transition of silver nanoprisms modified with thiol ended ligands. In their system, the presence of thiol ligands can protect the stability of silver nanoprisms without Hg^{2+}. When Hg^{2+} is added, the thiol group detached from the surface of silver nanoprisms to form complexes with Hg^{2+},

leading the consumption of silver atoms on the surface by iodine. Eventually, the morphology of particle changed, which can be monitored by the color, and UV-vis absorption spectra of the colloidal solution.[38] Xu and co-worker synthesized gold nanostars and use them as a probe for detecting Hg^{2+}. In this work, the morphology of gold nanostars were deformed due to the formation of Au-Hg amalgamate which changed the localized surface plasmonic resonance of gold nanostars.[66]

For high-sensitivity optical response based on morphology transition, gold nanorods (AuNRs) have shown their superior advantage over others due to their large spectral shift for a given change in their size, aspect ratio (AR) and the refractive index of surrounding media.[67–69] An early example using AuNRs for Hg^{2+} detection is from Rex, et. al. The detection was based on the amalgamation process between mercury and gold. The as-synthesized AuNRs were coated with hexadecyltrimethylammonium bromide (CTAB) ligands. The mercury formed by the reduction of Hg^{2+} initially deposited on the tips of AuNRs due to the low density CTAB packing on the surface of AuNRs, resulting in the decrease of the effective AR of the nanorods. The longitudinal band was highly sensitive for the aspect ratio change, which can be observed as blue shifts.[70] However, due to the nature of CTAB packing on AuNRs, it is known that the stability of CTAB-coated AuNRs (CTAB@AuNRs) is low, which is not ideal for a practical sensor. [67,71] A productive AuNR sensing system would ideally have stable NRs in complex solution as well as have a preferred reaction location on the area of the NR surface that gives the most sensitive plasmonic response. Furthermore, it is advantageous for the region of maximum plasmonic response to be adjustable to the unknown Hg^{2+} concentration.

Herein, the PEG-thiol coated AuNRs (PEG@AuNRs) were fabricated by a simple ligand exchange approach and used as plasmonic nanotransducers to monitor the amalgamation of the

Hg with the AuNRs. Due to the local curvature on the AuNR, the amalgamation occurred preferentially and actively at the rod tips of the PEG@AuNRs which give the most sensitive plasmonic response. The PEG@AuNRs show superior performances, including sensitivity, stability and specificity, over the CTAB@AuNRs. Furthermore, varying both the concentration of overall PEG@AuNRs and the incubation time ($t_{incubation}$) between PEG@AuNRs and Hg^{2+} were used to control the amount of attached PEG-thiol ligands in the system, which impacted the plasmonic responses of PEG@AuNRs toward the same amount of Hg. The mechanism for the strategy based on PEG@AuNRs was proposed and established by the evidence provided via various techniques. We believe that the reported new strategy for detection of Hg^{2+} is promising for constructing a smart Hg^{2+} sensing platform with adjustable peak sensitivity and selectivity.

2.2 Experimental Section

2.2.1 Materials

Hexadecyltrimethylammonium bromide (CTAB), gold (III) chloride trihydrate ($HAuCl_4 \cdot 3H_2O$), L-ascorbic acid (L-AA), hydrochloric acid (HCl), thiolate polyethylene glycol (PEG-SH) (MW 5,000) and ethanol (EtOH) were purchased from Sigma-Aldrich (USA). Sodium borohydride ($NaBH_4$) was purchased from Merck, and silver nitrate ($AgNO_3$) was purchased from Fisher Scientific (USA). Mercury chloride was purchased from Sigma Aldrich (USA). All chemicals were used as received without further purification.

2.2.2 Synthesis of CTAB@AuNRs

The CTAB@AuNRs were synthesized in a large batch via a seed-mediated growth method.[72] To prepare the seeds, 0.250 mL of 0.01 M $HAuCl_4$ was added to 10.0 mL of 0.1 M

CTAB. 0.600 mL of 0.01 M $NaBH_4$ was then added. The solution color changed from orange to light brown, indicating the formation of gold seeds. The solution was stirred for 2 min and left to stand for 2 h. For the growth solution, 450 mL, 0.094 M CTAB aqueous solution was prepared and fully dissolved by putting in a 45 °C water bath. The solution was cooled to room temperature (RT) before further use. 18 mL of 0.01 M $HAuCl_4$ was then added to the surfactant solution and fully mixed by inversion. This was followed by the addition of 2.7 mL of 0.01 M $AgNO_3$ and 2.9 mL of 0.1 M L-AA and the solution was fully mixed by inversion. Finally, 1.8 mL of Au seed solution was added to the mixture and the solution was inverted for 30 s and then left in a dark cabinet at RT for approximately 12 h. Note that the as-synthesized CTAB@AuNRs were first purified by centrifugation twice at 18,000 rpm for 20 minutes in order to remove the redundant CTAB in solution and can then be used for detecting Hg^{2+}.

2.2.3 Ligand exchange with PEG-Thiol

The as-synthesized 40 mL CTAB@AuNR solution was first purified by centrifugation twice at 18,000 rpm for 20 minutes and then re-dispersed in 40 mL nanopure water with 33 mg PEG-Thiol, which was used to replace the CTAB layers on AuNRs. The solution was stirred at RT for 14 hours before it was centrifuged four more times before use. It is important to note that the first two times, the particles were redispersed into ethanol solvent and nanopure water was used as a solvent for the last two times. The final solution volume was 20 mL. The prepared solution was then stored under refrigeration until needed.

2.2.4 Detection method

As a general procedure for detecting Hg^{2+}, 300 µL PEG@AuNRs with a specific concentration was first mixed with different concentrations of 10 µL $HgCl_2$ solution. Depending

on the $t_{incubation}$, 300 μL of fresh ice cold $NaBH_4$ solution was subsequently added into the mixture. The ice-cold $NaBH_4$ solution was prepared by diluting 1mL of 16.5 mM $NaBH_4$ solution with 9 mL chilled water. The final solution was mixed vigorously and left for about 10 to 15 minutes at RT until the color of solution finished changing. To ensure the completion of the amalgamation, the solutions were kept at RT for 20 min before the measurement of the absorption spectrum. Experiments on detecting other metal ions were performed similarly. The concentration of AuNRs was determined by the absorption intensity of longitudinal peak for the solution. The default absorption intensity of AuNRs solution for sensing was about 0.6 abs. (with 1 cm path length).

2.2.5 Characterization

All UV-Vis-NIR spectra for sensitivity and selectivity were recorded with a Jasco UV-VIS-NIR Spectrometer. Scanning Transmission Electron Microscopy (STEM) images of gold nanorods were taken using Jeol 7200 Scanning Electron Microscope in STEM mode. High resolution Transmission Electron Microscopy (HRTEM) images were acquired on a FEI Tecnai Spirit equipped with a Gatan Ultrascan 4000 4k × 4k CCD Camera. Nuclear Magnetic Resonance (NMR) spectra were acquired on a FT-NMR - Bruker Avance III 500 MHz in ^1H NMR mode.

2.3 Results and Discussion

2.3.1 Synthesis, PEG ligand modification and Characterization

The PEG@AuNRs were prepared by mixing PEG-SH with CTAB@AuNRs. After reacting the thiol group of PEG with the surface of AuNRs for 14 h at RT, CTAB was removed by repeated washing and centrifugation with ethanol and water, as depicted in Figure 2.1a. The absorption spectra of AuNR solution before and after ligand exchange were measured (Figure 2.1b). The as-prepared CTAB@AuNR solution (the blue line) has two absorption peaks at 510 and 770 nm that are assigned to the transverse localized surface plasmonic resonance (TSPR) and longitudinal localized surface plasmonic resonance (LSPR) bands of AuNR, respectively. When functionalized with PEG thiol ligand (the red line), the SP bands of PEG@AuNRs do not have obvious shifts (<5 nm) indicating that PEG@AuNRs were prepared without forming aggregates and similar observations have been reported by others as well.[73] The as-synthesized CTAB@AuNRs and the ligand exchanged PEG@AuNRs were characterized via nuclear

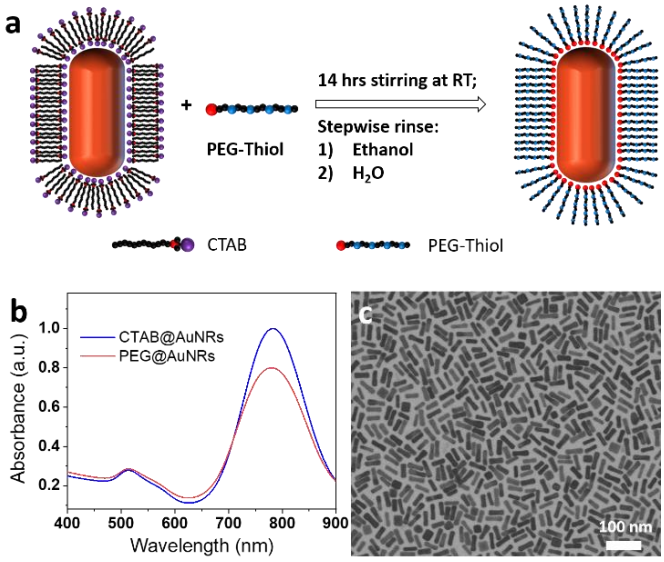

Figure 2.1 (a) Schematic illustration of ligand exchange process between PEG-Thiol ligands and CTAB ligands on the surface of AuNR. (b) UV-Vis absorption spectra of CTAB@AuNRs and PEG@AuNRs. (c) STEM image of PEG@AuNRs after ligand exchange.

magnetic resonance (NMR) spectroscopy. Figure 2.2 and Table 2.1 show ^{1}H NMR spectra of

CTAB@AuNRs (a) and PEG@AuNRs (b) below and the summary of the ^{1}H chemical shifts assignment for CTAB which have been previously reported.[74,75] Comparing the 1H NMR spectrum of CTAB@AuNRs, it is clear that the ^{1}H NMR spectrum of PEG@AuNRs (after

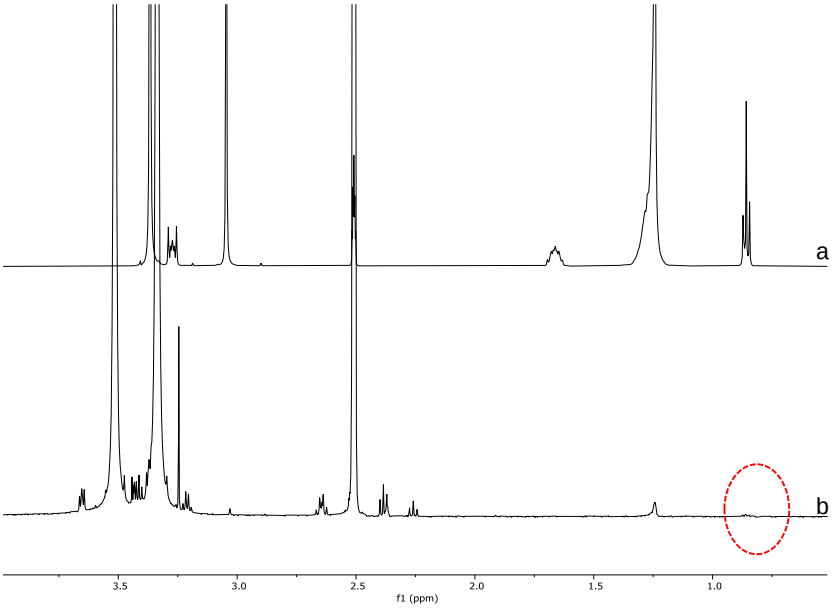

Figure 2.2. 1H NMR spectra of (a) CTAB@AuNR, (b) PEG@AuNR.

Table 2.1. 1H NMR Chemical Shifts in ppm, CTAB-AuNR.

Assignment	CTAB-AuNR (ppm)
1 (CH_2)	3.26
$N(CH_3)_3$ (head group)	3.04
2 (CH_2)	1.66
4 - 15 (CH_2 long chain)	1.24
16 (CH_3)	0.85

ligand exchange process) shows significant disappearance of the CTAB methyl resonance at 0.85 ppm (red dashed circle) and the presence of PEG long chain resonance at 3.5 ppm is clearly

distinguishable. These NMR results demonstrate that the ligand exchange process can significantly replace CTAB with PEG.

STEM analysis confirmed that the PEG@AuNRs remained well-dispersed after the ligand exchange. The STEM images of CTAB@AuNRs and PEG@AuNRs in Figure 2.3 and 2.1c show that the morphology of AuNRs is not impacted during the ligand exchange and majority of nanomaterials have a rod shape, with a small number of cubes produced as well. In addition, from the STEM image, the length and width of the synthesized AuNRs were around 48 ± 5 and 14 ± 2 nm, respectively, with an aspect ratio of 3.6 ± 0.8. It is noticed that the process of ligand exchange decreases AuNR concentration to some extent. Thus, in this study, the LSPR absorption intensity of AuNR solution will be used to represent the concentration of AuNRs in the sensing system.

2.3.2 Comparison of sensitivity, selectivity and stability of PEG@AuNRs and CTAB@AuNRs in mercury sensing

The performances of CTAB@AuNRs and PEG@AuNRs on detecting mercury were compared. The mercury sensing mechanism for both cases is based on the amalgamation process. To trigger this amalgamation process, fresh, ice-cold $NaBH_4$ was employed to reduce Hg^{2+} to Hg^0. Then the Hg^0 diffused on the surface of AuNRs, where it subsequently underwent amalgamation with the AuNRs. It is important to know that the most active sites of the AuNRs were located at their tips,[70,76] where the amalgams formed more efficiently, since the ligands in the tips are relatively loose due to their positive curvature. Therefore, the long axis of the AuNR decreases more drastically due to amalgamation than the short axis, resulting in reduced aspect ratio. On the absorption spectra, this will cause the LSPR to have a blue shift due to the two concomitant effects resulting from the deposition of mercury: alteration of the nanorod surface composition and the shape transition. Based on the relationship between LSPR shifts and concentration of Hg^{2+} ($[Hg^{2+}]$), a detection system for Hg^{2+} can be built.

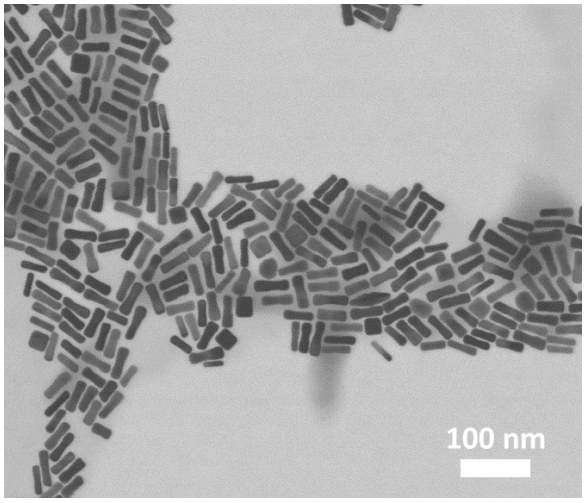

Figure 2.3 STEM images of CTAB@AuNRs

The initial absorption intensities for both CTAB@AuNRs and PEG@AuNRs system are very similar, about 0.62 abs., indicating the very similar concentration of AuNRs in the solutions. As shown in Figure 2.4a and 2.5, for both CTAB@AuNRs and PEG@AuNRs, with the increases of [Hg^{2+}] ranging from 0 nM up to 3690 nM, the LSPR peak shows a continuous blue shift (shorter wavelength) while the TSPR peak is almost fixed at ~510 nm. Thus, the

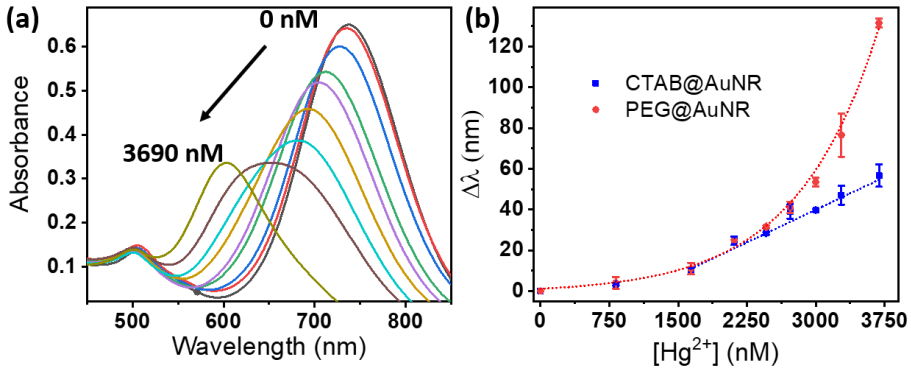

Figure 2.4 (a) Spectra of PEG@AuNR amalgamated under various concentration of Hg^{2+}: 0 nM (black), 820 nM (red), 1640 nM (blue), 1900 nM (green), 2460 nM (purple), 2720 nM (orange), 3000 nM (aquamarine), 3280 nM (brown) to 3690 nM (gold), respectively. (b) Plots of the mean of LSPR shifts for PEG@AuNR and CTAB@AuNR as function of concentration of Hg^{2+}.

degree of the LSPR shift was used as the response to detect the [Hg^{2+}]. It is worthwhile to mention that in these experiments, AuNR samples were all immersed with Hg^{2+} for less than one minute before fresh ice-cold $NaBH_4$ solution was added and all results were recorded after 10-15 min when the optical responses of the resulting AuNR solution were stable. The spectra at 0 nM Hg^{2+} for both CTAB@AuNRs and PEG@AuNRs were measured from the AuNRs mixed with $NaBH_4$, which results in a blue-shifted LSPR. From the collected spectra over the range of [Hg^{2+}], the LSPR peak of CTAB@AuNRs started at 750 nm with 0 nM Hg^{2+} and shifted to 695

nm when at 3690 nM Hg^{2+}. In contrast, the PEG@AuNRs solution shows a larger shift range, from 780 nm using 0 nM Hg^{2+} to 600 nm when using 3960 nM Hg^{2+}.

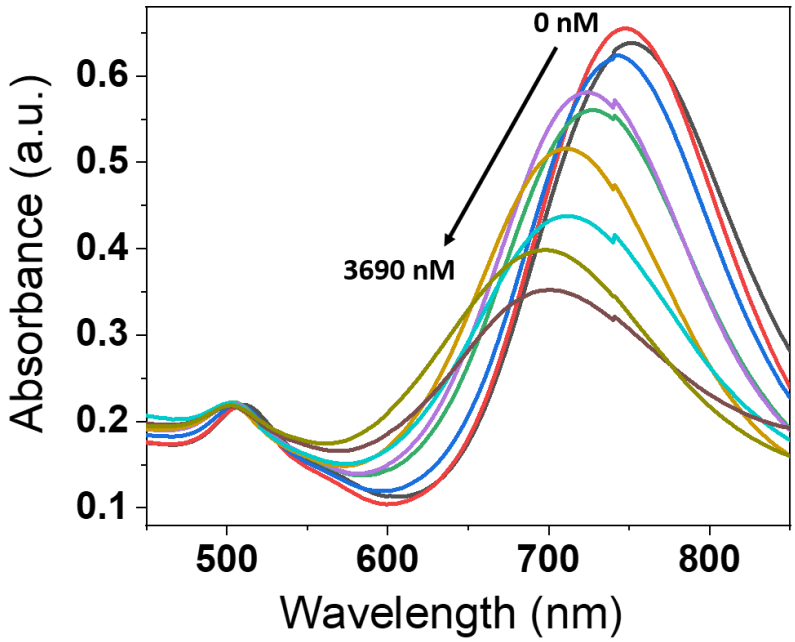

Figure 2.5. Spectra of the LSPR for CTAB@AuNR reduced with mercury (II) chloride from 0 nM (black) to 3690 nM (second of last lowest).

Figure 2.4b summarizes the mean of the LSPR shift of the CTAB@AuNRs solution (blue line) and the PEG@AuNRs solution (red line) based on three trials as a function of [Hg^{2+}] for each system. The $\Delta\lambda$ is defined as the LSPR wavelength change relative to its corresponding initial reference value (at 0 mM Hg^{2+}). At the lower concentrations ranging from 0 nM to 1640 nM, the optical responses for both CTAB@AuNRs and PEG@AuNRs are linear. However, as the [Hg^{2+}] increases, the optical responses of the CTAB@AuNRs and PEG@AuNRs systems show an interesting deviation. For the CTAB@AuNRs system, a linear response with an R^2=0.99 was obtained for measurements performed in the 1640 to 3690 nM Hg^{2+} range. In comparison, the PEG@AuNRs system shows exponential change (R^2=0.99) as a function of [Hg^{2+}], demonstrating a much higher sensitivity to changes in this [Hg^{2+}] range. Note that at higher

concentrations (>3690 nM), the Δλ reaches a plateau and barely changes, which will be discussed further later. Thus, the AuNRs have disparate performance with different ligands, suggesting the vital role of these ligands on sensing systems.

One distinct difference between CTAB@AuNRs and PEG@AuNRs is that the surface of AuNRs has a double layer of CTAB or single layer of PEG, respectively, as shown in Figure 2.1a. It is possible that this difference in density of ligands around the AuNRs impacts their relative detecting performance due to unequal accessibility. The ligands around the surface of the AuNRs impede Hg^0 from accessing the surface and the ligand density is higher for CTAB@AuNRs. Additionally there must be a certain number of free CTAB molecules in the CTAB@AuNRs colloidal solution as the outer layer of the CTAB bilayer must continuously exchange dynamically in order to stabilize the AuNRs.[22] It is possible that the surface of the AuNRs is covered by ligands even as the amalgamation process disrupts the initial packed ligands on the AuNR surface. Thus, the optical response of CTAB@AuNRs is linear to the additional $[Hg^{2+}]$. However, in the case of PEG@AuNRs solution, the density of the PEG around the AuNR surface is lower than with CTAB due to the single layer. Thus, the contact area between mercury and gold surface is larger, resulting in significant higher amalgamation rates as reported elsewhere.[77] With higher concentrations of additional Hg^{2+}, there is a larger extent of amalgamation reactions resulting in a larger optical response of AuNRs.

Figure 2.6a shows images of PEG@AuNRs (top) and CTAB@AuNRs (bottom) solutions after reacting with the same ranges of $[Hg^{2+}]$, showing the transition of the solutions' color from red (right, low $[Hg^{2+}]$) toward green (left, high $[Hg^{2+}]$) which is well-correlated with the observed spectral change as seen in Figure 2.4a. These photos were taken one day after the reaction finished. The PEG@AuNRs system solutions have clear differences in color, are still

very well dispersed, and have no aggregation formed, while the CTAB@AuNRs system solutions formed aggregates which precipitated out of the solution leaving the solution colors very pale. These results are not surprising since it is well known that PEG-modified AuNRs are more stable under various conditions than CTAB-modified AuNRs, as claimed in other studies.[73,78]

To further study the specificity performance of CTAB@AuNRs and PEG@AuNRs for the determination of Hg^{2+}, some inorganic metal ions were tested under the same experimental conditions, including Ag^{+}, Ba^{2+}, Cr^{3+}, Fe^{2+}, and Na^{+}. The inorganic metal ions selected for use in this paper are commonly used in the literature as interference ions and were chosen to be consistent with related works.[66,79] The same amount of CTAB@AuNR and PEG@AuNR were both exposed to 3280 nM solutions of each of those metal ions as well as Hg^{2+}, and 0.8 mM $NaBH_4$ solution was then added. Results are shown in Figure 2.6b. Each column represents the $\Delta\lambda$ averaged over three trials. Note that the added ions were mixed with AuNRs less than one minute before adding $NaBH_4$. In the sensing system of PEG@AuNRs (red bar), the addition of Hg^{2+} causes a large shift of 71 nm, while there are no obvious shifts in the presence of other

metal ions. This indicates the high selectivity against Hg^{2+} making PEG@AuNRs reliable for determination of Hg^{2+} in complex samples.

We observed that the CTAB@AuNRs system exhibits dramatic shifts to several metal ions. It is not surprising that the system has the largest blue shift, about 57 nm, for Hg^{2+} due to the amalgamation-caused morphology change of AuNRs. Additionally, the LSPR of

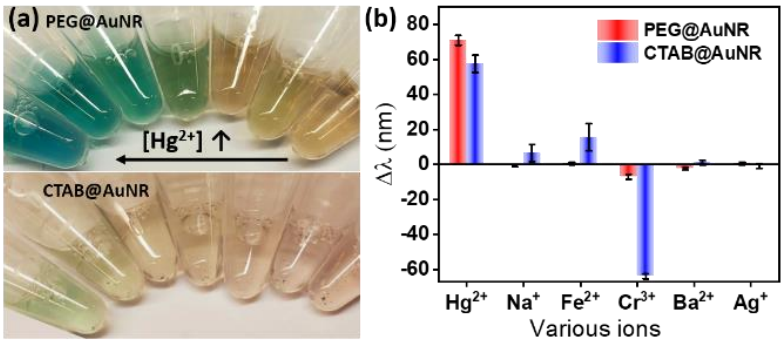

Figure 2.6 (a) Images of the AuNR solutions after reduction with mercury, PEG@AuNR (Top) CTAB@AuNR (Bottom). Concentration of Hg^{2+} from right to left in each tubes are: 0 nM, 820 nM, 1640 nM, 1900 nM, 2460 nM, 2720 nM, and 3280 nM, respectively. (b) Selectivity of CTAB@AuNR and PEG@AuNR against indicated ions (all concentration is 3280 nM).

CTAB@AuNRs has a similarly-sized red shift, about -64 nm, for Cr^{3+}. This is possible because the Cr^{3+} can coordinate with nitrogen in the CTAB capping ligand on AuNRs, inducing the aggregation of AuNRs, resulting in the significant red shift. Further evidence of this is that the corresponding solution of CTAB@AuNRs turns to purple after mixing with Cr^{3+} indicating the aggregation of AuNRs. Furthermore, it is noteworthy that the standard deviations of $\Delta\lambda$ shifts in CTAB@AuNRs system are much larger than PEG@AuNRs system, particularly for Hg^{2+}, Na^{+} and Fe^{2+}. We believe that the amount of free CTAB in the CTAB@AuNR solution will impact the reproducibility of each trial and it is challenging to obtaining accurate concentrations of CTAB based on standard procedures. The standard procedure, washing the synthesized

CTAB@AuNRs two times, maintains the CTAB concentration under 0.01 mM but does not allow for more precise control.[67,80]

2.3.3 Manipulating the mercury sensing performance of PEG@GNRs

Dilution impact. Various concentrations of PEG@AuNRs, determined by the LSPR absorption intensity of the solution, were prepared via dilution or concentration processes to study the rates of LSPR shift under a range of $[Hg^{2+}]$ and the results are shown in Figure 2.7a. The maximum $\Delta\lambda$ for all systems were similar, which we call the plateau. The approximate plateau is shown in green shading in Figure 2.7a. The result for the PEG@AuNRs with 0.99 abs., plotted in yellow in Figure 2.7a, shows that the mean of $\Delta\lambda$ follows an exponential increase

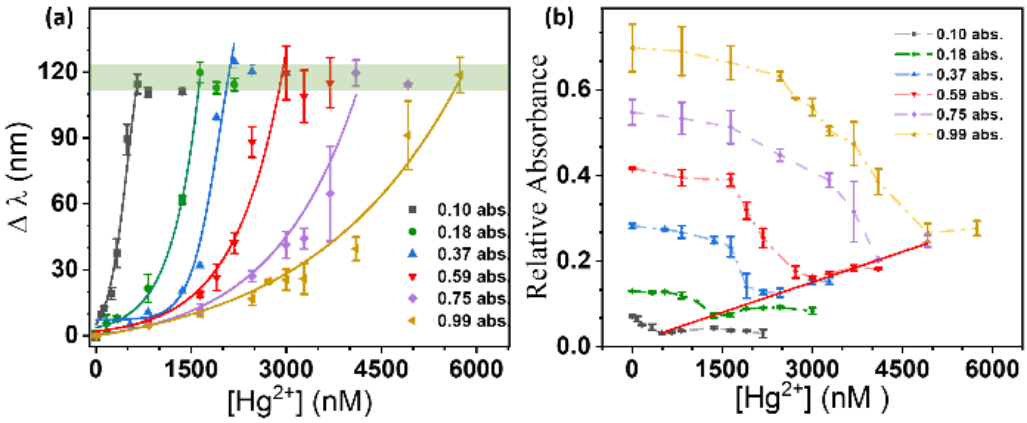

Figure 2.7 (a) Plots of the mean LSPR shifts of PEG@AuNR with various concentration of solutions as the function of $[Hg^{2+}]$. Curves in Figure 2.7a fitted to data before plateau (green shaded area) is reached. (b) Plots of the mean of relative absorbance of PEG@AuNRs solutions against various $[Hg^{2+}]$. The value of relative absorbance is obtained by subtracting the TSPR absorption intensity from the LSPR absorption intensity of the spectrum. The red curve is the linear fitting of the lowest point on each absorption solution.

(R^2=0.99) as the function of [Hg^{2+}] grows from 0 nM to 5747 nM. When the concentration of AuNRs decreases to an absorption of 0.75 abs., the mean of $\Delta\lambda$ similarly follows an exponential increase as a function of [Hg^{2+}], though this increase is faster than before and the plateau is reached around 4100 nM, as is shown in purple in Figure 2.7a. With further diluting of the AuNRs concentration, the rate of change continues to have an exponential relationship with [Hg^{2+}], though the growth rate is faster, and the plateau is reached at increasingly low levels of [Hg^{2+}]. Note that the curves in Figure 2.7a were only fitted to data before the plateau was reached for each system in order to clearly illustrate the relationships between [Hg^{2+}] and $\Delta\lambda$ in the regions where $\Delta\lambda$ is changing. Figure 2.7 indicates that a region of high sensitivity to changes in [Hg^{2+}] can be selected by adjusting the concentration of AuNRs appropriately. The reason for $\Delta\lambda$ reaching its "plateau" quicker when the AuNR concentration is lower was mentioned above. With lower concentration of AuNRs, and the same amount of Hg^{2+}, there will be more amalgamation of each individual nanorod. The consistent maximum $\Delta\lambda$ (the "plateau") indicates that the final shape of individual AuNRs due to the impact of amalgamation is the same regardless of the concentration of the AuNRs in solution if [Hg^{2+}] is sufficiently high. In addition, the detection limit of each concentration of PEG@AuNRs were calculated based on the

Table 2.2. Limit of detection for each concentration of PEG@AuNRs

Concentration of PEG@AuNR	Linear Range (Hg^{2+}nM)	Slope (nm/ Hg^{2+}nM)	Blank Standard Deviation (nm)	LOD (μg $HgCl_2$/L)	R^2
0.10 abs	0-330	0.08 ± 0.01	1.8	20	0.882
0.18 abs	0-820	0.025 ± 0.002	2.4	80	0.980
0.37 abs	0-1640	0.019 ± 0.002	2.7	100	0.946
0.59 abs	0-1900	0.011 ± 0.002	1.2	90	0.913
0.75 abs	0-2460	0.008 ± 0.001	0.2	20	0.905
0.99 abs	0-2460	0.0061 ± 0.0005	0.7	90	0.980

equation LOD=3S_blank/slope. The results are summarized in Table 2.2. It is worthwhile to mention that the blank solutions were obtained by mixing the PEG@AuNRs solutions with certain concentrations and the sodium borohydride solution. Overall, the LOD is not much different when changing the NR concentration and there is no trend in LOD changes when increasing the PEG@AuNR concentration.

Figure 2.7b shows the mean difference in relative absorption intensity of amalgamated PEG@AuNRs solutions under various [Hg^{2+}], obtained by subtracting the TSPR absorption intensity from the LSPR absorption intensity of the spectra. This relationship is obtained for

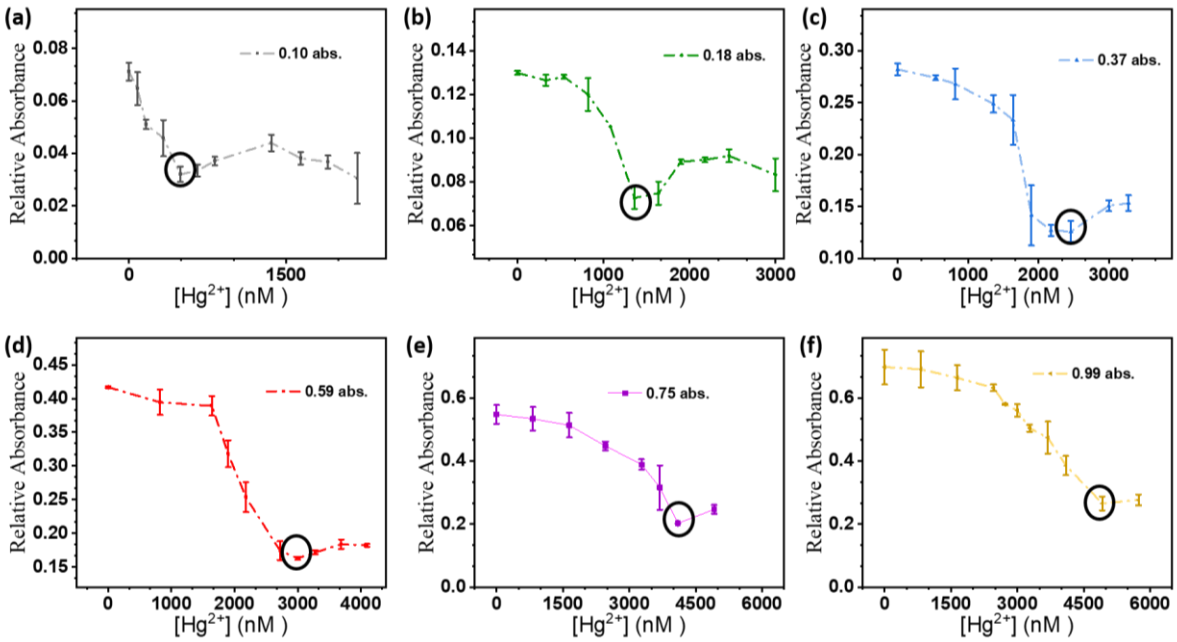

Figure 2.8. Spectra of the change in relative absorbance for PEG@AuNR at different concentrations (as indicated) under various [Hg^{2+}]: a) from 0 nM to 2180 nM b) from 0 nM to 3000 nM c) from 0 nM to 3280 nM d) from 0 nM to 4100 nM e) from 0 nM to 4920 nM f) from 0 nM to 5740 nM.

systems with differing concentrations of AuNR solution. Each system's results are individually plotted in Figure 2.8. In general, the trend for each system is similar. When increasing [Hg^{2+}],

the difference in TSPR/LSPR absorption intensity initially decreased and then reaches a turning point and begins to increase as [Hg^{2+}] is increased further. The turning point for each system can be more clearly observed in the individual plots in Figure 2.8. We believe that during amalgamation, which is the process of Hg^0 diffusing into the AuNRs and forming Au@Hg nanoalloys, there are two key stages impacting the absorption intensity change. In the early stage, the amalgamation takes place more effectively and preferentially on the tips of the AuNRs, decreasing the aspect ratio of the AuNRs and causing the reduced difference in absorption intensity. This is likely due to the smaller scattering cross section of the Au@Hg nanoalloys. In the later stage, the Hg^0 atoms continuously diffuse into the AuNRs, referred to as the "Swelling effect"[81], driven by the difference in cohesive energy between Hg (0.67 eV/atom) and Au (3.81 eV/atom). Thus, the size of Au@Hg nanoalloys gradually increase, leading to the increased absorption intensity. Interestingly, the turning point for each case, when combined in one plot has a linear relationship (R^2=0.99) as shown in Figure 4b (red line). This linear fitting is useful in terms of predicting the turning point in any system with different AuNR concentrations.

Incubation impact: sensitivity, specificity. The mercury sensing performance was further manipulated by incubating the PEG@AuNRs with [Hg^{2+}] for differing amounts of time before adding $NaBH_4$. The hypothesis here was that the incubation process changes the density of PEG on the surface of AuNRs due to the complexation of thiol group and Hg^{2+} which impacts the amount of surface of AuNRs exposed to the external environment and eventually impacts the efficiency of amalgamation.

Figure 2.9a plots the results of the mean of $\Delta\lambda$ for PEG@AuNR with different $t_{incubation}$ as the function of concentrations of Hg^{2+}. It clearly reveals that for same concentration of PEG@AuNRs, with a longer $t_{incubation}$, $\Delta\lambda$ is higher for the same level of [Hg^{2+}] and the plateau is

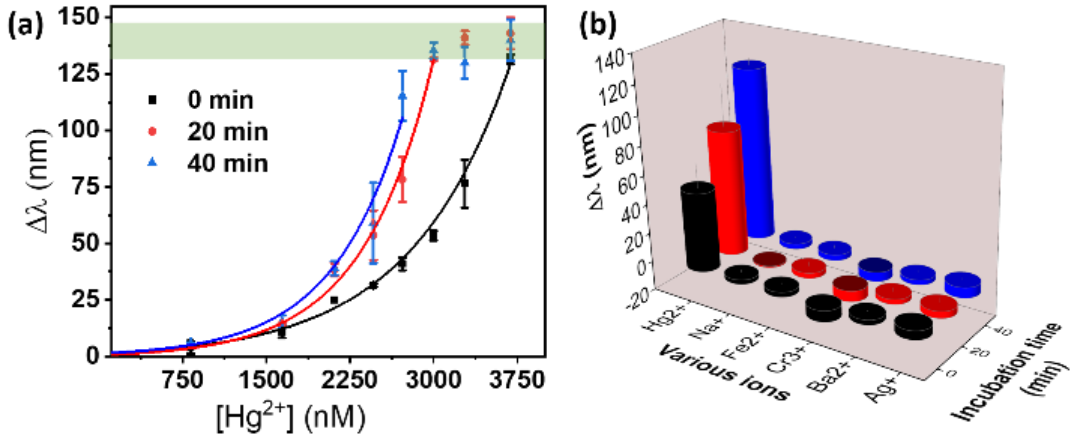

Figure 2.9 (a) Plots of Δλ of PEG@AuNR against the [Hg^{2+}] concentration with 0, 20, and 40 min incubation times based on three trials. Curves in Figure 5a fitted to data before plateau (green shaded area) is reached (b) A comparison of the selectivity of PEG@AuNRs incubated with Hg^{2+}, Na^{+}, Fe^{2+}, Cr^{3+}, Ba^{2+}, and Ag^{+} for 0, 20 and 4 min. (All at concentrations of 2720 nM.)

reached more quickly. Specifically, the PEG@AuNRs with 0 min of $t_{incubation}$ shows an exponential growth (R^2=0.99) and does not show a Δλ plateau in the [Hg^{2+}] range of 0-3690 nM. The PEG@AuNRs with 20 min of $t_{incubation}$ shows an exponential increase of Δλ (R^2=0.99) in the [Hg^{2+}] range of 0-3000 nM, reaching the plateau and not changing as [Hg^{2+}] is increased further from 3000 nM to 3690 nM. For the 40 min of $t_{incubation}$, the [Hg^{2+}] range where Δλ increases to the Δλ plateau is even narrower (0-2720 nM). This result reveals that $t_{incubation}$ can improve the PEG@AuNRs system's sensitivity performance.

The impact of incubation on the specificity of the PEG@AuNRs system toward Hg^{2+} was also examined. We performed experiments to test the influence of the LSPR in the presence of other inorganic ions that were used in Figure 5b, include Ag^{+}, Ba^{2+}, Cr^{3+}, Fe^{2+}, and Na^{+}. Each

column as shown in Figure 2.9b, represents the Δλ averaged over three trials and from the results, only Hg^{2+} caused a significant Δλ, with the other metal ions showing small changes in three cases with various $t_{incubation}$. Among the three cases, the case with 40 min of $t_{incubation}$ shows the highest value of Δλ, about 120 nm, demonstrating the best specificity to Hg^{2+}, while there was a 40 nm change for the case with 0 min of $t_{incubation}$ and an 80 nm change for the case with 20 min of $t_{incubation}$. This implies that the $t_{incubation}$ can amply the specificity to Hg^{2+} while retaining low or no impact from other metal ions.

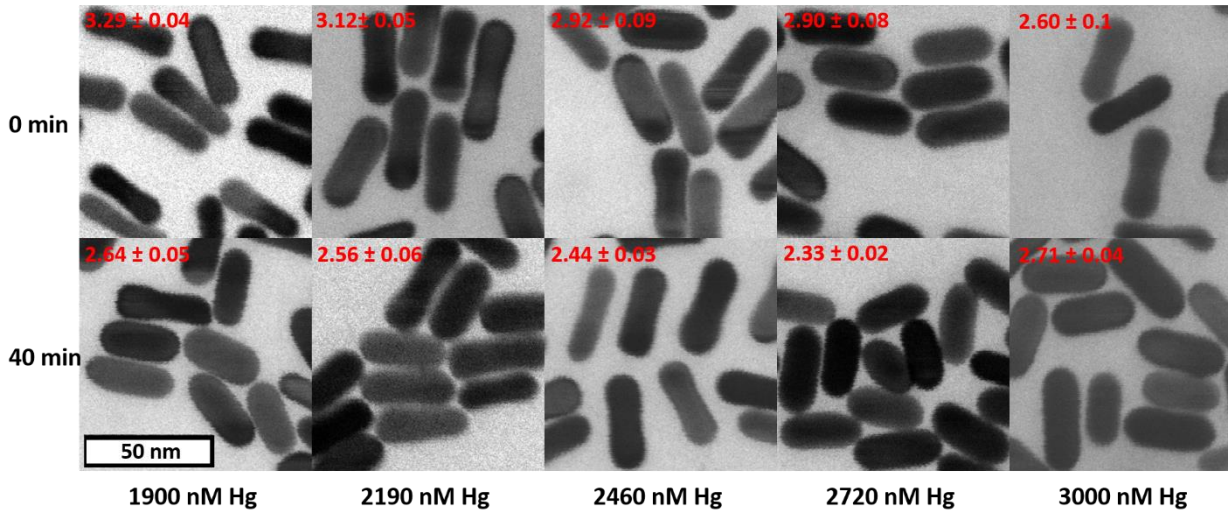

Figure 2.10. STEM images of PEG@AuNR after amalgamation under various concentration of Hg^{2+} for systems with 0 min (top) and 40 min (bottom) incubation time. (Aspect ratio in red determined from sample of at least 300 AuNRs.)

To understand the impact of incubation on the degree of deformation for AuNR morphology under various [Hg^{2+}], STEM was used to characterize the morphologies of PEG@AuNRs after reaction for systems with 0 min and 40 min of $t_{incubation}$. The representative STEM images (Figure 2.10) show the rod shape for both systems with various [Hg^{2+}]. The changes in AR values from increasing the [Hg^{2+}] for two systems are summarized in

Figure2.11a. The data in black represents the AR of the amalgamated PEG@AuNRs from the system where PEG@AuNRs were incubated with Hg^{2+} for 0 min before reduction and subsequent amalgamation, while the data in blue represents the AR of AuNRs from the system where PEG@AuNRs were incubated with Hg^{2+} for 40 min before reduction and subsequent amalgamation.

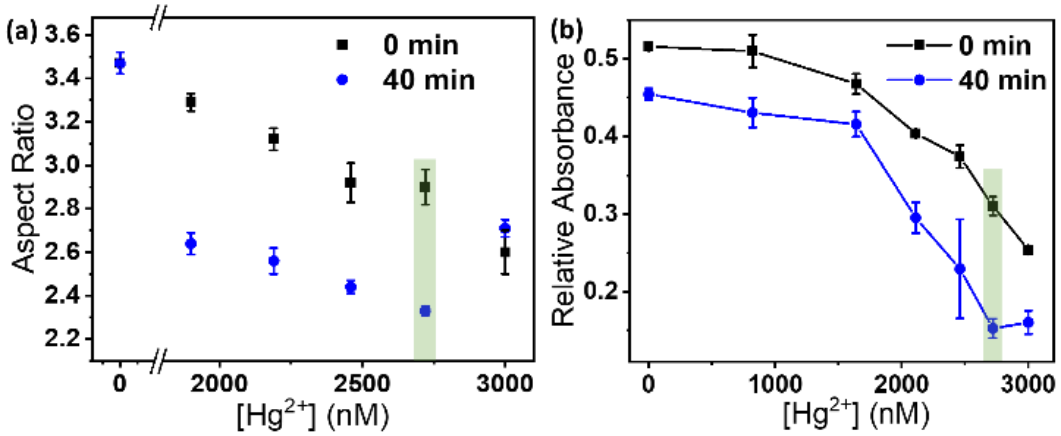

Figure 2.11 (a) The mean of AR value of amalgamated PEG@AuNR against various $[Hg^{2+}]$. (b) The mean of relative absorption intensity of PEG@AuNR solution under various $[Hg^{2+}]$. The value of relative absorbance is obtained by subtracting the TSPR absorption intensity from the LSPR absorption intensity of the spectrum. Green shadow highlights the results for (a) and (b) at 3000 nM $[Hg^{2+}]$ condition.

When the system has 0 nM Hg^{2+}, the $t_{incubation}$ does not impact AR. However, when introducing various amounts of Hg^{2+}, reduced to Hg for amalgamation, the AR values for each system are significantly different. For the system with 0 min of $t_{incubation}$, the AR continuously decreases from 3.47 ± 0.05 to 2.6 ± 0.1 as $[Hg^{2+}]$ is increased from 0 to 3000 nM, while for the system with 40 min of $t_{incubation}$, the AR value decreases from 3.47 ± 0.05 to 2.33 ± 0.02 when

increasing [Hg^{2+}] from 0 to 2720 nM but then increases to 2.71 ± 0.04 as [Hg^{2+}] is increased to 3000 nM.

The process of morphology change was discussed earlier in the context of the absorption intensity change under different [Hg^{2+}], including the initial stage of reducing AuNRs AR and the later stage of gradual size increase due to the diffusing of Hg atoms to the AuNR, referred to as the "Swelling effect". We believe that using the system with 0 min incubation, the range of [Hg^{2+}] used was not large enough to reach the later stage where the aspect ratio increases with increased [Hg^{2+}]. For the system with 40 min incubation, increasing [Hg^{2+}] from 0 to 2720 nM results in a much larger AR decrease than the system with 0 min incubation and then reached the "Swelling effect" stage at 3000 nM [Hg^{2+}] where aspect ratio begins increasing as [Hg^{2+}] increases.

To provide additional evidence for the presence of the "Swelling effect", the mean difference in absorption intensity (obtained by taking the difference of the spectrum's LSPR and TSPR) for amalgamated PEG@AuNRs solutions against various [Hg^{2+}] is plotted in Figure 2.11b. For the system with 0 min incubation (black color), the absorption intensity decreases over the range of Hg^{2+} which is consistent with the decrease of AR. For the system with 40 min incubation (blue color), the absorption intensity decreased initially and then increased starting from [Hg^{2+}] at 2760 nM. At 3000 nM [Hg^{2+}], the absorption intensity increases which matches the change of AR in Figure 2.11a. The green shadow highlights the results that for both systems at 2760 nM [Hg^{2+}] condition.

There are reported works using the AuNR solution based localized surface plasmon resonance for mercury detection. The detection methods include amalgamation[70,82,83] aggregation,[42,84] and surface enhance Raman scattering (SERS).[85,86] Those reported methods have various advantages such as high selectivity and sensitivity. However, there are intrinsic disadvantages to these approaches as well. The reported methods based on amalgamation often use CTAB@AuNRs which have poor stability.[70,82,83] Aggregation based methods are sensitive to ionic interference and the sensing method is highly complex.[42,84] The SERS based detection requires expensive and delicate equipment.[85,86] Our method does not have those drawbacks and is highly stable with straightforward preparation and detection. In addition, our method provides

Table 2.3 A comparison table on AuNR solution based localized surface plasmon resonance between our work and others in literature.

Type	Advantage	Disadvantage	Ref
Amalgamation	pH modification significantly improves sensitivity	CTAB reduces stability Relatively modest selectivity	Q.-Q. Duan, et al 2018 (ref.38)
Amalgamation	Synthetic method possibly reduced standard deviation	CTAB reduces sensitivity of AuNRs to Hg^{2+}	M. Rex, et al, 2006(ref.25)
Amalgamation	High selectivity for LSPR shift High Sensitivity	Very low aspect ratio AuNRs reduce the functional range of sensitivity	L.-H. Jin, et al , 2014 (ref. 39)
Aggregation	Highly sensitive range with very low LOD (ppt)	Absorption intensity is highly affected by other ions	T. Placido et al, 2013 (ref. 40)
Amalgamation and Aggregation	Highly Sensitive	Sensitive to ionic interference Sensing method is highly complex	L. Chen, et al, 2017 (ref.41)
SERS	Extremely good LOD and detection over very low concentration range	Requires expensive and delicate equipment Complicated sensing methodology/device synthesis	A. Yuan, et al, 2019 (ref.42)
SERS	Very Low Detection Limit	Requires expensive and delicate equipment	C. Song, et al, 2017 (ref. 43)
Amalgamation & Thiol Desorption	Highly Stable, Simple method for preparation and detection Broad linear range	High standard deviation of blank results in relatively modest LOD	This Work

broad linear range by changing the concentration of AuNRs or incubation time. See Table 2.3 for a more specific list of advantages and disadvantages of different types of detection methods.

2.3.4 Mechanism

Proposed model. Figure 2.12 shows models of the final morphology of PEG@AuNRs after amalgamation under various values of $t_{incubation}$ and $[Hg^{2+}]$. As depicted in the bottom row of the figure, in the case of low $t_{incubation}$ (such as 0 min) as the $[Hg^{2+}]$ increases, the morphology of the AuNRs moves from a first stage where the AR of the AuNRs is reduced because of amalgamation on the tips of the rods, to a second stage of gradual size increases due to the continuous diffusion of Hg atoms into the AuNRs, leading to an increasing number of atoms per cluster[77,87] . With additional incubation time, the ligand density on the AuNRs will be decreased due to detachment of thiol group by Hg^{2+}. It is well known that an exceptionally strong complex can be formed between Hg^{2+} and sulfur (-S) or thiol (-SH) functional groups.[88–90] The stability constants (log K_f), an equilibrium constant for the formation of a complex in solution, are often used to measure the strength of the interaction between a metal ion with a ligand. It is reported that the log K_f of Hg(SCN)N is about 22, which is larger than that of Au(SCN)N.[91] -SCN is similar to -SH in that it can bind strongly onto the surface of Au nanomaterial.[92,93] Thus, it is reasonable to propose that PEG-thiol, which was initially chemisorbed on the surface of the AuNRs, will be partially removed and complexed with Hg^{2+}. Due to the high-energy surfaces on the tip (curved part) of the AuNRs, PEG-thiol on those locations will be removed first. The first model in both rows in Figure 2.12 indicates the PEG@AuNRs after incubation for a certain amount of time. The model in the top row has less PEG-thiol on the tip comparing to the model in bottom row due to the longer incubation time. With less PEG-thiol on the tip, this increases

the accessibility of free Hg^{2+} (in complex with thiol group) to the surface of the AuNRs and results in a significantly higher amalgamation rate. As shown in Figure 2.12, the more PEG-thiol ligands are removed from AuNR through increased $t_{incubation}$, the a higher degree of amalgamation process will happen under any given $[Hg^{2+}]$, causing additional reduction of the AuNR aspect ratio, which is then reflected in a higher sensitivity of AuNR. It also results in a faster transition from stage one to stage two for the same range of $[Hg^{2+}]$ as indicated by comparing the top and bottom rows of Figure 2.12 for any amount of $[Hg^{2+}]$.

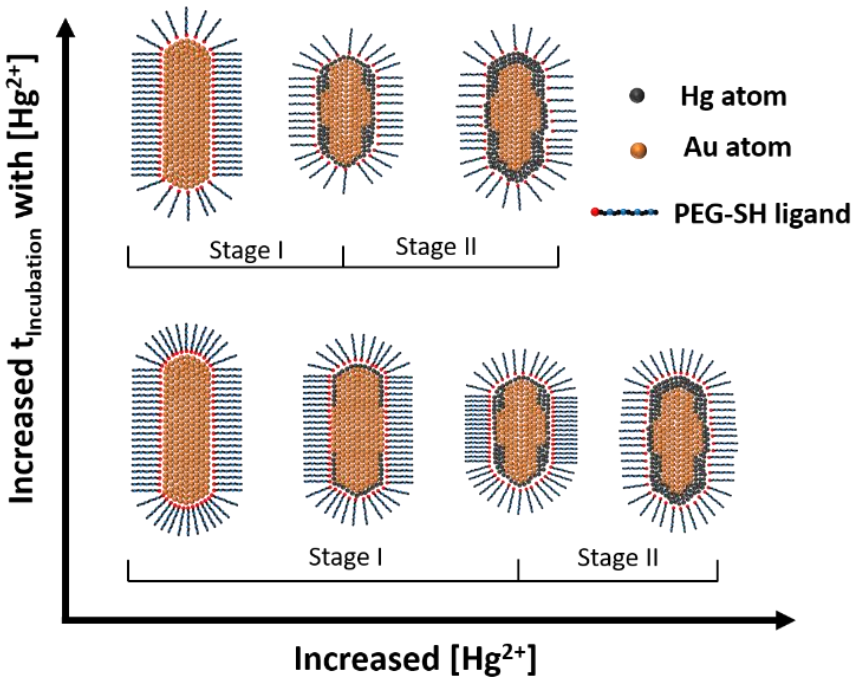

Figure 2.12. Illustration of the final morphology of PEG@AuNR after amalgamation under various values of $t_{incubation}$ and $[Hg^{2+}]$. (not to scale) The following two stages will appear as Hg^{2+} concentration increases. Stage I: diffusion of Hg atoms into AuNRs, shortening or rounding the particle; Stage II: diffusion of Hg atoms into AuNR, gradual increasing the size due to an increase of number of atoms per cluster. With more ligands on the surface of AuNR, the amalgamated PEG@AuNR will stay in stage I through higher $[Hg^{2+}]$.

Electron Microscopy. To investigate the interactions of Hg^{2+} and PEG@AuNRs, and especially to understand the impact of the removal of PEG-thiol on the crystalline structure of AuNRs, PEG@AuNRs with and without Hg^{2+} incubation were characterized by HRTEM. As shown in Figure 2.13a, the PEG@AuNRs without Hg^{2+} incubation exhibit a highly consistent lattice fringe, indicating their monocrystalline structure. The lattice spacing distance of ~0.205/0.204 nm throughout the AuNRs corresponds to (200) facet of gold materials, consistent with other reports.[94] With Hg^{2+} incubation for 40 min, the lattice spacings for (200) planes at the tip and near the curved edge were slightly increase to 0.212 nm as indicated in Figure 2.13b,

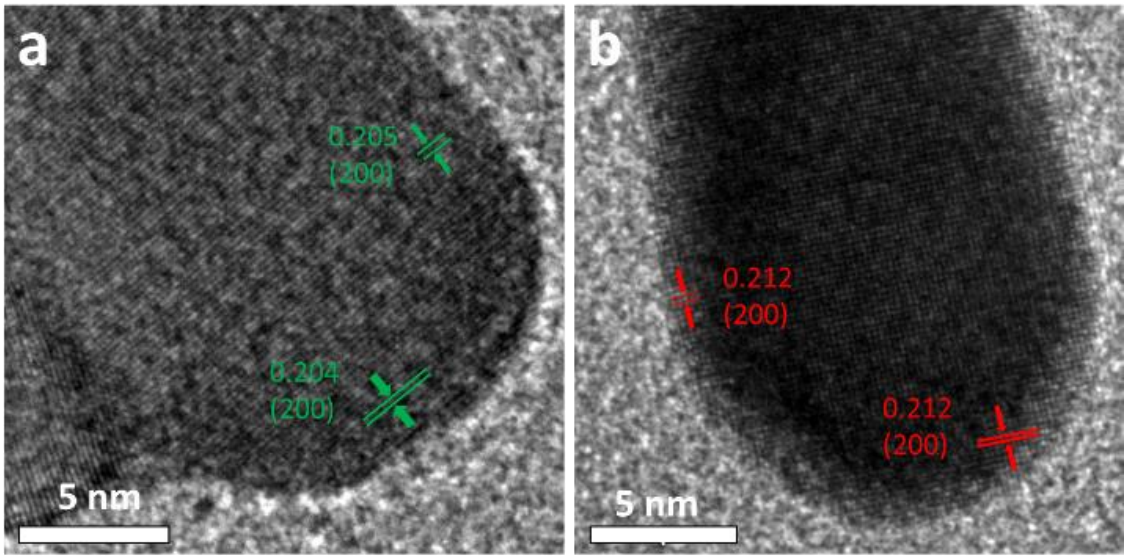

Figure 2.13. HRTEM images of (a) PEG@AuNR without incubation and (b) PEG@AuNR incubated with 1640 nM Hg^{2+} for 40 minutes.

which should be attributed to the Au-SH bond being broken by the Hg^{2+}. Such lattice distortion is likely attributable to the fluctuation of surface ligands, and similar observations have been reported elsewhere.[95–97] In addition, due to the higher activity levels, such interactions

selectively occur at the edge and tips of the AuNRs, facilitating higher sensitivity for Hg^{2+} detection.

Nuclear Magnetic Resonance. NMR spectroscopy is widely used to study the surface chemistry of gold nanoparticles.[98,99] In this work, we used NMR techniques to characterize the complexation between Hg^{2+} and PEG-SH removed from the surface of PEG@AuNRs. The NMR sample of PEG@AuNR was washed with water and titrated with $HgCl_2$ to determine the ability of PEG to adsorb onto $HgCl_2$. Figure 2.14 shows the ^1H NMR spectra for free PEG-thiol ligands

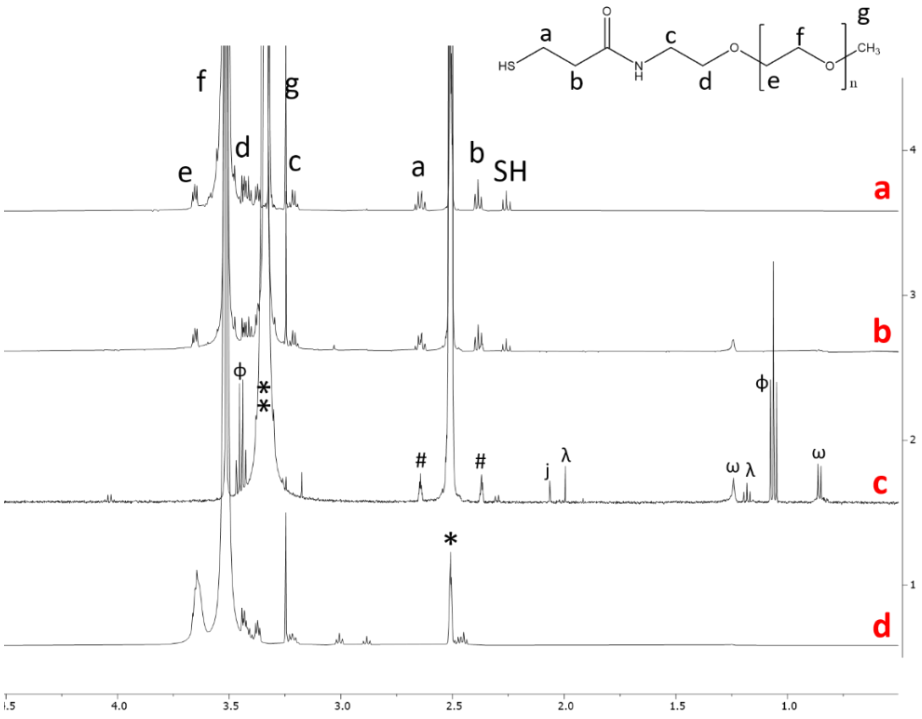

Figure 2.14. ^1H NMR spectra of (a) Free PEG (20.2 mg), (b) PEG@AuNR (c) $HgCl_2$-PEG* obtained by adding 1.1 mg of $HgCl_2$ to PEG@AuNR (d) $HgCl_2$-PEG# obtained by adding 2.0 mg of $HgCl_2$ to free PEG (43.15 mg) in DMSO-d6. Note *DMSO-d6 solvent, and # is 13C satellite from DMSO-d6, ** is a signal for HDO, and other solvent impurities form j acetone, λ ethyl acetate, Φethanol and ω grease.

(20.2 mg), PEG@AuNR, $HgCl_2$-PEG* solution, and $HgCl_2$-PEG# solution in DMSO-d6. Table

2.4 contains the summary of the ^{1}H NMR spectral assignments. It is worthwhile to mention that prior to the NMR spectral acquisitions, all PEG@AuNRs samples were washed with ethanol twice, water twice, and DMSO-d6 once, and then redispersed into DMSO-d6 in order to remove

Table 2.4. ^{1}H NMR Chemical Shifts in ppm, Line Widths, and Assignments for PEG and AuNR-PEG, $HgCl_2$-PEG* and $HgCl_2$-PEG$^{\#}$.

Assignment	PEG[a, b]	AuNR-PEG[a, b]	$HgCl_2$-PEG*	$HgCl_2$-PEG[#, a,b]
SH (thiol, t)	2.25 (1.37)	2.26 (1.66)		
a (CH_2, q)	2.64 (1.53)	2.64 (1.66)		3.00 (t) (2.30); 2.88 (t) (2.2
b (CH_2, t)	2.38 (1.68)	2.39 (1.53)		2.46 (m) (2.29)
c (CH_2, q)	3.21 (1.79)	3.21 (1.35)		3.21 (2.30)
d (CH_2, m)	3.42 (1.48)	3.37 (1.22)		3.43 (1.68)
e (CH_2, m)	3.66 (1.48)	3.65 (1.66)		3.64 (2.30)
f (CH_2, long chain)	3.51 (1.98)	3.52 (1.35)	redu. Int	3.52 (2.91)
g (CH_3, s)	3.25 (1.22)	3.24 (0.92)	redu. Int	3.24 (1.37)

[a] Proton chemical shifts are in ppm, [b] full width at half-maximum (fwhm) line with is in Hz. Peak multiplicity singlet (s), triplet (t), quartet (q), multiplet (m). ^{1}H NMR chemical shifts for $HgCl_2$-PEG* is from Figure 3c and $HgCl_2$-PEG$^{\#}$ is from Figure 8. Reduced intensity (redu. Int.)

excess or unbonded ligands in the solution. The $HgCl_2$-PEG* solution was the supernatant of a mixture of 1.1 mg $HgCl_2$ and PEG@AuNR (5 times higher concentration than in the synthesized solution) which was mixed overnight. As shown in Figure 2.15, after incubating the $HgCl_2$ and PEG@AuNR overnight, the mixture solution changes from a well dispersed brownish red color (Figure 2.15a) to transparent with precipitates formed at the bottom (Figure 2.15b), indicating the detachment of PEG thiol ligands from the AuNRs causing the precipitation of AuNRs. The mixture solution then was centrifuged and the supernatant $HgCl_2$-PEG* was used for 1H NMRanalysis. $HgCl_2$-PEG# solution

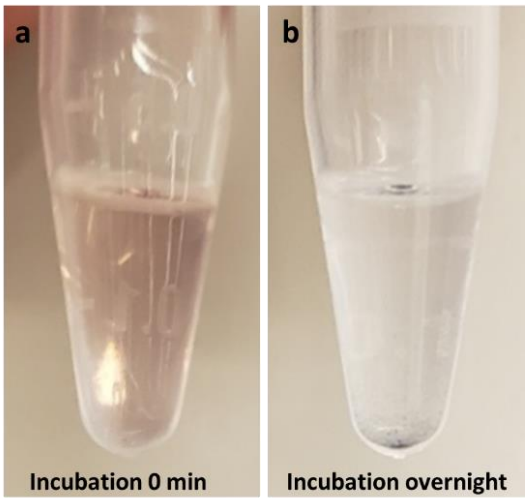

Figure 2.15. Photo of PEG@AuNR solution incubated with 1.1 mg $HgCl_2$ in 600 µL of dimethyl sulfoxide (DMSO) for (a) 0 min, and for (b) overnight.

To understand the interaction of PEG@AuNR with $HgCl_2$, the supernatant of $HgCl_2$-PEG*was analysed with ^1H NMR. Figure 9c shows the disappearance of proton resonance at 2.38, 2.64, 3.42, and 3.58 ppm In the expanded Figure 2.16, the -SH thiol proton shifted slightly downfield with a doublet (Figure 2.16C) instead of triplet (as seen in in Figures 2.14a and 2.13b at 2.26 ppm), and methyl proton at 3.24 ppm showed reduced intensities while CH_2 quartet at 3.21 ppm collapsed to a singlet at 3.17 ppm (Figure 2.16B-C). Note that signals at 3.37, and 3.43 ppm are buried under residual HDO. These results indicate that there are no free PEG-thiol ligands in the $HgCl_2$-PEG* solution, and the changes in proton resonances are characteristics of ligands bound to metal or nanoparticles.[99] It is noteworthy that CH_2 proton at position ‘e’ of PEG-thiol long chain, shifted downfield, 4.04 ppm, with ABq spin system. It is possible that metal core, Hg^{2+}, can induced diasterotopicity in methylene proton. This phenomenon has been reported in several articles.[100–102]

To further demonstrate the complexation of PEG thiol and Hg^{2+}, we explored the interaction between free PEG thiols with native $HgCl_2$ (shown in Figure 2.14d). The NMR was made from mixing 2.0 mg of HgCl2 and free PEG (43.15 mg). The ^{1}H NMR spectrum and chemical shift assignments of free PEG-thiol ligands are shown in Figure 2.14a and the first column of Table 2.4. The 1H NMR spectrum of PEG@AuNR in Figure 2.14b and expanded in Figure 2.16a-b,

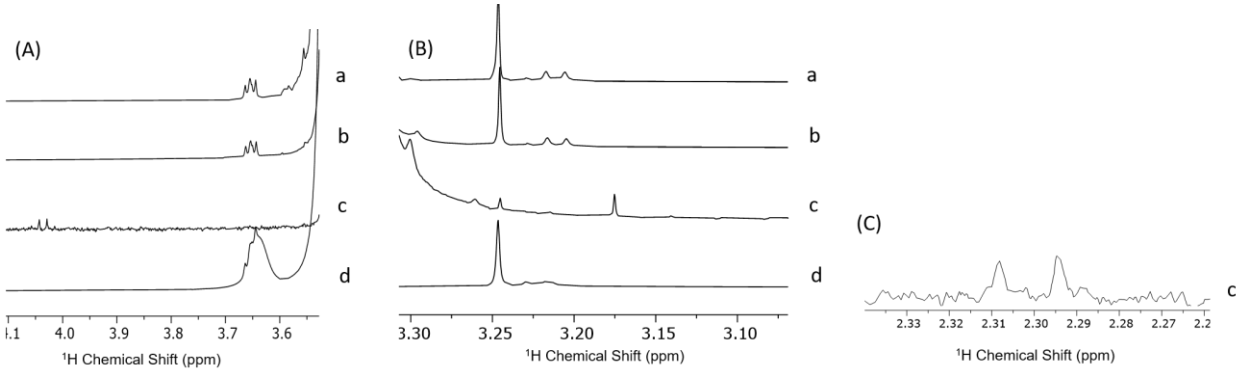

Figure 2.16. Expanded image of ^{1}H NMR spectra from Figure 9 to illustration the line broadening and disappearance of proton resonances upon binding with mercury 1H NMR of $HgCl_2$-PEG* complex show a) deshielded CH2 proton resonance at 4.04 ppm (quartet) b) Thiol proton resonance also shifted slightly downfield at 2.3 ppm (doublet) and c) Methyl proton signal at 3.24 ppm is significantly reduced and CH_2 proton at 3.17 ppm collapsed from quartet to singlet demonstrated that PEG is complexed with mercury.

shows the disappearance of methylene proton at 3.58 ppm and a slight line-broadening of α-CH2 proton adjacent to thiol (Table 2.4). This result indicates that PEG-thiol chains are stabilized on the surface of the AuNRs.[103–105]

2.4 CONCLUSIONS

Preparation of PEG@AuNRs from CTAB@AuNRs was performed through the well-known thiol-gold chemistry approach. Due to the coating of PEG-thiol ligands, the PEG@AuNRs show superior performance compared to CTAB@AuNRs in a number of ways, including sensitivity, stability and specificity. In addition, the total number of PEG-thiol ligands on the surface of the AuNRs in the sensing system can be controlled by adjusting either the concentration of AuNRs or the incubation time of PEG@AuNRs with Hg^{2+}, which detaches certain amounts of PEG-thiol from the AuNRs via Hg^{2+}-S complexation. Adjusting these inputs impacts the plasmonic responses of the system to the same concentration of mercury. The characterization of AuNR morphologies shows the differences of each sensing system. According to spectral data and AuNR shape changes, obtained under various incubation times, the proposed mechanism for the adjustable sensing system includes two processes: the Hg^{2+}-S complexation and amalgam formation. Evidence for this mechanism obtained from HRTEM, ^{1}H NMR and other observations were provided. This present work enables the development of a mercury plasmonic based sensing system with adjustable peak plasmonic response.

2.5 Notes on the Chapter

In any experiment there are many unanswered questions, and this is no exception. It has been asked if reduction of the Hg^{2+} ion during incubation might be responsible for the observed effect. However, this seems unlikely given the lower activity of $Au^{(0)}$, which would suggest the reverse reaction, where gold ion oxidizes $Hg^{(0)}$ would dominate. It is still possible that a reaction occurs between Hg^{2+} and the sulfhydryl group of the ligand, however, UV and EDS examination of samples after prolonged incubation gave no evidence of $Hg^{(0)}$ without reduction with $NaBH_4$.

There are also several areas ready for further exploration using the technique discussed in this paper. First, there is the obvious exploration of other anisotropic gold nanoparticles with other geometry. Gold bipyramids would be a particularly interesting shape to explore given their high sensitivity to shape change, relative mono-dispersity, and poor morphological stability. Also, the use of "mini-rods" a relatively new material the smaller size of which might enhance the relative sensitivity of the AuNRs to an analyte. Second, it could be very informative to observe the relative adsorptive strengths, against Hg^{2+} of varied sulfur end-capped materials on gold nanoparticles with different dominant lattice planes. Such an investigation could provide valuable information, not only about the nature of the gold-sulfur bond, which is still not fully understood, but also about how different attachments effect the orbital structure of sulfur atoms.

Finally, in a collaborative work there is always a question of disambiguating individual contributions, as such it is necessary to point out the specific work of a few people. HR-TEM imaging was done by Dr. Ellen Lavoie in the Molecular Analysis Facility at the University of Washington. ^{1}H NMR studies were performed by Dr. Hla Win-Piazza and her help with data analysis was invaluable in helping me understand a world of data with which I have little experience. J.E. Doebler was helpful in the production of AuNRs, and T. Luan was responsible for some of the preliminary work testing AuNR for mercury sensing. All data presented in the paper was collect by this author unless otherwise specified. As for writing, this author produced a first and second draft of the paper the organizational structure and underlying ideas of which served as the basis for the final work along with much input, editing, and collaboration with Dr. Ying Bao.

Chapter 3

Site-specific Macromolecular Imprinted Anisotropic Plasmonic Sensor

3.1 Introduction

The ability to cheaply and rapidly detect biological materials is of extreme importance for the early discovery and treatment of disease, from micro scale viral pathogens and cancer cells to nanoscale proteins associated with neurodegenerative ailments such as Alzheimer's disease.[8,106] The traditional methods for such detection using antibody-antigen coupling requires expensive and time-consuming production of natural anti-bodies. Polymer imprinting, a technique which has long been used with small molecules,[107] or ions[108] for separation and catalysis has also been recently explored for imprinting using macromolecular materials such as proteins[109] and viruses.[110] Polymer imprinting is a process where a material of interest, anything from ions to cells, is placed in a monomer solution. The monomer is polymerized around the material, which will then be removed hence creating a surface that is highly attractive to the material of interest. The incorporations of such polymer imprinting for sensing has been primarily utilized on metal surfaces,[111,112] or using single-dimensional materials such as spheres in order to take advantage of their optical properties.[107]

Metal nanoparticles have become ubiquitous in their use as sensors due to their interesting plasmonic properties. Electrons trapped on the surface of metal nanoparticles interact with the electromagnetic field from visible and NIR-light causing them to oscillate coherently, a property called surface plasmon resonance (SPR). Anisotropic nanoparticles, such as gold nanorods (AuNRs) , have nano-dimensionality in two directions and exhibit SPR for each dimensionality. The SPR associated with the longitudinal dimension of such particles, called longitudinal surface plasmon resonance (LSPR), is especially useful for sensing because of its

extreme sensitivity to changes in refractive-index in proximity to the surface of the nanoparticle.[113] This highly sensitive area on the tips of AuNRs has spurred significant research for the detection of many materials both inorganic, such as ions,[42,82,85,114] and organic materials, including proteins,[18] bacteria,[14] and even whole cells.[115] Abbas et.al have demonstrated detection of proteins using AuNRs deposited on a silica surface, where tip-selectivity was induced through the expected preferential replacement of cetyltrimethylammonium bromide (CTAB) with 4-aminothiophenol (4-ATP) on the tips of the gold nanorods. These were demonstrated to have good selectivity for the imprinted protein but also had significantly weaker LSPR response then desired and the deposition on a silica surface also mandated a long incubation time to allow for surface equilibration of the protein.

In this work we have investigated combining the sensitive plasmonic properties of gold nanoparticles with the high degree of selectivity and durability of silica-based polymer imprinting. This work is distinguished from others by: 1) the use of anisotropic materials (AUNRs and AuNBP), with highly sensitive locations, as well as, the direction of proteins to these locations and 2) the ability to imprint the selective surface onto these materials in solution rather than after deposition onto a surface to produce protein imprinted gold nanorods with a side-silica coating (Imp@SCAuNR). First side-silica coated AuNR's (SCAuNR's) were produced and characterized for their AuNR tip-exposure and relative quantity. Hemoglobin (Hb) was then attached to the SCAuNRs using a linker system with (3-aminopropyl)trimethoxysilane (APTMS) and glutaraldehyde (Glut). An imprint of the Hb was then formed We believe that this new strategy could lead to a simple and cheap method for the rapid production of sensitive and selective detectors for proteins and other macroscale biological materials.

3.2. Experimental Section

3.2.1 Materials

Hexadecyltrimethylammonium bromide (CTAB), gold (III) chloride trihydrate ($HAuCl_4 \cdot 3H_2O$), L-ascorbic acid (L-AA), hydrochloric acid (HCl), ammonium hydroxide (NH_4OH), tetraethylorthosilicate (TEOS), Oxalic Acid (OxA), (3-aminopropyl)trimethoxysilane (APTMS), thiolate polyethylene glycol (PEG-SH) (MW 5,000), and glutaraldehyde were purchased from Sigma-Aldrich (USA). N-propyltrimethoxysilane (n-PTMS) was procured from Gelest Inc. Ethanol (C_2H_5OH), silver nitrate ($AgNO_3$), phosphate buffer solution (PBS), and sodium citrate dihydrate ($C_6H_9Na_3O_9 \cdot 2H_2O$) were purchased from Fisher Scientific (USA); sodium borohydride ($NaBH_4$) from Merck. Hemoglobin bovine erythrocytes (Hb) were purchased from Worthington Biochemical Company and Fluoroscein(6) bovine serum albumin (F-BSA) was obtained from Biosearch Technologies. All chemicals were used as received unless otherwise specified.

3.2.2 Synthesis of Gold Nanorods.

Gold nanorods were synthesized using an expansion of the seed-mediated method described by El-Sayed.[28] To produce gold seed, 250 µL of $HAuCl_4$ (10 mM) was first added to 10 mL of 100 mM CTAB in a scintillation vial, and the solution was reduced with 600 µL of ice-cold $NaBH_4$ (10 mM). The solution was immediately shaken vigorously while removing the cap several times to facilitate the removal of hydrogen. The seed was kept at 40 °C in a water bath for 2 h.

The growth solution for the gold nanorods was produced by dissolving 400 mL of 100 mM CTAB, with heat and sonication, in a 1 L round glass media bottle. To this solution 20 mL of $HAuCl_4$ (10 mM) was added and then inverted, followed by 3.5 mL of HCl (1M) and then shaking to mix thoroughly. 4 mL of $AgNO_3$ (10 mM) and 3.2 mL of L-AA (100 mM) were

added, to the solution, and mixed by inversion. Finally, 960 µL of the prepared seed were, added to the growth solution, mixed well, and allowed to sit overnight in a water bath at 30°C. The prepared gold nanorods were stored under refrigeration until needed.

3.2.3 Synthesis of Silica Side-Coated Gold Nanorods.

To begin 20 mg of PEG-thiol (5000 MW) was dissolved in 10 mL of nanopure water to make a 2 mg/mL PEG-thiol solution. PEG solution, 750 µL, was diluted to 10 mL producing a 0.15 mg/mL PEG-thiol solution which was then stored overnight in a dark place. The 0.15 mg/mL PEG-thiol solution was heated with stirring in an 80 °C water bath for 3 h, uncapped. The solution volume reduced by 5-6 mL. The solution was capped and allowed to cool to room temperature.

Gold nanorods (12 mL) were purified twice by centrifugation for 8 min at 10000 rpm, first exchanging into nanopure water and then into 2 mL of CTAB (100 mM) to concentrate them. The concentrated gold nanorods were then added to the previously heated PEG-thiol solution which was diluted to 10 mL and allowed to sit overnight. The solution was then purified once by centrifugation for 15 min at 4000 rpm, exchanged into 10 mL of CTAB (2mM) and allowed to rest for 5 h.

The solution was then stirred at 600 rpm and the pH was adjusted to 10 with the addition of approx. 100 µL of NH_4OH (133mM in ethanol), followed by 19.5 µL of TEOS (20 %v/v in ethanol), which was added in three additions of 6.5 µL each with 30 minutes between. The solution was allowed to stir for at least 18 hours and then purified twice by centrifugation for 8 minutes at 10000 rpm into ethanol.

3.2.4 In-solution Protein Imprinting

2 mL of silica side-coated gold nanorods (SC@AuNRs) were purified one time by centrifugation and exchanged into nanopure water and then combined in a 5 mL centrifuge tube with a stir bar. 4 µL of APTMS was added to the SC@AuNR solution under stirring and allowed to react for 6 minutes then purified two times by centrifugation for 8 minutes at 10000 rpm and redispersed into 2mL nanopure water and combined in a 5 mL centrifuge tube with a stir bar. 20 µL of glutaraldehyde (25 %w/v in water) was added to the SC@AuNR solution under stirring and allowed to react for 30 minutes then purified two times by centrifugation for 8 minutes at 10000 rpm and redispersed into 2mL 25 µg/mL Hb in PBS (20mM) and combined in a 5 mL centrifuge tube and shaken for 2.5 hours at room temperature. The Hb solution was then centrifuged at 3000 rpm for 12 min and redispersed into 20 mM PBS and combined in a 5 mL centrifuge tube with a stir bar. 4 uL each of APTMS and n-PTMS were then added under stirring and allowed to react for various times before being centrifuged once for 8 minutes at 10000 rpm and redispersed into a solution of 0.5 M HCl and 0.02M CTAB and sonicated for 5 minutes at 45°C. The Hb imprinted SC@AuNRs (ImpSC@AuNR) were then purified two times by centrifugation for 8 minutes at 10000 rpm and redispersed into ethanol for storage.

3.2.5 Hemoglobin Sensitivity

For each concentration of Hb, 100 µL of prepared ImpSC@AuNR were centrifuged for 8 min at 10000 rpm and redispersed into Hb (0.2 ug/mL, 0.3 ug/mL, 0.4 ug/mL, 0.5 ug/mL, 1 mg/mL, 2.5 mg/mL, and 5 mg/mL) in 20 mM PBS and allowed to incubate at room temperature while shaking for 1 hour. The samples were then centrifuged at 3000 rpm for 12 min and redispersed into 20 mM PBS and characterized using UV-Vis spectroscopy.

3.2.6 Hemoglobin Removal

ImpSC@AuNR with attached Hb are centrifuged and redispersed in a solution of oxalic acid (2 mg/mL) and CTAB (0.02M CTAB) and shaken at moderate speed for 30 min. The solution was then centrifuged two times for 8 min at 10000 rpm and redispersed into nanopure water.

3.2.7 Hemoglobin Selectivity

100 µL of prepared ImpSC@AuNR were centrifuged for 8 min at 10000 rpm and redispersed into BSA (1 mg/mL) in 20 mM PBS and allowed to incubate at room temperature while shaking for 1 h. The samples were then centrifuged at 3000 rpm for 12 min and redispersed into 20 mM PBS and characterized using UV-Vis spectroscopy. The samples were then redispersed into Hb (38 µg/mL) in 20 mM PBS and allowed to incubate at room temperature while shaking for 1 h. The samples were then centrifuged at 3000 rpm for 12 min and redispersed into 20 mM PBS and characterized using UV-Vis spectroscopy.

3.3 Results and Discussions

Side-coated gold nanorods were produced by growing silica on the sides of gold nanorods after partial replacement of CTAB with PEG-disulfide. Silica was selected for this process due to its high durability in biological environments and excellent stabilizing ability in solutions with varied electrostatic properties. It has been well documented that when AuNRs are stabilized in excess concentration of CTAB silica coating will begin at the tips of the AuNRs. This is a result of the easier penetration of silica monomer, TEOS, at the tips of the AuNR's where curvature will cause lower density of the CTAB bilayer. To force nucleation of silica on the sides of gold nanorods CTAB is replaced on the tips of the rods with a material that will maintain stability but reduce the nucleation of silica. The same low density of CTAB at the tips of the gold nanorods, mentioned above, can also be used to promote selective replacement of CTAB on AuNR tips with PEG-thiol or PEG-disulfide. As can be seen in Figure 3.1 PEG-Thiol is heated at 80 °C in air to oxidize PEG-Thiol producing PEG-Disulfide. The CTAB

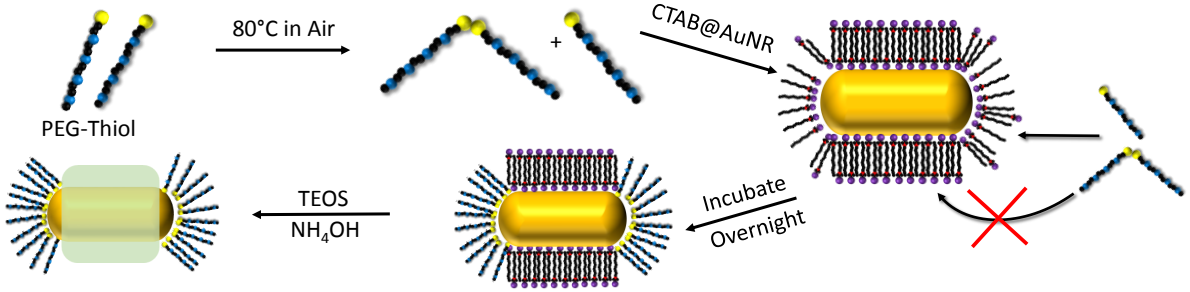

Figure 3.1 A schematic for the synthesis of side coated gold nanorods using PEG-Disulfide and PEG-Thiol.

concentration is lowered to further increase the difference in density between the sides and tips of the AuNRs. The higher CTAB side density causes the PEG-Disulfide molecules to be excluded from the sides of the rods and only adsorbed on the tips of the AuNRs. By further reducing CTAB concentration it is expected that the remaining CTAB bilayers at the center of the gold nanorods will be driven to enhance TEOS nucleation because of their hydrophobic

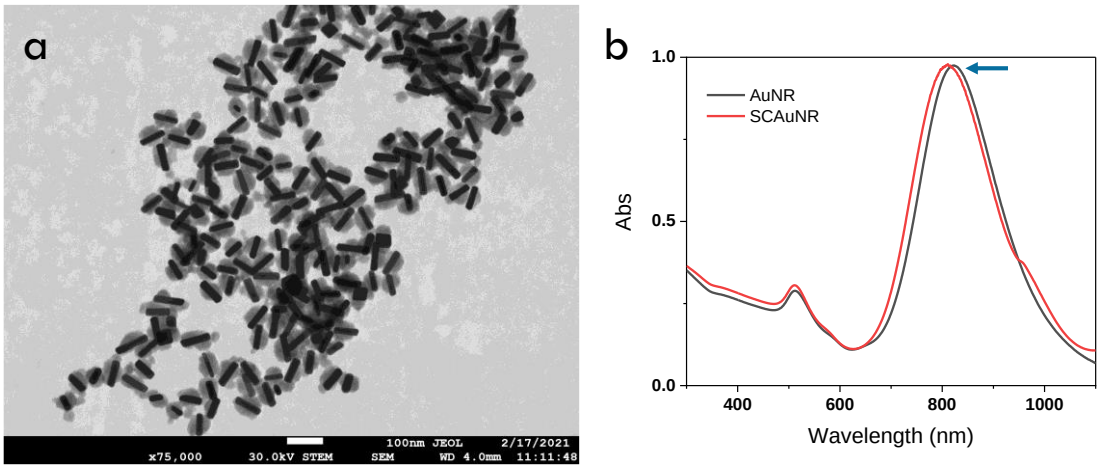

Figure 3.2 a) An SEM image of side silica coated gold nanorods. b) UV-Vis spectra of gold nanorods (black) and side-coated gold nanorods (red).

interior. This process combined with careful control of TEOS concentration, can, be used to

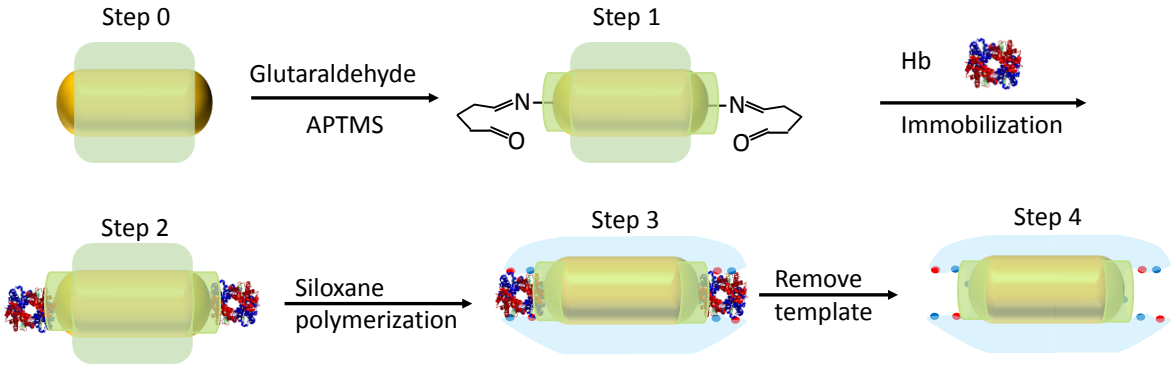

Figure 3.3 A mechanism for the imprinting of SC@AuNRs with a surface selective for the hemoglobin protein with process steps as indicated.

create large quantities of side-coated gold nanorods (SC@AuNRs), as shown in the STEM images, Figure 3.2a. By comparing the optical spectra of the AuNRs and SC@AuNRs in Figure 3.2b, it can be seen that the side-coating of these gold nanorods produced a significant blue-shift of the longitudinal resonance shift. This shift may be attributed to the difference in dielectric constant between the CTAB and PEG material as well as the increased scattering of the silica coating. This blue-shift showed good correspondence to the level in which the side-coating exposed the tips of the AuNRs. Larger shift corresponding well to greater AuNR exposure and

small to no-shift relating well to exposed ends with fully covered sides. These SC@AuNRs were then imprinted in-solution for the detection of Hb protein. Imprinting involved several steps which are illustrated in Figure 3.3. The step labeled 1 is the decoration of the SCAuNRs with a linker to attract the hemoglobin protein to the surface, this linker is composed of APTMS and glutaraldehyde. The APTMS produces a layer of low-density silica on the rod surface containing numerous exposed amino head groups, and these amino head groups will react with glutaraldehyde (Glut) forming polymer chains with end groups that can react with amino groups on the protein surface and holds them in place during polymer imprinting. The formation of an APTMS-Glut linker can is confirmed by a slight red-shift of the LSPR, seen as step 1 in figure 3.4b. The SCAuNRs are then incubated in Hb producing a strong red-shift in the LSPR as can

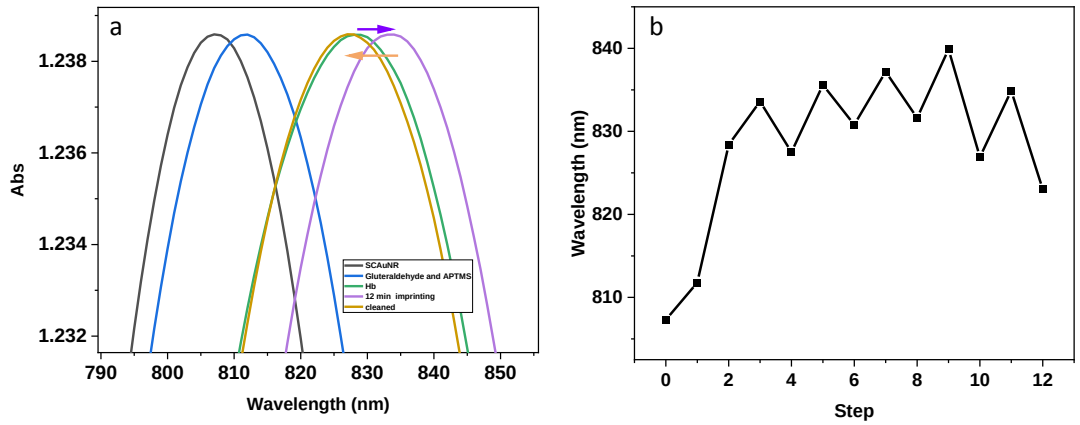

Figure 3.4 a) UV-Vis spectra of the LSPR during the imprinting process. **b)** Summary of the LSPR shift for the imprinting process and four subsequent cycles of hemoglobin attachment and removal. (All cycles with 25 µg/mL Hb.)

be seen in step 2 of Figure 3.4b. The Hb@SCAuNRs were then reacted with a mixed siloxane solution composed of n-PTMS and APTMS which arrange themselves in a low energy configuration surrounding the Hb protein before condensing to form a network polymer and further shifting the LSPR to higher wavelength as shown in step 4 of figure 3.4. This new low

energy surface on the AuNRs acts to enhance the strength of adsorption for hemoglobin protein on the Imp@SCAuNRs while diminishing the adsorption of other material. In figure 3.3 steps 3 and 4 selective surfaces, indicated as red (electrostatic) and blue (hydrophobic) are molded on the Hb protein. The template Hb is then removed along with excess siloxane using an acid cleaning and causing a blue-shift to the LSPR as indicated in Figure 3.4a. The resulting Imp@SCAuNR could be run through three cycles of Hb detection and cleaning before showing significant change to the shift, which is most likely, due to damage on the imprinted template.

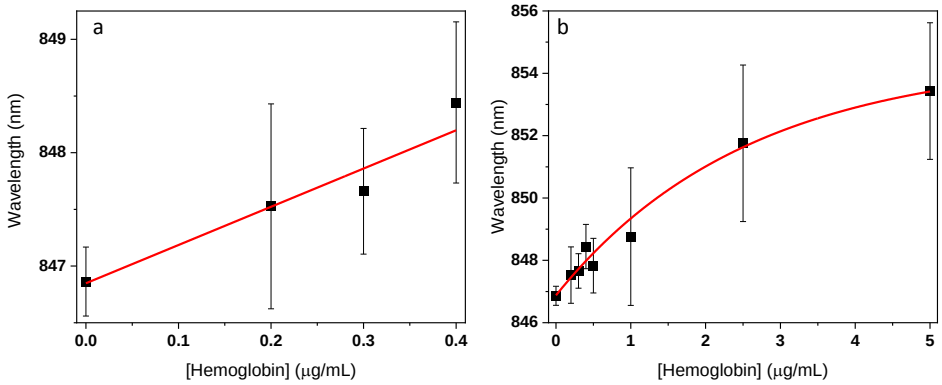

Figure 3.5 a) A plot of the change in wavelength vs concentration of hemoglobin for ImpSC@AuNRs from 0 to 0.4 µg/ mL with linear fit. ($m = 3.5 \pm 0.5$ µg · nm /mL $R^2 = 0.925$) **b)** A plot of the change in wavelength vs concentration of hemoglobin for ImpSC@AuNRs to hemoglobin from 0 to 5 µg/ mL with exponential fit. ($R^2 = 0.939$)

The ImpSC@AuNRs were further used to determine their sensitivity and selectivity. Figure 3.5 shows the sensitivity of the LSPR wavelength for ImpSc@AuNR when exposed to varied amounts of Hb. The sensitivity of the ImpSC@AuNR demonstrate good linearity at low concentrations (Figure 3.5a) with a limit of detection of 260 ng/mL Hb. As the concentration increases the sensitivity plateaus sharply following a model that closely matches a Langmuir

isotherm[116] indicating saturation of the available site on the Imp@SCAuNR. The selectivity was examined by comparing the LSPR shift of the Imp@SCAuNRs for Hb after incubation with bovine serum albumin (BSA) a common protein often found in similar concentrations throughout the body and also containing many sulfur surface groups making it particularly attractive to gold, and as such a strong competitor for bonding to uncoated surface on AuNRs. In Figure 3.6 the selectivity results are compared for Imp@SCAuNRs imprinted with siloxanes for 6 and 12 min. and incubated with BSA at 25 times the concentration of Hb. It can be observed that for samples imprinted for 6 min there is greater total shift (>20 nm) than for specimen imprinted for 12 min (~ 17 nm) the greater total shift for Hb would suggest that the shorter imprinting is superior. However, examining the ratio of the LSPR shift for Hb against the LSPR shift for BSA it is observed that the 12 min. imprinting results in 4.1 times the LSPR shift for Hb than for BSA, whereas the 6 min imprinting resulted in only 3.7 time the LSPR shift of Hb for BSA. Which

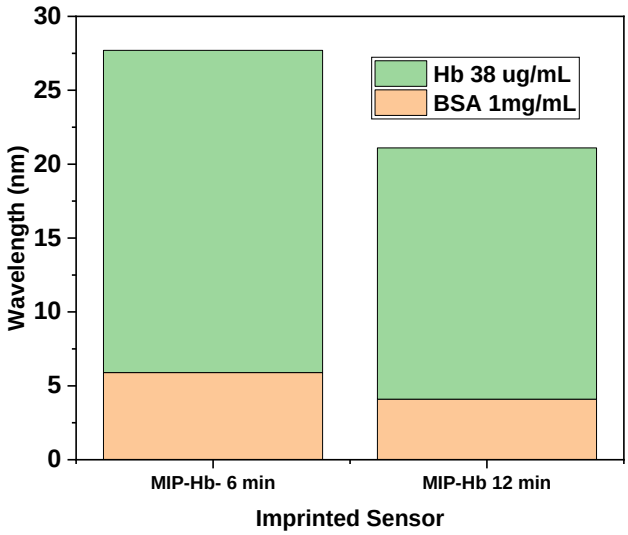

Figure 3.6 A plot comparing the selectivity ImpSC@AuNRs for Hb versus BSA.

suggests that increasing imprinting time lowers total sensitivity but may enhance sensitivity for Hb over BSA, thus enhancing selectivity.

3.4 Conclusions

In this work we have presented a method for imprinting for side-coated gold nanorods with a selective surface for the qualitative detection of proteins. Based on the obtained preliminary results it was shown that the LSPR of these Imp@SCAuNRs was significantly sensitive to the protein and that this sensitivity as well as the selectivity for proteins could be tuned by controlling the reaction time. The imprinted surfaces were also shown to have good durability retaining similar sensitivity through sensing cycles. In addition, the ability to imprint plasmonic materials in solution offers several advantages over deposition methods: 1) the sensitivity of the Imp@SCAuNRs is superior, both in terms of total LSPR shift and lessened incubation time, 2) the materials can be imprinted in bulk for later use as desired, and 3) the ability to imprint materials with different plasmonic characteristics separately, which could allow for the construction of multiplexed sensors capable of detecting several materials simultaneously.

3.5 Notes on the Chapter

It cannot be over stressed that the data presented in this chapter is preliminary. The methodology presented for producing SC@AuNRs has yet to be fully characterized. In particular the production of pure PEG-disulfide has not yet been confirmed although NMR has shown a change to the structure of the PEG thiol reagent. It is also true that this is only one of several possible methodologies which can be utilized in side-silica coating of AuNRs several of which show success using only PEG-thiol. This further leads to the question of whether some amount of PEG-thiol may be essential to preserve the stability of the SC@AuNRs during the molecular

imprinting process. To answer this question, it is necessary to confirm the purity of the PEG-disulfide produced with our method or to compare imprinting using SC@AuNR fabricated with a known source of pure PEG-disulfide.

There are many other areas that it is necessary to explore both regarding the construction of Imp@SCAuNRs and the characterization of their function. First, it is necessary to more rigorously examine the synthetic methodology of the Imp@SCAuNRs towards increasing reproducibility. The imprinting step is problematic in that the reaction is self-propagating and only stopped by removal of AuNRs from the solution making reproducibility highly time dependent. We would also like to employ methodologies, such as, Raman spectroscopy to further confirm the attachment of the protein to the rods, as well as, techniques from biochemistry such as a western blot to verify uptake of protein from the solution. It is also true that although the sensitivity for Hb has been focused to the LSPR of the AuNRs the imprinting process is not restrictive to imprinting Hb on the tips. It is probable that much of the surface of the Imp@SCAuNRs is imprinted for Hb, which ultimately reduces the limit of detection for the sensor and it is thus essential that we further explore methodologies to direct proteins only to the tips of the rods in order to maximize detection. Finally, it is also desirable to explore incorporating other linking method into the imprinted surface which might enhance selectivity for the desired protein, possibly through known affinity such as pseudo or true antigen-antibody binding or the incorporation of metal ions to make use of coordination chemistry which can not only add specificity for elements on a protein surface but can even repel competitive biological materials.

Furthermore, although testing for sensitivity certainly demonstrates a response to Hb the

concentrations of AuNRs was relatively uncontrolled between experiments. As this ratio would have a strong effect on the strength of LSPR shift it is absolutely essential to normalize such a concentration before a true assessment of the abilities of Imp@SCAuNRs can be ascertained.

Chapter 4

Morphology Control of SERS-active 2D Gold Nanosnowflakes

Reproduced with permission from Cohen-Pope, S.; Crockett, J.R.; Wang, M.; Flynn, K.; Hoff, A.; Bao, Y. Morphology control of SERS-active 2D gold nanosnowflakes. *J. Mater. Chem. C* **2020**.

4.1 Introduction

Synthetic control over the morphology of gold nanomaterials has attracted extensive interest in the past decades since the size/shape of these nanomaterials can greatly influence their optical, electronic and chemical properties.[117,118] These properties determine the usefulness of nanomaterials in a wide range of applications from catalysis[119], bio-sensing[120], optics[121], solar cells[120], bioimaging[122], and surface-enhanced Raman spectroscopy (SERS)[123]. A variety of shapes can be produced including spheres, cubes, rods, plates, etc., which allows for the selection of desired properties for specific applications.[124–126] Among this plethora of shapes, 2D branched nanostructures (e.g. dendritic, snowflake, flower-like) have obtained particular attention in SERS and catalysis. Such dendritic nanostructures have large specific surface area and high density of steps and corners which are essential features for high performance in SERS and catalysis.[44,127–129]

Until now, most reported 2D Au branched nanostructures were fabricated at interfaces, such as air/water, liquid/liquid and solid/liquid interfaces.[44,130–133] Compared to other nanostructures, 2D branched nanostructures have a different synthetic challenge, which is to confine the branching in plane while minimizing the growth in the perpendicular direction.[133] The studies that have managed to synthesize such nanostructures[132,134,135] have utilized methods such as electrochemical deposition[130] and galvanic reaction[135,136]. These have been demonstrated to directly fabricate branched nanomaterials on substrates, however, those methods have minimal control on the location and the quantity of gold ions being reduced. Control of these parameters is essential for influencing the nucleation and growth kinetics of the nanocrystals and subsequently impacting the final morphology. On the other hand, several groups have put efforts into preparing 2D Au dendrite nanostructures with the assistance of structure-directed surfactants or additives and have demonstrated better control of the morphology of 2D Au dendrite nanomaterials.[136,137] For example, Wang and coworkers fabricated 2D snowflake-like highly branched Au nanostructures with the aid of the cationic gemini surfactant, hexamethylene-1,6-bis(dodecyl dimethylammonium bromide) ($C_{12}C_6C_{12}Br_2$). In their work, $C_{12}C_6C_{12}Br_2$ acts as capping agent which selectively adsorbs onto the (111) plane to drive the generation of the 2D morphology. Additionally, the surfactant also plays a role in mediating the growth kinetics through the quaternary ammonium cations of $C_{12}C_6C_{12}Br_2$ binding with both Au(III) and Au(I) through strong electrostatic interactions. This leads to a decrease in the reduction potential of the gold ions and a decrease in the diffusion rate, thus resulting in an improvement in control of the shape of Au 2D branched nanostructures.[137] Unfortunately, even if the shape is well controlled, the resulting nanostructures display a broad distribution in size and product due to the lack of control over nuclei formation.

Seed mediated growth is widely used to control the morphology of branches for Au nanostructures by altering the ratio of gold seeds and chemicals in colloidal growth solution.[138] The seeds in the growth solution can act as nucleation centers, favoring exterior gold atoms to be immobilized on the surface which slows the formation of new nucleation centers. In addition, by altering the ratio of seeds and additive chemicals in the growth solution, it is possible to control the diffusion kinetics of metal ions and thus the reactivity of the gold ions. For example, Li and coworker altered the ratio of the gold seed and the additive hydroquinone, allowing for a wide range of tunability in the diameters and morphologies of urchin-like Au particles.[139] Although such an approach is commonly used in colloidal solution synthesis, there is no report on using such a method to fabricate 2D dendrites with controlled density and morphology.

In this work, we developed a simple and rapid synthetic method for 2D gold snowflake nanomaterials (Au NSFs) based on seed mediated growth. The morphology and size of the 2D Au branched structurers can be finely tuned by altering the synthesis conditions. Gold nanoparticle seeds were pre-embedded on the substrate, then a reduction mixture of sodium citrate and hydroquinone, which acts as reducing agents and capping ligands, were used to form the Au NSF. The Au^{3+} is reduced to Au^{1+} by citrate, while Au^{1+} is further reduced to Au^{0} by hydroquinone. The impact of seed concentration and growth solution pH were explored in detail, and a mechanism of formation is proposed to explain the experimental data on both morphology formation and evolution. Finally, we investigated and compared the optical properties and SERS activities among the various morphologies of Au NSFs substrates.

4.2 Experimental section

Tetrachloroauric acid trihydrate ($HAuCl_4 \cdot 3H_2O$, ≥99.9%), hydroquinone (≥99%), sodium hydroxide (NaOH, 30% wt.), hydrogen peroxide (H_2O_2, 30% wt.), crystal violet (CV), cellulose acetate (CA, MW ≈ 30,000) and poly(sodium 4-styrenesulfonate) (PSS, MW ≈ 70,000) were purchased from Sigma-Aldrich. Hydrochloric acid (HCl, concentrated) was purchased from Macron. Ethanol (95%) was purchased from Pharmco-Aaper. Sodium citrate dihydrate ($C_6H_5O_7Na_3 \cdot 2H_2O$, ≥99%) and Sulfuric acid (H_2SO_4, concentrated) were purchased from Fischer. Poly(diallyldimethylammonium chloride) (PDADMAC, MW ≈ 240,000) was purchased from Polysciences. Nanopure water with a resistivity of 18 MΩ cm was used in all experiments.

4.2.1 Preparation of Seed Solution.

Negatively charged citrate-coated gold nanoparticles (Au NPs, 13 nm in diameter) were prepared according to the well-known citrate reduction method as described in the literature.[140] Typically, HAuCl4 (75 μL, 0.1 M) was added to nanopure water (30 mL) and brought to a boil on a stir plate. Then, sodium citrate (900 μL, 1% wt.) was added to the solution and left to boil for 40 min. A few minutes after the sodium citrate was added, the solution turned from clear to lavender, before finally turning a wine red. The resulting seed solution was allowed to cool to room temperature, then stored in the fridge for further use.

4.2.2 LBL thin film preparation

Silicon-wafer substrate and glass slide substrate with a typical size of 10 mm × 10 mm were cleaned in a piranha solution [3:1(v/v) H_2SO_4/H_2O_2]. *Attention: Piranha solution is extremely dangerous and should be handled very carefully.* After cleaning the substrates were rinsed with Nanopure water at least three times and then stored in Nanopure water until use. The glass slide substrates were used for the purpose on obtaining UV-Vis spectra of Au nano-

snowflakes. The multiple polymer layers were fabricated by the spin-assisted LbL method. A layer of PDADMAC was first deposited onto the substrate from a 0.1 % wt PDADMAC solution by spin coating for 30 s at 11,000 rpm. The substrate was rinsed once with Nanopure water and dried while spinning for 30 s at 11,000 rpm. In a similar manner, 0.3 % wt PSS solution was deposited. This procedure was repeated until the desired number of polymer bilayers was achieved. Two types of polymer bilayers were prepared. One has 1.5 bilayers which can express as this formula: PDADMAC/PSS/PDADMAC; the other has 12 bilayers $(PDADMAC/PSS/PDADMAC)_{18.5}$ which is for freestanding film where. After fabricating the designed polymer bilayers, 200 μL of the sodium citrate gold nanoparticle solution with certain dilution was deposited on the substrate by spinning coating for 30 s at 11,000 rpm. To obtain a freestanding film, a sacrificial cellulose acetate (CA) layer was first spun on the prepared silicon substrate before further deposition. Freestanding LbL thin films can be obtained by dissolving the sacrificial CA layer in acetone. The freestanding LbL films can be lifted from the solution using a variety of substrates, such as glass slides, silicon wafers, and copper grids for further characterization and investigation. All of the procedures were performed in a class 100 soft-wall clean room.

4.2.3 Gold Nano-snowflake growth.

For the nano-snowflake growth, $HAuCl_4$ (75 uL, 0.1 M) was added to Nanopure water (9.6 mL) in a 20 mL vial. The pH of the solution was adjusted as desired using NaOH (4 μL-30 μL, 1M) or HCl (20-480 μL, 1 M). The seeded substrate was suspended in the solution, then sodium citrate (22 μL, 1% wt.) was added, followed by hydroquinone (1 mL, 30 mM). After two min, another addition of hydroquinone (500 μL, 1 M) was added. After another two min period,

the substrate was then removed from the solution, and rinsed with nanopure water before being blown dry with nitrogen.

4.2.4 Instruments and measurement

We have utilized a variety of techniques to study the Au NSFs. UV-visible spectra of Au NSFs were obtained using a Jasco V-670 UV-Vis-NIR spectrometer. The morphology and thickness of Au NSFs and multilayer thin films were measured on a Bruker BioScope Catalyst atomic force microscope using tapping mode under ambient conditions. The scanning electron microscopy (SEM)and scanning transmission electron microscopy (STEM) images of the freestanding multilayer thin film with Au NSFs were obtained on the JEOL-7200F field emission SEM operated at 30 kV.

The crystalline formations of Au NSFs were checked using a Rigaku Miniflex 6G benchtop diffractometer. The X ray diffraction (XRD) patterns of Au NSFs on silica substrates were measured in the range of 32-90° with a step of 0.02° and a scan rate of 0.50°/min while spinning the samples at 10 rpm, employing a characteristic Cu Kα radiation having a wavelength of k = 1.540593 Å, with a 40 kV voltage and 15 mA current. The full-width at half-maximum (FWHM) from different peaks were used in Scherrer's equation to determine the average crystallite size of the nanoparticles.

Higher resolution TEM (HRTEM) images were obtained using a JEOL model 3010 instrument operated at 200 kV and a beam current of 104.1 μA. Samples for this analysis were prepared by depositing the freestanding films on copper grids and dried overnight.

Rhodamine 6G (R6G) molecule was used as a Raman reporter to evaluate the SERS efficiency of the Au NSFs. Samples were prepared by dipping in 1 mM R6G solution for several hours and then substrates and dried overnight. Single SERS measurements were carried out using a confocal Raman microscope (Renishaw InVia). The excitation wavelength was 532 nm, and the power was 200 μW. The spectrum was collected with a 50× objective and with 1 s integration time. SERS mapping results were collected with a 100× objective and with 5 s integration time.

4.3 Results and Discussion

4.3.1 Synthesis and characterization of 2D polymer-Au NSF composites

The approach to preparation of polymer-Au NSF composites starts from a piranha treated substrate as shown in Scheme 4.1. In order to fix the gold seeds onto the substrate, the substrate was modified with alternating layers of charged polyelectrolytes eventually leaving a positively charged polymer as the top exposed layer. Gold nanoparticle seeds with diameters of 15.0 ± 2.4 nm were prepared by reducing gold chloroauric acid with sodium citrate at boiling temperature and then deposited on the substrate via spin-coating.[141] The pre-placed seeds were grown into the NSF structures by immersing the substrate into the growth solution. To kinetically control the formation of Au^0 atoms and subsequent Au crystal, the weak reducing agents sodium citrate and hydroquinone are employed in the growth condition. It is worth mentioning that the whole growth process is under 2 minutes which is very rapid.

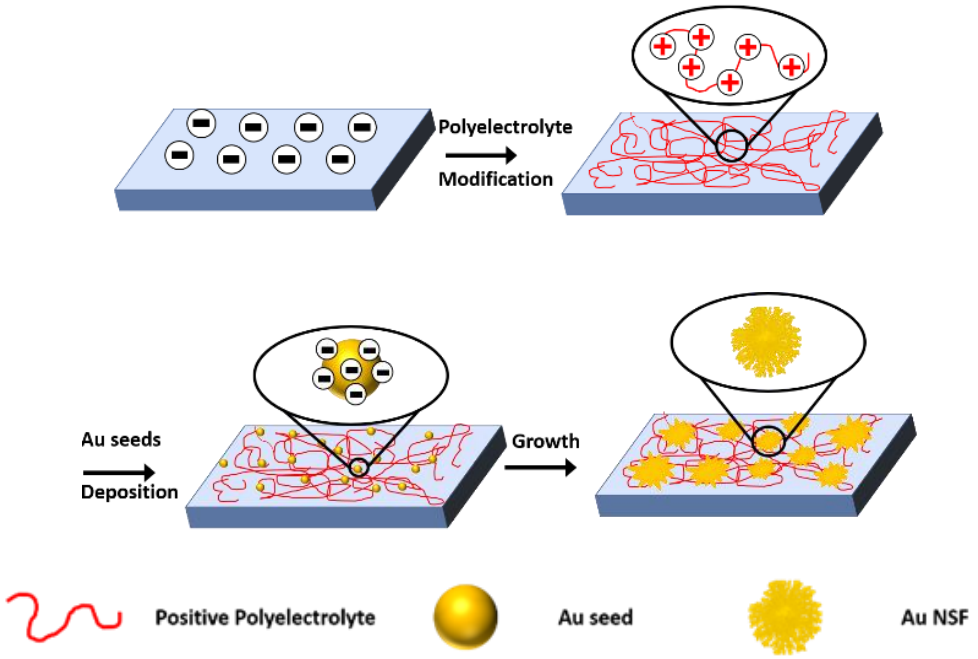

Scheme 4.1. Schematic Illustration of the polymeric- gold nano-snowflake (Au NSF) composite preparation

Figure 4.1a shows the scanning electron microscopy (SEM) image of the fabricated NSFs, revealing their morphology, structure, and size. It clearly shows that the fabricated Au NSFs

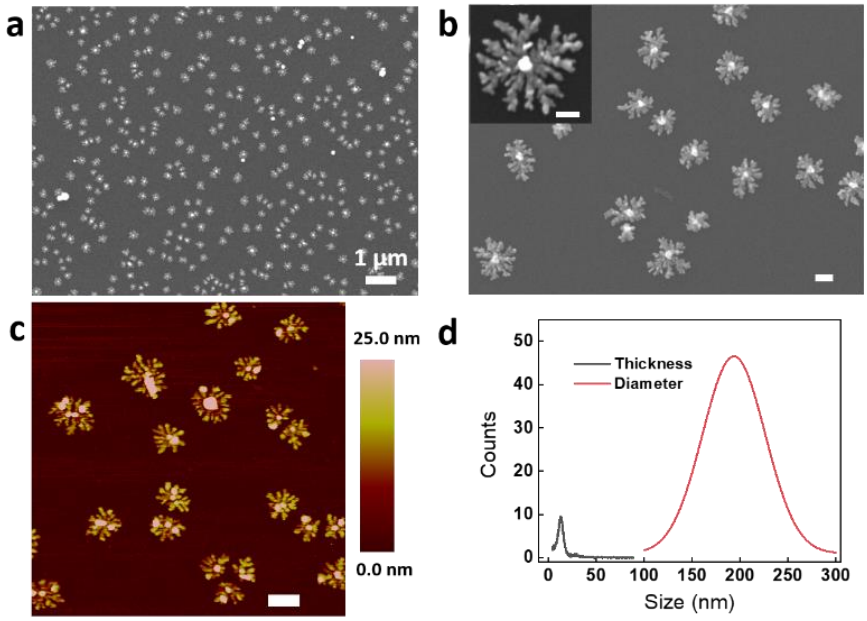

Figure 4.1. SEM images of as-prepared NSFs with (a) low magnification and (b) higher magnification (the inset in b shows the dendrite nanostructure of the individual NSF. (c) Height AFM image of the fabricated NSFs on polymer modified substrate shows the thin thickness of the NSFs. (d) Data histograms of NSFs' thickness (black line) and diameter (redline). Scale bars in b and c: 100 nm

uniformly cover the substrate without any significant aggregation. The morphology of individual Au NSFs shows the rather symmetric dendritic nanostructure with pronounced branches originating from the core and then split into larger numbers of sub-branches filling the space at the boundaries which is clearly presented in Figure 4.1b and 4.1b inset with larger magnification. Based on atomic force microscopy (AFM) measurements, the average diameter of the Au NSFs is 194.4 ± 37.6 nm and the average thickness is about 12 nm, the size and thickness histograms are shown in Figure 4.1d (red and black traces respectively). Thus, the aspect ratio of the Au NSFs is well above 20 which indicates the structure is 2D. It is worth mentioning that the average thickness of a NSF more closely represents the branch height, and in general, the core of the Au NSF is much

higher than the average thickness. One representative AFM image of an individual NSF with

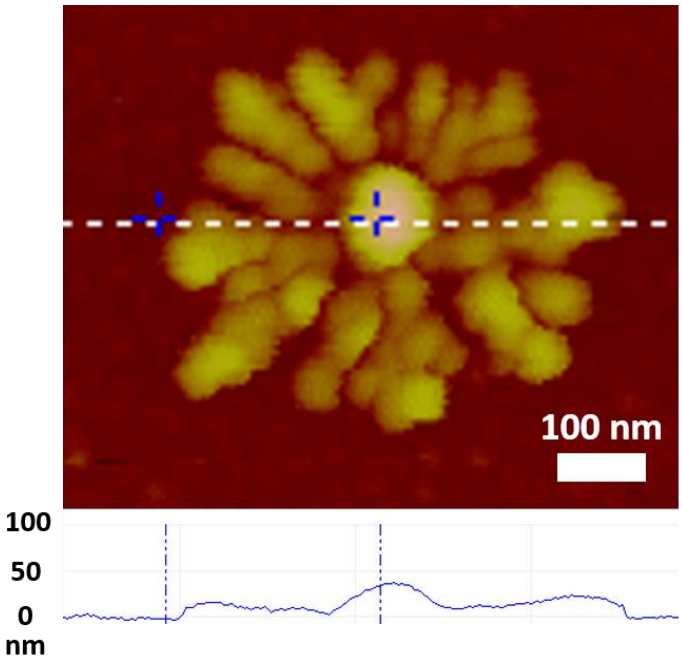

Figure 4.2. AFM image and line profile of Au NSF.

height profile is provided in Figure 4.2 showing that the core height of the NSF about 40 nm is higher than the flake. Additionally, the branches of the NSF are not completely flat and the thinnest branch is less than 10 nm.

Figure 4.3a presents an X-ray diffraction (XRD) pattern of the as-prepared NSFs on polymer modified Si substrate which reveals its crystalline information. There are clearly observed main diffraction peaks at ca. 38.2° and 44.4° assigned to the (111) and (200) lattice planes of face-centered cubic (fcc) Au crystal (JCPDS No. 4-0784). In addition, the diffraction peak at ca. 64°, assigned to the (220) lattice planes, is quite weak and cannot be well discerned. The single crystalline domain, determined by the Debye-Scherrer formula, was 16.60 nm and

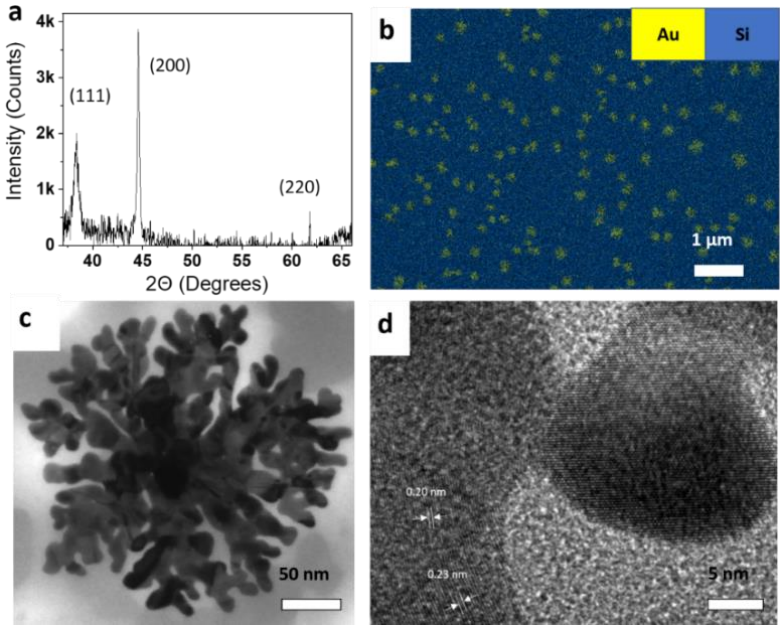

Figure 4.3. Characterizations of the as-prepared NSF on polymer modified Si wafer: XRD pattern (a), elemental mapping (b), TEM and corresponding HRTEM images (c,d). The exposed lattice fringes are (111) plane and (200) plane, corresponding to the Au lattice spacing of 0.23 nm and 0.20 nm, respectively.

40.02 nm according to the (111) and (200) crystalline planes, respectively. It is understandable that (111) gives a smaller crystalline size since the sharpness of the diffraction peaks correlates to the size of the crystallite. It is interesting to note that the intensity ratio of the (111) peak to the (200) peak, estimated by normalizing to the (111) peak, is ca. 0.5. This value is substantially smaller (specifically speaking, nearly 4 times) than is reported in the standard JCPDS file of Au, which generally is ca. 2.[142] Such an observation indicates that the as prepared Au NSFs in

Figure 4.1 are polycrystalline in nature and are predominantly enriched with (200) crystal facets. Elemental analysis was performed by energy dispersive X-ray spectroscopy (EDS) elemental mapping (Figure 4.3b) and confirms the active presence of silicon as the substrate and further confirms that NSFs are composed of elemental Au.

In order to perform high-resolution transmission electron microscopy (HRTEM) to further verify the dominate population of (200) planes in the Au NSFs, freestanding NSFs were fabricated by adding a sacrificial layer on the substrate before the polyelectrolyte modification and increasing the numbers of polyelectrolyte bilayers before seed deposition. The detailed preparation of freestanding film is stated in Experimental Section. Figure 4.4 show the Au NSFs fabricated on 18 bilayers of polymeric thin film composed by alternating deposition of PDADMAC/PSS. It can be clearly observed that the polymeric thin film, which is porous, is

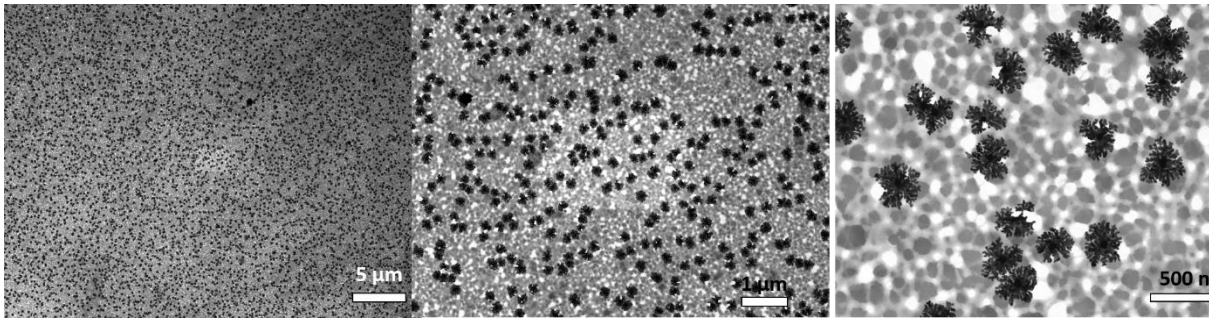

Figure 4.4. Low magnification (left), middle magnification (center) and high magnification (right) STEM images of freestanding Au NSFs decorated thin film.

uniformly decorated with a high density of Au NSFs. The porous structure of the thin film is possibly due to the low concentration of polymer that was applied in this study. The size and morphology of Au NSFs are consistent with such structures produced on polymer modified silicon wafers. The Au NSFs are composed of numerous branches and therefore form nanogaps. The corresponding HRTEM of individual Au NSF is shown in Figure 4.3c-d. The crystalline lattice fringe spacing's of 0.20 nm and 0.23 nm, assigned to (200) and (111) facets of fcc Au, can

be easily observed. This observation is in good agreement with the data obtained from XRD investigation showing that the Au NSFs is polycrystalline.

4.3.2 Mechanistic study of the Formation of Au NSFs

The formation mechanism of 2D dendritic nanostructures is always a contentious topic. It has been reported that the 2D nanostructures including nanoplates and nanodendrites can be formed under kinetically controlled conditions, where the driving force is largely through non-equilibrium processes.[143] The main criterion proposed to achieve kinetic control is that the reaction should proceed considerably slower than under normal conditions. Under such conditions, the final product can take on morphologies deviating from the thermodynamically favored equilibrium shape. Therefore, the formation of more complicated structures requires a higher driving force, i.e., a lower reaction or precursor rate. In our work, the growth of 2D Au NSFs are formed under kinetically controlled reduction by using the weak reducing agents sodium citrate and hydroquinone in the growth condition. In addition, the whole nanostructure formation process is under the guidance of "diffusion-limited aggregation" (DLA) strategy as depicted in Scheme 4.2.

The substrate initially has deposited Au NP seeds acting as a nucleus, which are the growth centers for the final products. A reduction mixture of sodium citrate and hydroquinone are used to stepwise reduce Au^{3+} to Au^{0}. Since the growth step is operated at room temperature, the reducibility of sodium citrate is weak which can only reduce Au^{3+} to Au^{1+}. When hydroquinone was added, the Au^{1+} was slowly reduced to Au^{0} which then migrated onto the substrate where aggregation with the existing Au seeds forms the primary branches. With continuous reduction of Au^{3+}, more Au^{0} is formed far from Au cores and diffusion across the

substrate to further join to the core occurs at a place with a lower energy barrier to form secondary and higher order branches. The process will last till all Au^{3+} ions are consumed. Eventually, the DLA process facilitates the assembled nanostructure as a dendrite-like fractal structure. The formed nanostructure was stabilized by the excess sodium citrate, adsorbing on the Au surface. Note that hydroquinone might also adsorb on the Au surface, in direct competition with sodium citrate. However, given that sodium citrate possesses stronger coordination with the gold surface than does hydroquinone, it acts as the primary ligand.[139,144]

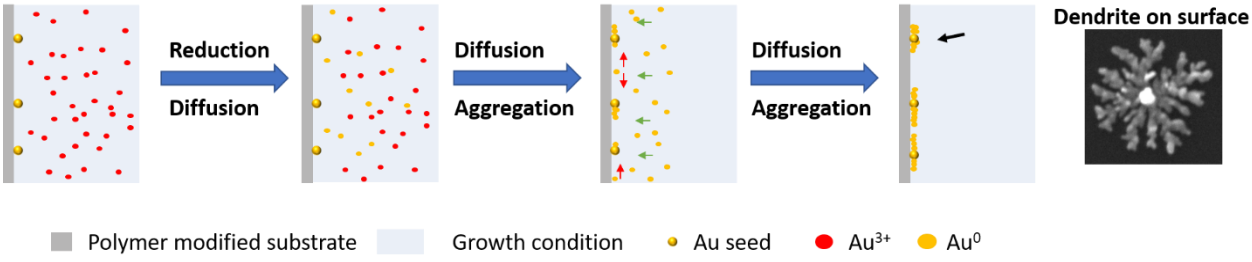

Scheme 4.2. A schematic illustration of the Au NSF formation process

4.3.3 Controls over the density, size and microfeatures of the NSFs.

From the above discussion, it can be expected that both the morphology and size of 2D Au NSFs will be greatly influenced by the number of pre-deposited seeds on the surface and by the growth rate of NSFs branches, which can be altered and fine controlled by the experimental design.

4.3.5 Pre-seed concentration

Various concentrations of Au seed were deposited onto the polymer modified substrate in order to study the change in morphology of the fabricated Au NSFs. Figure 4.3a shows the Au NSFs fabricated when the seed solution was 45 times (45 ×) diluted with nanopure water, which

reduces the concentration of Au seed from 0.71 mM to 0.047 mM. The silicon substrate is uniformly decorated with much larger 2D Au NSFs (diameter ~1000 nm) without any significant aggregation, Figure 4.3b shows a representative SEM image of an individual Au NSF. It can be clearly observed by comparison to the Au NSFs fabricated from 0.71 mM seed solution (3 × diluted, shown in Figure 4.1b), the Au NSF grown from a lower concentration of seed has a bigger core and more complex branches with nanosized roughness features. This can be explained by the decreased Au seed nucleus concentration, which leads to excessive deposition of gold atoms onto individual seeds, thereby, forming more branches. EDX elemental mapping (Figure 4.5) reveals that the NSF is indeed still composed of entirely elemental Au.

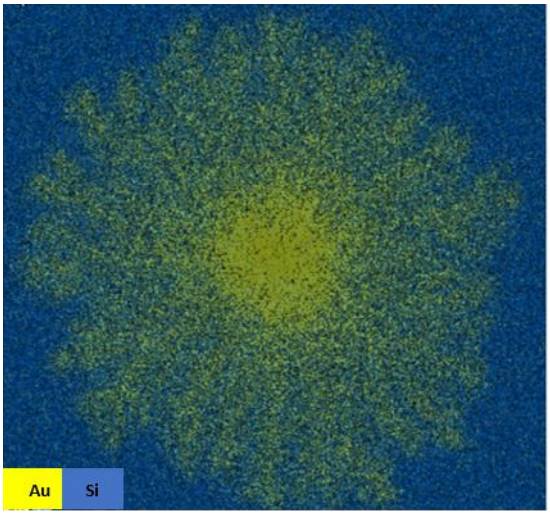

Figure 4.5. Elemental mapping result of the NSF prepared with diluted seed solution.

We also studied the variation of seed concentration versus the size of the prepared Au NSFs shown in the plot (Figure 4.3c). It clearly shows that when the seed concentration was diluted, the average size of Au NSFs increases. For instance, when the seed concentration was diluted by 10 ×, the average size of Au NSFs increases to 314 nm. The average size of Au NSFs significantly continues increasing to 580 nm as the concentration decreased to 0.0705 mM (30 × dilution). Eventually, with 45 × dilution, the average size of Au NSFs reaches to about 1000 nm.

We found that the size of Au NSFs increases nonlinearly with a decrease in seed concentration. Such results can be explained by the density of seed that deposited on the substrate.

The substrate seed densities, prepared by varying the concentration of the seed solution, were analyzed with respect to seed solution concentration and is plotted in Figure 4.6d. The densities of seeds deposited onto the substrate decreased exponentially with increased dilution. The trend in seed density is contrasting to the change in seed diameter, indicating that a higher density of seeds on substrate will lead to smaller NSFs growth. This is reasonable, since the gold source concentration remains the same and the number of seeds will determine the amount of source gold that could be consumed by individual seed. With more seeds, less gold source will be available for individual seeds.

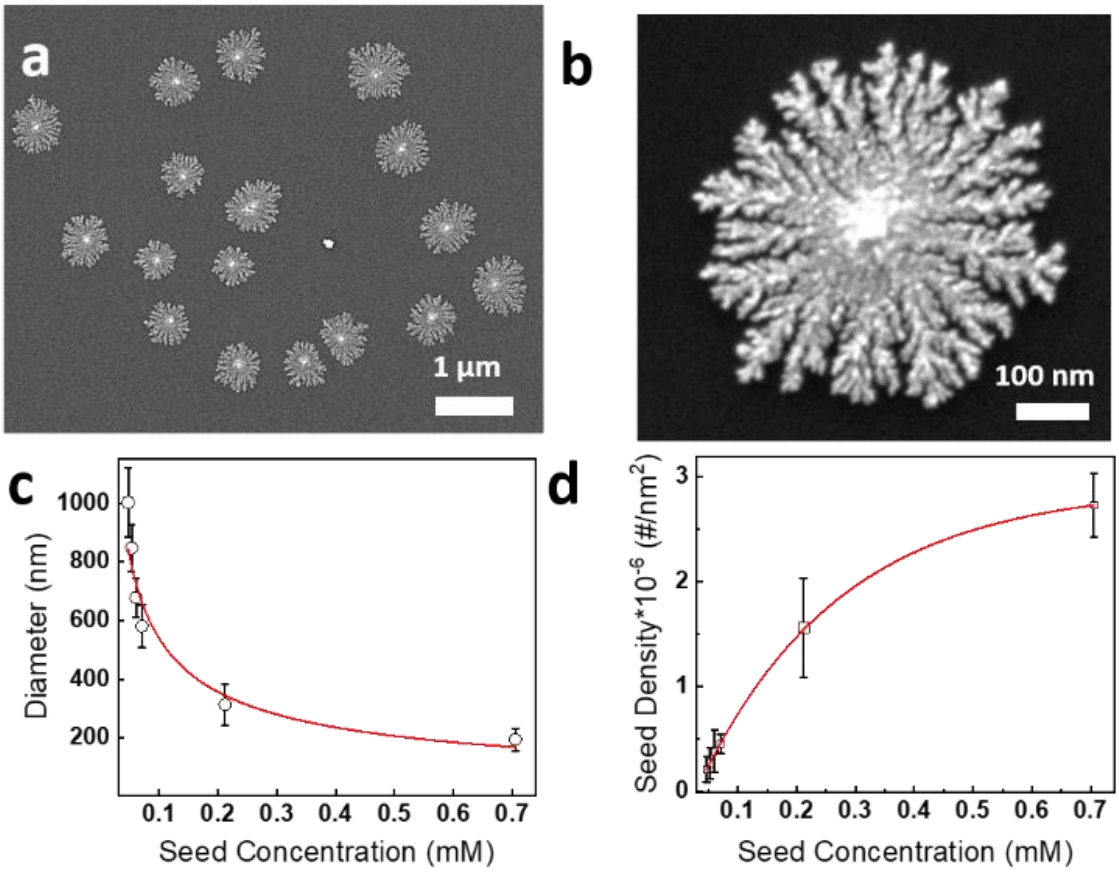

Figure 4.6. SEM images of Au NSFs fabricated with seed concentration at 0.016 mM with low magnification (a) and high magnification (b). (c) Plot of Au NSFs average diameter vs seed concentration. (d) Plot of seed density on substrate vs seed concentration.

4.3.6 pH effect

The growth solution pH effect on the morphology of Au NSFs was also studied. The pH of the growth solutions was adjusted by addition of either HCl or NaOH over the pH range of 1.69 to 4.97. The default growth solution has pH of about 3.1. As solution pH was decreased to 1.69, the color of the growth solution changes slower while at higher pH, the color change was more rapid. As shown in videos, upon the addition of hydroquinone, the growth solution at pH 1.69 takes 20 s to acquire an orange color. While the growth solution at pH 3.1 has a rapid, 2 s, transformation from colorless to brown. In the case of pH 4.97, the color changes almost instantly from colorless to dark blue. The growth solutions from pH 1.69 and 4.97 after reaction

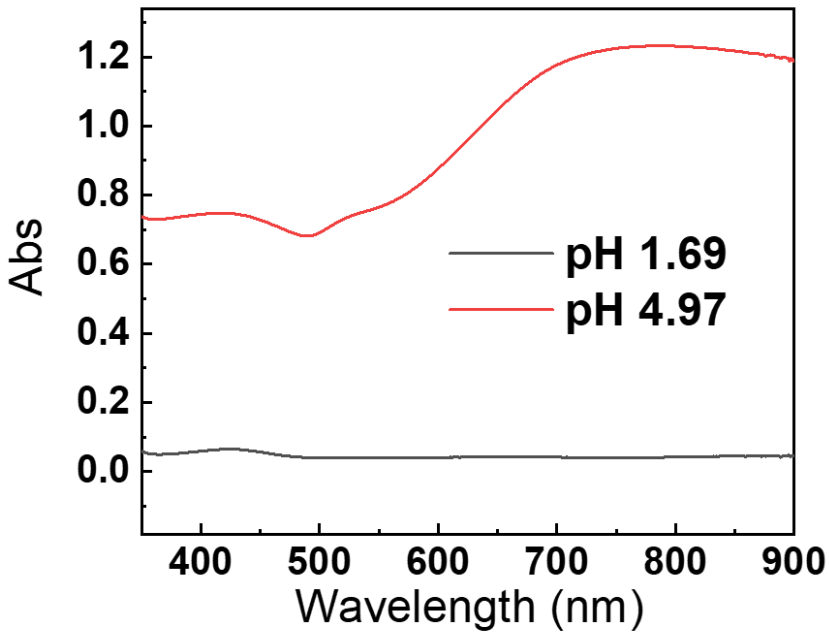

Figure 4.7. Optical extinction spectra of growth solution after the completion of fabricating Au NSFs under pH 1.69 and 4.97.

were examined by the UV-Vis spectrometer and their spectra shows a distinctive difference. Specifically, the pH 4.97 growth solution shows a broad plasmon resonance features starting at 700 nm (Figure 4.7), which has a high absorption intensity. It is highly indicative of excess gold nanoparticle formation in the growth solution. While, the UV-Vis spectrum of pH 1.69 growth solution only shows a very weak peak at 420 nm. This indicates the gold source in solution are almost immobilized on the substrate and leave nearly zero gold in solution.

SEM imaging was used to analyze the morphologies of the Au NSFs prepared in various

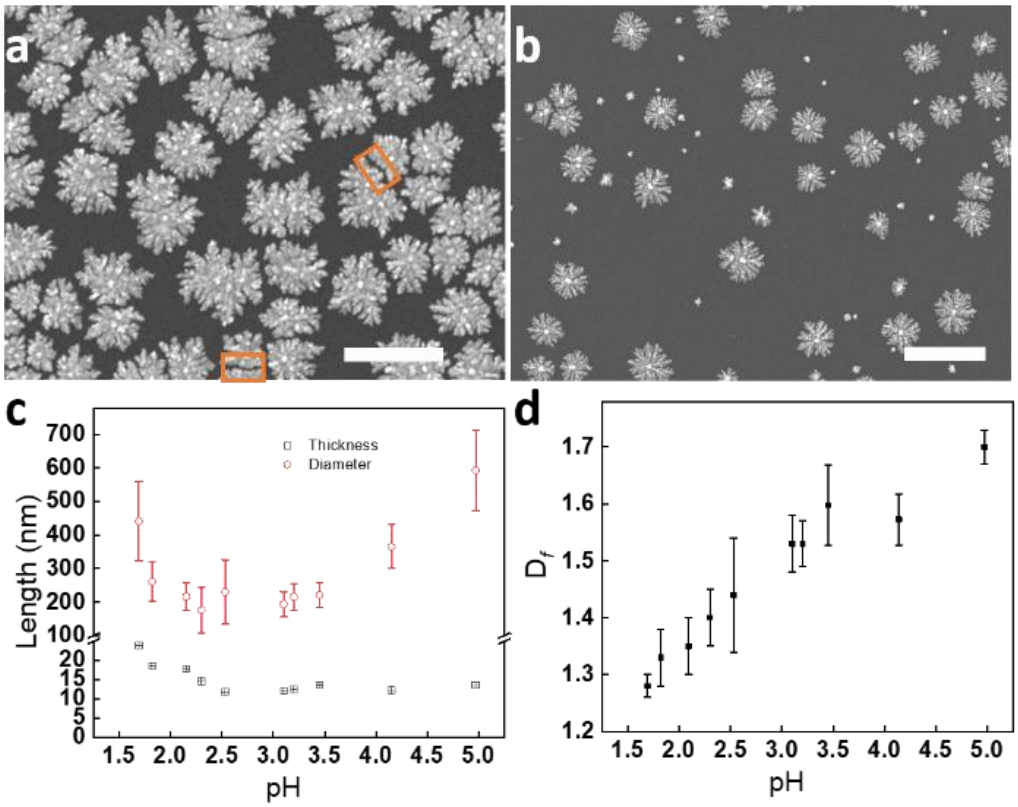

Figure 4.8: (a-b) SEM images of Au NSFs fabricated with pH of growth solutions at (a) 1.69; (b) 4.97. Scale bar: 1 µm. (c) Average length with respect to diameter and thickness of the Au NSFs with various pH growth conditions. (d) Plot of fractal dimension vs pH of growth solutions.

pH growth solutions, which confirms the transition of the structure of NSFs. Figure 4.8a, 4.8b, Figure 4.9(a-f) are representative SEM images of Au NSFs prepared in various pH growth

solutions. An important feature for all samples is that the individual branches from two neighboring seeds never cross each other, instead, a small but clear gap was formed at the converged interface. This is caused by deficiency of gold source at that location. Beyond this, from SEM images, the morphologies of NSFs from pH 1.69 to 4.97 appears significantly

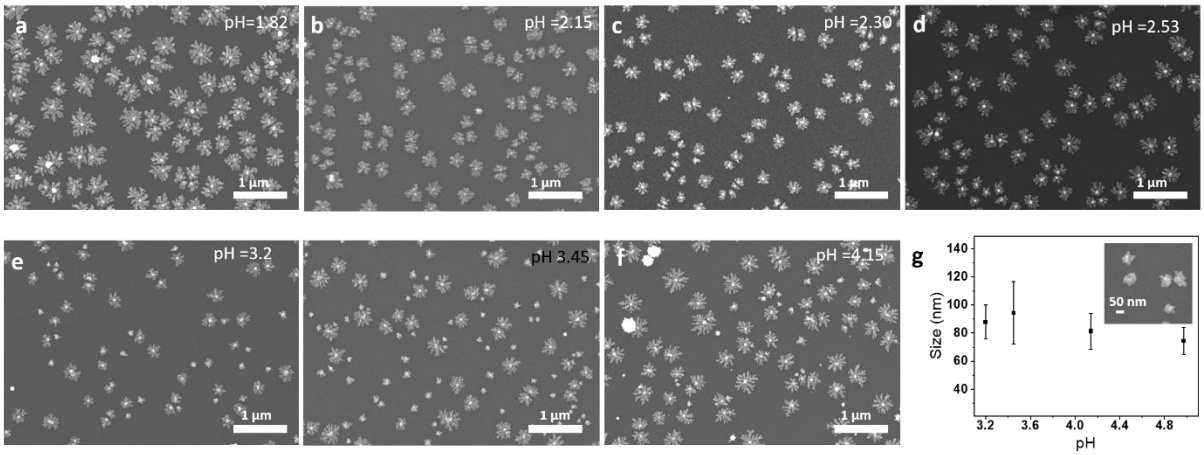

Figure 4.9. (a-f) SEM images of Au NSFs fabricated with pH of growth solutions at various pH values. Scale bar: 1 µm. (g) Average sizes of the popcorn-like nanomaterials fabricated at various pH growth conditions. Inset: A representative image of popcorn-like nanomaterials from pH 4.97. Scale bar: 100 nm.

changes. The uniformity of Au NSFs decorating on substrates appears much better on samples prepared at the pH toward acidic condition. As show in Figure 4.10, samples prepared at pH 1.69 show much higher density of Au NSFs across the substrate. Compared to the default sample prepared at pH 3.10, the structure tends to be less branched (shown in Figure 4.8a) and the diameter of the Au NSFs is larger about 441 ± 119 nm. Gaps between two Au NSFs occurs more frequently in this sample since NSFs size are larger and tend to greater proximity with neighboring seeds as is clearly shown by the two highlighted sectors in Figure 4.8a.

Yet, the sample prepared at pH 4.97 are less uniform. In addition to snowflake nanostructures, the substrates also contain 'popcorn-like' gold nanomaterials. Such structures exist on samples prepared at pH 3.20 to 4.97, as clearly shown in Figure 4.9 (e-f) and inset in Figure 4.9g. An

analysis of the popcorn-like nanomaterial demonstrated no significant size difference, about 90 nm, between samples in the higher pH range (Figure 4.9g). The structure of Au NSFs prepared at pH 4.97 shows more branches (shown in Figure 4.4b) and the diameter of the Au NSFs is larger about 592 ± 121 nm compared to the default sample prepared at pH 3.10. Figure 4.8c

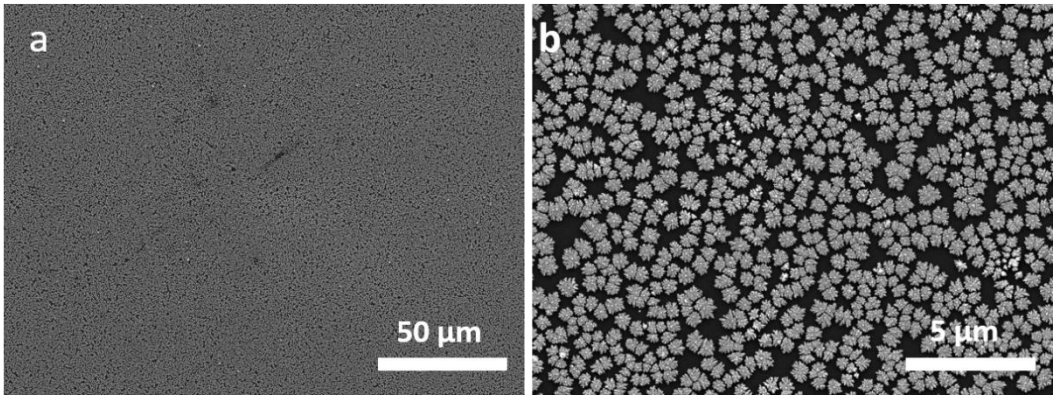

Figure 4.10. Low magnification (left) and high magnification (right) SEM images of Au NSFs fabricated with pH of growth solutions at 1.69.

shows the average length with respect to diameter and thickness of the Au NSFs with various pH growth conditions. Note that data from pH 3.20 to 4.97 eliminate the size of popcorn like nanomaterial on the substrates. It clearly shows the diameter of Au NSFs increase when decreasing the pH from 3.10 to 1.69 and increasing pH from 3.10 to 4.97. The thickness of Au NSFs, data obtained from AFM, decreases when increasing pH from 1.69 to 2.53 and keep relatively similar thickness afterwards.

The fractal pattern can be analyzed as an index of fractal dimension (D_f) by describing their convolution as the ratio of change in detail to that of scale which provides the information about the structural complexity and its efficiency, specifically in terms of covered surface area.[145] D_f is calculated by the box and counting method which has been shown to be accurate and efficient by Barabasi.[146,147] We applied the fractal dimension D_f method to evaluate the shape complexity of Au NSFs which was calculated by Fraclac Version 2.5 software developed

by ImageJ. By using the standard box counting evaluation (Details in appendix B), the values of D_f for NSFs from pH=1.69 to 4.97 have shown in Fig.4.8d. It was found that when pH increases from 1.69 to 4.97, the D_f was gradually increased which is from 1.28 ± 0.02 to 1.70 ± 0.03. This indicates that with increasing pH, the branching of fractal structures increases which can be observed from the SEM images. We note that the value of D_f =1.70 ± 0.03 which is in agreement with the 2D DLA simulation (ca. 1.7).[148,149]

From all discussed results, we suggest that the supply rate of Au^0 in higher pH growth condition is much faster than lower pH growth condition. Sodium citrate and hydroquinone are well known reducing agents whose electrochemistry has been widely studied and their impact on synthesis gold nanomaterial.[150–152] During reduction, Sodium citrate firstly reduces Au^{3+} to Au^{1+} by accepting two electrons from the citrate oxidation reaction. Once Au^{1+} are formed, hydroquinone reduces them to Au^0. Hydroquinone undergoes a two electron, two proton oxidation process, to form benzoquinone illustrated in Schematic 4.3). The influence of pH on the oxidation of reducing

Scheme 4.3. Stepwise Reduction of Au^{3+} to Au^{1+} by Sodium Citrate (Equation 1) and Au^{1+} to Au^0 by Hydroquinone (Equation 2)

Equation 1.

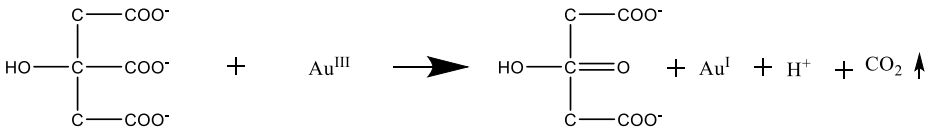

Equation 2.

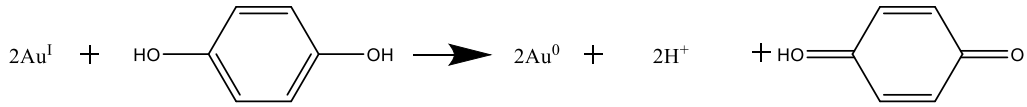

agents is important because H^+ ions are involved in the oxidation/reduction process.

When HCl is added to lower the pH of the solution, HCl provides the H^+ ions to the solution. As H^+ ions increase, the availability of electrons to reduce the Au^{3+} is reduced and the reaction rate is slowed. In accordance with Le Chatelier's principle, citrate and hydroquinone becomes less

effective and the formation rate of Au^0 is much slower. In this case, the gold seed/surface likely plays an important role as a surface- catalyzed center favoring reduction of gold atom to the exterior surface of the seed. The standard reduction potential, in the presence of seed, has been reported as 1.002 V, whereas it was -1.5 V in reducing isolated $Au^{1+}$to Au^0. Given the less effective oxidation process, hydroquinone preferentially reduces Au^{1+} on the surface of the gold seed. This can also explain the increase in thickness of Au NSF with decreasing pH of the growth solution. In addition, due to the slow deposition rate, the final Au NSFs have less branching and there FD is about 1.28, far away from 2D DLA simulation (ca. 1.7).

On the other hand, at the higher pH conditions, the reducing rate of Au^0 formation is promoted, and secondary nucleation is unavoidable. This explains the rapid color change and the appearance of a Au sphere peak in the growth solution. The Au spheres formed in solution are deposited on the substrate and give rise to the popcorn-like structures on the substrate. For the similar sizes, it is possible that sodium citate stabilized the gold which restricts the nanoparticle growth to a critical size, and hence, the nanoparticles are stable. Besides sources of Au^0 for secondary nucleation formation, there are enough Au^0 in solution which continue deposit on the surface of gold seed and forming NSFs via DLA growth. From the change of D_f values, it also suggests that the formation of the higher branched Au NSF (with higher D_f) occurs with high immobilization efficiency of Au^0 on pre-placed seeds. It is worth to mentioning that in such cases, the gold seed/gold surface play less role as surface-catalyzed centers which explains the smaller and relatively similar thickness of Au NSFs in the case of higher pH.

The XRD patterns in Figure 4.11 are carried out to acquire the structure information of NSFs fabricated under various pH conditions. XRD of samples fabricated from growth solutions at pH 4.97 and 1.69 are shown in Figure 4.11a. It is obviously that the (111) crystal facets are highly

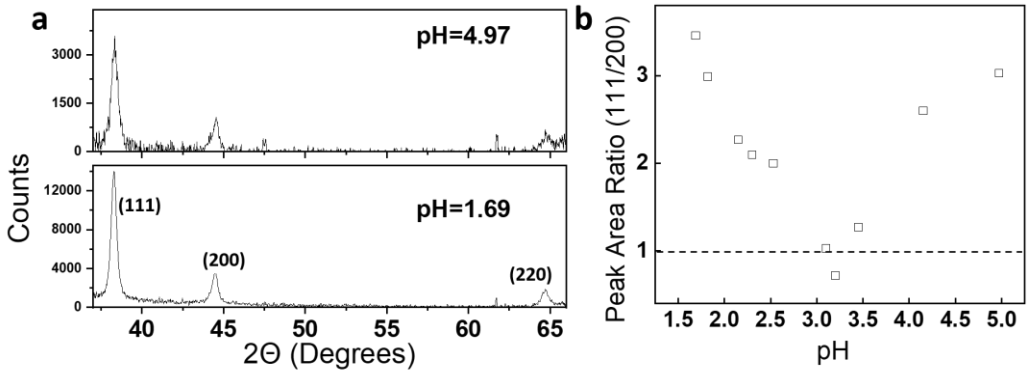

Figure 4.11. XRD patterns of Au NSFs fabricated with pH of growth solutions at (a) 4.97 and 1.69.(b) plot of Peak ratio (200/111) vs pH.

exposed as evidenced by the extremely high (111) intensity for both samples. Very high values of intensity ratio of (111)/(200) suggest that the (111) face are predominantly enriched in the samples. One clearly differences for the samples in Figure 4.11a from sample fabricated at pH 3.10 in Figure 4.1a is their diameters are larger. Thus, these observations suggest that the Au NSF grew preferentially along the (111) direction. Similar observations on Au dendrite were reported by other groups.[153,154] In addition, sample fabricated at 1.69 is much thicker and dense than other samples. This explains the high counts for this sample compared to others. Figure 4.11b is the plot of peak ratio vs. growth solution at various pH condition. This further confirms the relationship between diameter and population of plane (111) the trend on the plot is in agreement with the trend in the diameter/thickness of Au NSFs fabricated at those conditions (show in Figure 4.6c). Among all samples, only samples prepared at pH 3.1 has the intensity ratio of (111)/(200) less than 1 (the dashed line indicates this separation value). Samples

prepared at pH 3.1 also have relatively low value of diameter/thickness when compared to all other conditions.

4.3.7 Optical properties and SERS activities

Figure 4.12 gives the UV-vis-NIR spectra of four representative samples fabricated under various conditions, including pH 1.69, 3.1, 4.97 and pre-deposition of 45 times diluted seed solution which were measured from 400 nm to 1500 nm. The sample prepared at pH 3.1 shows strong absorptions at 580 nm. As is well known, the surface plasmon resonance (SPR) of Au nanomaterial greatly depends on its morphology and environment. Thus, the observed absorption spectra may represent a contour combining the size, aspect ratio and coupling factors of the hierarchical dendritic structures. For Au NSFs, with the increase in size of 2D structure, the frequency of SPR will move to the longer wavelength due to the long-range interaction of SPR in the 2D dendritic. As shown in Figure 4.12, samples prepared pH 1.69 and 4.97 give a significant red shift of SPR peak from visible to near infrared region, which is consistent with the morphology evolution of NSFs

discussed earlier. The broadened peaks may be resulted from the multiple coupling between side branches and neighboring trunks. It is worth mentioning that the broad SPR peak for NSFs at pH 1.69 can also be attributed to the much denser packing of NSFs for samples prepared under these conditions. Such dense packing can generate a significant amount of inter-structural plasmonic coupling leading to broadening of the plasmon resonance. While for the sample prepared at 45 times diluted seed solution, the spectrum shows a gradual increase in absorption from about 500

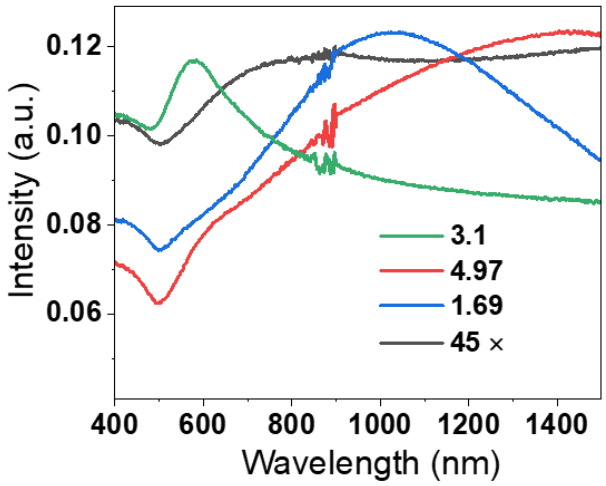

Figure 4.12: Optical extinction spectra of Au NSFs fabricated under pH 1.69, 3.1, 4.97 as well as 45 times diluted seed solution.

nm to the near-IR region without indication of leveling off. This is not surprising considering the size of Au NSF under this condition is close to a micrometer and such broadened absorption can be ascribed to the dipole and quadrupole plasmon resonances of NSFs based on the predictions produced by discrete dipole approximation simulations.[155,156]

It has been demonstrated that gold branched nanostructures contain a large number of sharp corners, edges and junctions, which act as electromagnetic "hot spots" for SERS. Hence, the SERS activities of the Au NSFs formed under pH 1.69, 3.1, 4.97 as well as 45 times diluted seeds have been assessed by using R6G as the probe molecule in Figure 4.13. In comparison to the spectrum taken on a spot without Au NSF (black), all other substrates show the characteristic vibration bands of R6G molecules which clearly appear at 612, 765, 1186, 1306, 1360, 1508, 1574, and 1650 cm^{-1}. The band at 612 cm^{-1} was assigned to the *ν*(C-C-C) in-plane stretching mode. The bands at 765

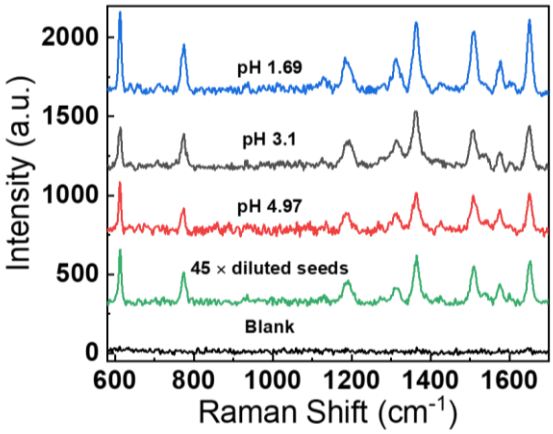

Figure 4.13. SERS spectra of substrates without Au NSFs and with the Au NSFs fabricated under pH 1.69, 3.1, 4.97 as well as 45 times diluted seeds.

and 1186 cm^{-1} were assigned to the *ν*(C-H) out-of-plane and in-plane bending modes, respectively. The bands at 1360, 1508, 1574, and 1650 cm^{-1} were related to the C-C stretching of the aromatic ring.[157] Such SERS activity is due to the decoration of Au NSFs on substrates. It is worth mentioning that for those samples, it has been observed that the SERS intensities are not uniform across the substrate. This is expected since SERS intensity varies due to the local substrate environment. The sizes and density of Au NSFs on the substrates all play a significant role in

determine the SERS activity. Thus, Figure 4.13 only demonstrates that the samples are SERS active and is not a comparison of the SERS performance among the varied substrates.

In order to understand the relationship between substrate conditions and SERS property, optical imaging and confocal Raman mapping were conducted on substrates decorated by the Au NFs obtained at pH 1.69. Figure 4.14 shows a Au NSFs decorated substrate with a scratch used to give

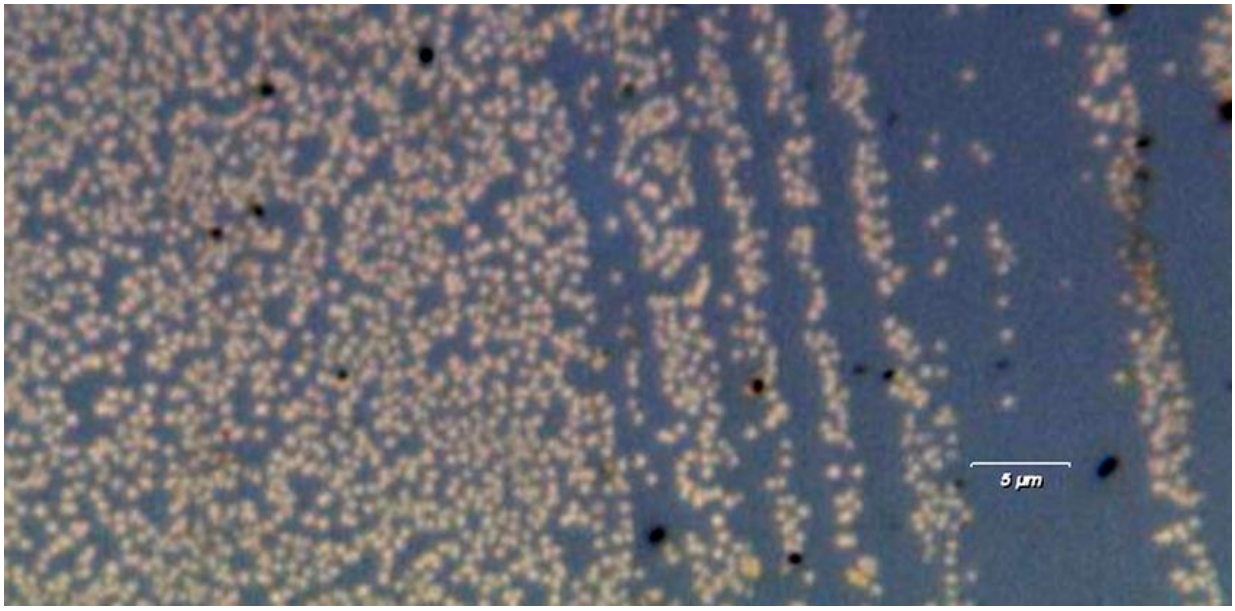

Figure 4.14. Optical image of Au NSFs decorated silicon substrate taken under 100× objective.

contrast to the Au NSFs area. The locations of the Au NSFs can be observed under an optical microscope which shows a brighter color than the area without NSFs. A typical 10 µm × 10 µm area, shown in Figure 4.15a, was investigated with the confocal Raman technique. The SERS mapping result shown in Figure 4.15b depicts the intensity distribution of the Raman peak at 1507 cm^{-1} across the whole area and the distribution of Raman hot spots can be "visualized". The strong SERS signal was obtained from the locations having Au NSFs. The Raman map shows a similar pattern to the optical image, indicating the effective SERS enhancement of Au NSFs on the substrates. In other words, the Raman map identified the location and density of the Raman hot

spots, which were generated by closely packed Au NSFs. Three Raman spectra from the represented spots (red, blue and black color in (b)) were plotted and shown in Figure 4.15c. It clearly shows that the black spot does not have any characteristic peaks of R6G which is reasonable due to lacking Au NSFs. The Red spots have much stronger SERS intensity than blue spots. By comparing optical image and SERS mapping. It can observe that the red spots are locations higher Au NSFs density while blue spots are lower in density. It is very intriguing to observe the strong SERS signal from few or individual Au NSFs, which are valuable in both the fundamental study of SERS-active substrates and in their potential applications, such as sensing technology.

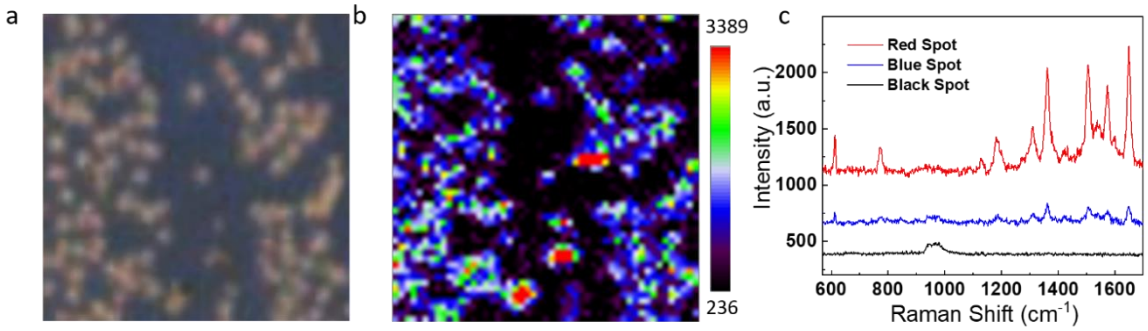

Figure 4.15 (a) Optical image of the Au NSFs decorated substrate with a scratch; (b) confocal Raman image of the same area. Size of the area: 10 μm × 10 μm. (c) Raman spectra recorded in positions (red, blue and black spots) in (b)

4.4 Conclusions

In summary, a facile method to fabricate 2D Au snowflake-like (Au NSF) nanostructures on a polymeric modified substrate has been explored, and the morphology of such nanostructures can be controlled or tuned by varying the density of seed and pH of the growth medium. The seed mediate growth is effective in controlling the number of nucleus on the substrate and thus

controlling the final morphology of the nanostructure. The SERS characterization was performed not only to demonstrate the fabricated Au NSF SERS activities, but also to study the relationship between substrate condition and SERS property. Our study demonstrated a successful approach to fabricate SERS-active dendrite 2D Au nanostructures with controlled morphologies, structures, and properties for broad applications.

4.5 Notes on the chapter

In this work with several first authors is especially important to make clear the ownership of individual contributions of work and writing. Sullivan Cohen-Pope deserves the lion share of the credit for synthetic work associated with growing the dendritic structures, as well as, all characterization with atomic-force microscopy. Electron microscopy was shared between this author, Cohen-Pope, and Maggie Wang. HR-TEM images were acquired by Dr. Helen Lavoie in the Molecular Analysis Facility at University of Washington. Alexandra Hoff was extremely helpful in the production of the free-standing polymer film and Kaitlynn Flynn was indispensable for help with data processing. Maggie Wang was also responsible for all Raman based characterization with the help of staff at the University of Washington. This author was responsible for all of the XRD characterization, STEM imaging, much of the SEM imaging and analysis, as well as, working in conjunction with Cohen-Pope on optical characterization. The writing of this document was quite divided, Cohen-Pope wrote the initial draft of the experimental section which was the edited by all authors. Wang, Cohen-Pope and myself, submitted drafts of the introduction, the final version of which is a composite of these drafts with Dr. Bao's additions. This author wrote an initial draft explaining how the observed results could be explained by the changing reduction potential of hydroquinone and how this could lead to diffusion-based aggregation at high pH and nucleated growth at low pH, and how this related to

the observed difference in relative crystal surface formation. The final work was a collaborative process containing input from Wang, Cohen-Pope, Dr. Bao and myself.

Works Cited

(1) Brown, S. D.; Nativo, P.; Smith, J.-A.; Stirling, D.; Edwards, P. R.; Venugopal, B.; Flint, D. J.; Plumb, J. A.; Graham, D.; Wheate, N. J. Gold Nanoparticles for the Improved Anticancer Drug Delivery of the Active Component of Oxaliplatin. *J. Am. Chem. Soc.* **2010**, *132* (13), 4678–4684. https://doi.org/10.1021/ja908117a.

(2) Wang, D.; Bourgeois, M. R.; Guan, J.; Fumani, A. K.; Schatz, G. C.; Odom, T. W. Lasing from Finite Plasmonic Nanoparticle Lattices. *ACS Photonics* **2020**, *7* (3), 630–636. https://doi.org/10.1021/acsphotonics.0c00231.

(3) Ahmed, E. S. A.; Sohal, H. S. Nanotechnology in Communication Engineering: Issues, Applications, and Future Possibilities. **2017**, 15.

(4) Liu, Y.; Zhou, G.; Liu, K.; Cui, Y. Design of Complex Nanomaterials for Energy Storage: Past Success and Future Opportunity. *Acc. Chem. Res.* **2017**, *50* (12), 2895–2905. https://doi.org/10.1021/acs.accounts.7b00450.

(5) Hasan, R. Md. M.; Luo, X. Promising Lithography Techniques for Next-Generation Logic Devices. *Nanomanuf Metrol* **2018**, *1* (2), 67–81. https://doi.org/10.1007/s41871-018-0016-9.

(6) Bernhoft, R. A. Mercury Toxicity and Treatment: A Review of the Literature. *Journal of Environmental and Public Health* **2012**, *2012*, 1–10. https://doi.org/10.1155/2012/460508.

(7) Gates, A. T.; Fakayode, S. O.; Lowry, M.; Ganea, G. M.; Murugeshu, A.; Robinson, J. W.; Strongin, R. M.; Warner, I. M. Gold Nanoparticle Sensor for Homocysteine Thiolactone-Induced Protein Modification. *Langmuir* **2008**, *24* (8), 4107–4113. https://doi.org/10.1021/la7033142.

(8) Park, J. S.; Kim, S. T.; Kim, S. Y.; Jo, M. G.; Choi, M. J.; Kim, M. O. A Novel Kit for Early Diagnosis of Alzheimer's Disease Using a Fluorescent Nanoparticle Imaging. *Sci Rep* **2019**, *9* (1), 13184. https://doi.org/10.1038/s41598-019-49711-y.

(9) Zuloaga, J.; Prodan, E.; Nordlander, P. Quantum Plasmonics: Optical Properties and Tunability of Metallic Nanorods. *ACS Nano* **2010**, *4* (9), 5269–5276. https://doi.org/10.1021/nn101589n.

(10) *Optics in Our Time*; Al-Amri, M. D., El-Gomati, M., Zubairy, M. S., Eds.; Springer International Publishing: Cham, 2016. https://doi.org/10.1007/978-3-319-31903-2.

(11) Wu, W.; He, Q.; Jiang, C. Magnetic Iron Oxide Nanoparticles: Synthesis and Surface Functionalization Strategies. *Nanoscale Res Lett* **2008**, *3* (11), 397–415. https://doi.org/10.1007/s11671-008-9174-9.

(12) Singh, P.; Roy, S.; Jaiswal, A. Cubic Gold Nanorattles with a Solid Octahedral Core and Porous Shell as Efficient Catalyst: Immobilization and Kinetic Analysis. *J. Phys. Chem. C* **2017**, *121* (41), 22914–22925. https://doi.org/10.1021/acs.jpcc.7b07748.

(13) Chudasama, V.; Richards, D.; Maruani, A. Antibody Fragments as Nanoparticle Targeting Ligands: A Step in the Right Direction. *Chem. Sci.* **2016**, *8*. https://doi.org/10.1039/C6SC02403C.

(14) Wang, C.; Irudayaraj, J. Gold Nanorod Probes for the Detection of Multiple Pathogens. *Small* **2008**, *4* (12), 2204–2208. https://doi.org/10.1002/smll.200800309.

(15) Liu, L.; Corma, A. Metal Catalysts for Heterogeneous Catalysis: From Single Atoms to Nanoclusters and Nanoparticles. *Chem. Rev.* **2018**, *118* (10), 4981–5079. https://doi.org/10.1021/acs.chemrev.7b00776.

(16) Stockman, M. I. Nanoplasmonics: Past, Present, and Glimpse into Future. *Opt. Express* **2011**, *19* (22), 22029. https://doi.org/10.1364/OE.19.022029.

(17) Huang, X.; El-Sayed, M. A. Gold Nanoparticles: Optical Properties and Implementations in Cancer Diagnosis and Photothermal Therapy. *Journal of Advanced Research* **2010**, *1* (1), 13–28. https://doi.org/10.1016/j.jare.2010.02.002.

(18) Abbas, A.; Tian, L.; Morrissey, J. J.; Kharasch, E. D.; Singamaneni, S. Hot Spot-Localized Artificial Antibodies for Label-Free Plasmonic Biosensing. *Adv Funct Mater* **2013**, *23* (14), 1789–1797. https://doi.org/10.1002/adfm.201202370.

(19) Hu, F.; Zhang, Y.; Chen, G.; Li, C.; Wang, Q. Double-Walled Au Nanocage/SiO2 Nanorattles: Integrating SERS Imaging, Drug Delivery and Photothermal Therapy. *Small* **2015**, *11* (8), 985–993. https://doi.org/10.1002/smll.201401360.

(20) Du, Y.; Liu, R.; Liu, B.; Wang, S.; Han, M.-Y.; Zhang, Z. Surface-Enhanced Raman Scattering Chip for Femtomolar Detection of Mercuric Ion (II) by Ligand Exchange. *Anal. Chem.* **2013**, *85* (6), 3160–3165. https://doi.org/10.1021/ac303358w.

(21) Ando, J.; Fujita, K.; Smith, N. I.; Kawata, S. Dynamic SERS Imaging of Cellular Transport Pathways with Endocytosed Gold Nanoparticles. *Nano Lett.* **2011**, *11* (12), 5344–5348. https://doi.org/10.1021/nl202877r.

(22) Kumari, G.; Zhang, X.; Devasia, D.; Heo, J.; Jain, P. K. Watching Visible Light-Driven CO_2 Reduction on a Plasmonic Nanoparticle Catalyst. *ACS Nano* **2018**, *12* (8), 8330–8340. https://doi.org/10.1021/acsnano.8b03617.

(23) Cao, J.; Sun, T.; Grattan, K. T. V. Gold Nanorod-Based Localized Surface Plasmon Resonance Biosensors: A Review. *Sensors and Actuators B: Chemical* **2014**, *195*, 332–351. https://doi.org/10.1016/j.snb.2014.01.056.

(24) Savage, N. Photonics: Trick of the Light. *Nature* **2013**, *495* (7440), S8–S9. https://doi.org/10.1038/495S8a.

(25) Silverman, P. J. Extreme Ultraviolet Lithography: Overview and Development Status. *J. Micro/Nanolith. MEMS MOEMS* **2005**, *4* (1), 011006. https://doi.org/10.1117/1.1862647.

(26) Watt, F.; Bettiol, A. A.; Van Kan, J. A.; Teo, E. J.; Breese, M. B. H. ION BEAM LITHOGRAPHY AND NANOFABRICATION: A REVIEW. *Int. J. Nanosci.* **2005**, *04* (03), 269–286. https://doi.org/10.1142/S0219581X05003139.

(27) Kim, F.; Song, J. H.; Yang, P. Photochemical Synthesis of Gold Nanorods. *J. Am. Chem. Soc.* **2002**, *124* (48), 14316–14317. https://doi.org/10.1021/ja028110o.

(28) Nikoobakht, B.; El-Sayed, M. A. Preparation and Growth Mechanism of Gold Nanorods (NRs) Using Seed-Mediated Growth Method. *Chem. Mater.* **2003**, *15* (10), 1957–1962. https://doi.org/10.1021/cm020732l.

(29) Indrasekara, A. S. D. S.; Wadams, R. C.; Fabris, L. Ligand Exchange on Gold Nanorods: Going Back to the Future. *Particle & Particle Systems Characterization* **2014**, *31* (8), 819–838. https://doi.org/10.1002/ppsc.201400006.

(30) Wu, C.; Xu, Q.-H. Stable and Functionable Mesoporous Silica-Coated Gold Nanorods as Sensitive Localized Surface Plasmon Resonance (LSPR) Nanosensors. *Langmuir* **2009**, *25* (16), 9441–9446. https://doi.org/10.1021/la900646n.

(31) Wang, F.; Cheng, S.; Bao, Z.; Wang, J. Anisotropic Overgrowth of Metal Heterostructures Induced by a Site-Selective Silica Coating. *Angewandte Chemie International Edition* **2013**, *52* (39), 10344–10348. https://doi.org/10.1002/anie.201304364.

(32) Zhu, X.; Jia, H.; Zhu, X.-M.; Cheng, S.; Zhuo, X.; Qin, F.; Yang, Z.; Wang, J. Selective Pd Deposition on Au Nanobipyramids and Pd Site-Dependent Plasmonic Photocatalytic Activity. *Adv. Funct. Mater.* **2017**, *27* (22), 1700016. https://doi.org/10.1002/adfm.201700016.

(33) Hinman, J. G.; Eller, J. R.; Lin, W.; Li, J.; Li, J.; Murphy, C. J. Oxidation State of Capping Agent Affects Spatial Reactivity on Gold Nanorods. *J. Am. Chem. Soc.* **2017**, *139* (29), 9851–9854. https://doi.org/10.1021/jacs.7b06391.

(34) Oesterhelt, F.; Rief, M.; Gaub, H. E. Single Molecule Force Spectroscopy by AFM Indicates Helical Structure of Poly(Ethylene-Glycol) in Water. *New J. Phys.* **1999**, *1*, 6–6. https://doi.org/10.1088/1367-2630/1/1/006.

(35) López-Lozano, X.; Barron, H.; Mottet, C.; Weissker, H.-C. Aspect-Ratio- and Size-Dependent Emergence of the Surface-Plasmon Resonance in Gold Nanorods – an Ab Initio TDDFT Study. *Phys. Chem. Chem. Phys.* **2014**, *16* (5), 1820–1823. https://doi.org/10.1039/C3CP53702A.

(36) Alizadeh, T.; Ganjali, M. R.; Zare, M. Application of an Hg2+ Selective Imprinted Polymer as a New Modifying Agent for the Preparation of a Novel Highly Selective and Sensitive Electrochemical Sensor for the Determination of Ultratrace Mercury Ions. *Anal Chim Acta* **2011**, *689* (1), 52–59. https://doi.org/10.1016/j.aca.2011.01.036.

(37) Chen, L.; Lu, L.; Wang, S.; Xia, Y. Valence States Modulation Strategy for Picomole Level Assay of Hg^{2+} in Drinking and Environmental Water by Directional Self-Assembly of Gold Nanorods. *ACS Sens.* **2017**, *2* (6), 781–788. https://doi.org/10.1021/acssensors.7b00149.

(38) Chen, L.; Fu, X.; Lu, W.; Chen, L. Highly Sensitive and Selective Colorimetric Sensing of Hg^{2+} Based on the Morphology Transition of Silver Nanoprisms. *ACS Appl. Mater. Interfaces* **2013**, *5* (2), 284–290. https://doi.org/10.1021/am3020857.

(39) Li, L.; Zhang, L.; Zhao, Y.; Chen, Z. Colorimetric Detection of Hg(II) by Measurement the Color Alterations from the “before” and “after” RGB Images of Etched Triangular Silver Nanoplates. *Microchim Acta* **2018**, *185* (4), 235. https://doi.org/10.1007/s00604-018-2759-9.

(40) Chen, W.; Lei, W.; Xue, M.; Xue, F.; Meng, Z.; Zhang, W.; Qu, F.; Shea, K. J. Protein Recognition by a Surface Imprinted Colloidal Array. *J. Mater. Chem. A* **2014**, *2* (20), 7165. https://doi.org/10.1039/c4ta00048j.

(41) Lei, W.; Meng, Z.; Zhang, W.; Zhang, L.; Xue, M.; Wang, W. “Induced Fit” Recognition of Proteins by Surface Imprinted Silica with “Soft” Recognition Sites. *Talanta* **2012**, *99*, 966–971. https://doi.org/10.1016/j.talanta.2012.07.067.

(42) Placido, T.; Aragay, G.; Pons, J.; Comparelli, R.; Curri, M. L.; Merkoçi, A. Ion-Directed Assembly of Gold Nanorods: A Strategy for Mercury Detection. *ACS Appl. Mater. Interfaces* **2013**, *5* (3), 1084–1092. https://doi.org/10.1021/am302870b.

(43) Chang, W.-S.; Ha, J. W.; Slaughter, L. S.; Link, S. Plasmonic Nanorod Absorbers as Orientation Sensors. *Proceedings of the National Academy of Sciences* **2010**, *107* (7), 2781–2786. https://doi.org/10.1073/pnas.0910127107.

(44) Parab, H.; Jung, C.; Woo, M.-A.; Park, H. G. An anisotropic snowflake-like structural assembly of polymer-capped gold nanoparticles. *J. Nanopart. Res* **2011**, *13* (5), 2173–2180.

(45) Jaiswal, A.; Tian, L.; Tadepalli, S.; Liu, K.; Fei, M.; Farrell, M. E.; Pellegrino, P. M.; Singamaneni, S. Plasmonic Nanorattles with Intrinsic Electromagnetic Hot-Spots for Surface Enhanced Raman Scattering. *Small* **2014**, *10* (21), 4287–4292. https://doi.org/10.1002/smll.201401278.

(46) Liu, H.; Chen, D.; Li, L.; Liu, T.; Tan, L.; Wu, X.; Tang, F. Multifunctional Gold Nanoshells on Silica Nanorattles: A Platform for the Combination of Photothermal Therapy and Chemotherapy with Low Systemic Toxicity. *Angew. Chem. Int. Ed.* **2011**, *50* (4), 891–895. https://doi.org/10.1002/anie.201002820.

(47) Krenkel, P. A.; Goldwater, L. Mercury: Environmental Considerations, Part I. *null* **1973**, *3* (1–4), 303–373. https://doi.org/10.1080/10643387309381605.

(48) Clarkson, T. W.; Stockinger, H. Recent Advances in the Toxicology of Mercury with Emphasis on the Alkylmercurials. *Crit. Rev. Toxicol* **1972**, *1* (2), 203–234.

(49) Rice, K. M.; Walker, E. M.; Wu, M.; Gillette, C.; Blough, E. R. Environmental Mercury and Its Toxic Effects. *J Prev Med Public Health* **2014**, *47* (2), 74–83.

(50) Morel, F. M. M.; Kraepiel, A. M. L.; Amyot, M. The Chemical Cycle and Bioaccumulation of Mercury. *Annu. Rev. Ecol. Evol. Syst* **1998**, *29* (1), 543–566.

(51) Gómez-Ariza, J. L.; Lorenzo, F.; García-Barrera, T. Comparative Study of Atomic Fluorescence Spectroscopy and Inductively Coupled Plasma Mass Spectrometry for Mercury and Arsenic Multispeciation. *Anal. Bioanal. Chem* **2005**, *382* (2), 485–492.

(52) Bloom, N.; Fitzgerald, W. F. Determination of Volatile Mercury Species at the Picogram Level by Low-Temperature Gas Chromatography with Cold-Vapour Atomic Fluorescence Detection. *Anal. Chim. Acta* **1988**, *208*, 151–161.

(53) Tang, S.; Tong, P.; Lu, W.; Chen, J.; Yan, Z.; Zhang, L. A Novel Label-Free Electrochemical Sensor for Hg2+ Based on the Catalytic Formation of Metal Nanoparticle. *Biosens. Bioelectron* **2014**, *59*, 1–5.

(54) Cai, S.; Lao, K.; Lau, C.; Lu, J. Turn-on" Chemiluminescence Sensor for the Highly Selective and Ultrasensitive Detection of Hg2+ Ions Based on Interstrand Cooperative Coordination and Catalytic Formation of Gold Nanoparticles. *Anal. Chem* **2011**, *83* (24), 9702–9708.

(55) Ding, Y.; Wang, S.; Li, J.; Chen, L. Nanomaterial-Based Optical Sensors for Mercury Ions. *TrAC, Trends Anal. Chem* **2016**, *82*, 175–190.

(56) Annadhasan, M.; Muthukumarasamyvel, T.; Sankar Babu, V. R.; Rajendiran, N. Green Synthesized Silver and Gold Nanoparticles for Colorimetric Detection of Hg2+, Pb2+, and Mn2+ in Aqueous Medium. *ACS Sustain. Chem. Eng* **2014**, *2* (4), 887–896.

(57) Chen, G.-H.; Chen, W.-Y.; Yen, Y.-C.; Wang, C.-W.; Chang, H.-T.; Chen, C.-F. Detection of Mercury(II) Ions Using Colorimetric Gold Nanoparticles on Paper-Based Analytical Devices. *Anal. Chem* **2014**, *86* (14), 6843–6849.

(58) Zhang, Z.; Wang, H.; Chen, Z.; Wang, X.; Choo, J.; Chen, L. Plasmonic Colorimetric Sensors Based on Etching and Growth of Noble Metal Nanoparticles: Strategies and Applications. *Biosens. Bioelectron* **2018**, *114*, 52–65.

(59) Chen, L.; Li, J.; Chen, L. Colorimetric Detection of Mercury Species Based on Functionalized Gold Nanoparticles. *ACS Appl. Mater. Interfaces* **2014**, *6* (18), 15897–15904.

(60) Lou, T.; Chen, Z.; Wang, Y.; Chen, L. Blue-to-Red Colorimetric Sensing Strategy for Hg2+ and Ag+ Via Redox-Regulated Surface Chemistry of Gold Nanoparticles. *ACS Appl. Mater. Interfaces* **2011**, *3* (5), 1568–1573.

(61) Bhattacharjee, Y.; Chatterjee, D.; Chakraborty, A. Mercaptobenzoheterocyclic Compounds Functionalized Silver Nanoparticle, an Ultrasensitive Colorimetric Probe for Hg(II) Detection in Water with Picomolar Precision: A Correlation between Sensitivity and Binding Affinity. *Sens. Actuators B Chem* **2018**, *255*, 210–216.

(62) Peng, C.-F.; Pan, N.; Xie, Z.-J.; Wu, L.-L. Highly Sensitive and Selective Colorimetric Detection of Hg2+ Based on the Separation of Hg2+ and Formation of Catalytic DNA–Gold Nanoparticles. *Anal. Methods* **2016**, *8* (5), 1021–1025.

(63) Lee, J.-S.; Han, M. S.; Mirkin, C. A. Colorimetric Detection of Mercuric Ion (Hg2+) in Aqueous Media Using DNA-Functionalized Gold Nanoparticles. *Angew. Chem. Int. Ed* **2007**, *46* (22), 4093–4096.

(64) Chen, L.; Lou, T.; Yu, C.; Kang, Q.; Chen, L. N-1-(2-Mercaptoethyl)Thymine Modification of Gold Nanoparticles: A Highly Selective and Sensitive Colorimetric Chemosensor for Hg2+. *Analyst* **2011**, *136* (22), 4770–4773.

(65) Maity, D.; Kumar, A.; Gunupuru, R.; Paul, P. Colorimetric Detection of Mercury(II) in Aqueous Media with High Selectivity Using Calixarene Functionalized Gold Nanoparticles. *Colloids Surf., A* **2014**, *455*, 122–128.

(66) Xu, D.; Yu, S.; Yin, Y.; Wang, S.; Lin, Q.; Yuan, Z. Sensitive Colorimetric Hg2+ Detection via Amalgamation-Mediated Shape Transition of Gold Nanostars. *Front Chem* **2018**, *6*. https://doi.org/10.3389/fchem.2018.00566.

(67) Wang, M.; Hoff, A.; Doebler, J. E.; Emory, S. R.; Bao, Y. Dumbbell-Like Silica Coated Gold Nanorods and Their Plasmonic Properties. *Langmuir* **2019**, *35* (51), 16886–16892.

(68) Bao, Y.; Fong, H.; Jiang, C. Manipulating the Collective Surface Plasmon Resonances of Aligned Gold Nanorods in Electrospun Composite Nanofibers. *J. Phys. Chem. C* **2013**, *117* (41), 21490–21497.

(69) Chang, H.-H.; Gole, M. T.; Murphy, C. J. A Golden Time for Nanotechnology. *MRS Bull* **2020**, *45* (5), 387–393.

(70) Rex, M.; Hernandez, F. E.; Campiglia, A. D. Pushing the Limits of Mercury Sensors with Gold Nanorods. *Anal. Chem.* **2006**, *78* (2), 445–451. https://doi.org/10.1021/ac051166r.

(71) Bao, Y.; Vigderman, L.; Zubarev, E. R.; Jiang, C. Robust Multilayer Thin Films Containing Cationic Thiol-Functionalized Gold Nanorods for Tunable Plasmonic Properties. *Langmuir* **2012**, *28* (1), 923–930.

(72) Lee, S.; Anderson, L. J. E.; Payne, C. M.; Hafner, J. H. Structural Transition in the Surfactant Layer That Surrounds Gold Nanorods as Observed by Analytical Surface-Enhanced Raman Spectroscopy. *Langmuir* **2011**, *27* (24), 14748–14756.

(73) Zhang, Z.; Lin, M. Fast Loading of PEG–SH on Ctab-Protected Gold Nanorods. *RSC Adv* **2014**, *4* (34), 17760–17767.

(74) Hubert, F.; Testard, F.; Spalla, O. Cetyltrimethylammonium Bromide Silver Bromide Complex as the Capping Agent of Gold Nanorods. *Langmuir* **2008**, *24* (17), 9219–9222.

(75) Kreke, P. J.; Magid, L. J.; Gee, J. C. 1h and 13c NMR Studies of Mixed Counterion, Cetyltrimethylammonium Bromide/Cetyltrimethylammonium Dichlorobenzoate, Surfactant Solutions: The Intercalation of Aromatic Counterions. *Langmuir* **1996**, *12* (3), 699–705.

(76) Chang, J.-Y.; Wu, H.; Chen, H.; Ling, Y.-C.; Tan, W. Oriented Assembly of Au Nanorods Using Biorecognition System. *Chem. Commun* **2005**, *8*, 1092–1094.

(77) Mertens, S. F. L.; Gara, M.; Sologubenko, A. S.; Mayer, J.; Szidat, S.; Krämer, K. W.; Jacob, T.; Schiffrin, D. J.; Wandlowski, T. Au@Hg Nanoalloy Formation Through Direct Amalgamation: Structural, Spectroscopic, and Computational Evidence for Slow Nanoscale Diffusion. *Adv. Funct. Mater.* **2011**, *21* (17), 3259–3267. https://doi.org/10.1002/adfm.201100409.

(78) Schulz, F.; Friedrich, W.; Hoppe, K.; Vossmeyer, T.; Weller, H.; Lange, H. Effective PEGylation of Gold Nanorods. *Nanoscale* **2016**, *8* (13), 7296–7308. https://doi.org/10.1039/C6NR00607H.

(79) Lin, C.-Y.; Yu, C.-J.; Lin, Y.-H.; Tseng, W.-L. Colorimetric Sensing of Silver(I) and Mercury(II) Ions Based on an Assembly of Tween 20-Stabilized Gold Nanoparticles. *Anal. Chem* **2010**, *82* (16), 6830–6837.

(80) Huang, J.; Park, J.; Wang, W.; Murphy, C. J.; Cahill, D. G. Ultrafast Thermal Analysis of Surface Functionalized Gold Nanorods in Aqueous Solution. *ACS Nano* **2013**, *7* (1), 589–597.

(81) Wang, N.; Liu, G.; Dai, H.; Ma, H.; Lin, M. Spectroscopic Evidence for Electrochemical Effect of Mercury Ions on Gold Nanoparticles. *Analytica Chimica Acta* **2019**, *1062*, 140–146. https://doi.org/10.1016/j.aca.2019.02.037.

(82) Duan, Q.-Q.; Zhou, J.-L.; Li, P.-W.; Sun, L.; Zhuo, K.; Zhang, Y.-X.; Zhang, W.-D.; Sang, S.-B. High-Sensitivity Mercury Ion Detection System Using Unmodified Gold Nanorods. *Chinese Journal of Analytical Chemistry* **2018**, *46* (9), e1874–e1879. https://doi.org/10.1016/S1872-2040(18)61112-0.

(83) Jin, L.-H.; Han, C.-S. Eco-Friendly Colorimetric Detection of Mercury(II) Ions Using Label-Free Anisotropic Nanogolds in Ascorbic Acid Solution. *Sensors and Actuators B: Chemical* **2014**, *195*, 239–245. https://doi.org/10.1016/j.snb.2014.01.020.

(84) Chen, L.; Lu, L.; Wang, S.; Xia, Y. Valence States Modulation Strategy for Picomole Level Assay of Hg2+ in Drinking and Environmental Water by Directional Self-Assembly of Gold Nanorods. *ACS Sensors* **2017**, *2* (6), 781–788.

(85) Yuan, A.; Wu, X.; Li, X.; Hao, C.; Xu, C.; Kuang, H. Au@gap@AuAg Nanorod Side-by-Side Assemblies for Ultrasensitive SERS Detection of Mercury and Its Transformation. *Small* **2019**, *15* (27), 1901958. https://doi.org/10.1002/smll.201901958.

(86) Song, C.; Yang, B.; Zhu, Y.; Yang, Y.; Wang, L. Ultrasensitive Sliver Nanorods Array SERS Sensor for Mercury Ions. *Biosensors and Bioelectronics* **2017**, *87*, 59–65. https://doi.org/10.1016/j.bios.2016.07.097.

(87) Liu, Y.; Huang, C. Z. Real-Time Dark-Field Scattering Microscopic Monitoring of the in Situ Growth of Single Ag@Hg Nanoalloys. *ACS Nano* **2013**, *7* (12), 11026–11034.

(88) Gu, B.; Bian, Y.; Miller, C. L.; Dong, W.; Jiang, X.; Liang, L. Mercury Reduction and Complexation by Natural Organic Matter in Anoxic Environments. *Proc. Natl. Acad. Sci* **2011**, *108* (4), 1479–1483.

(89) Skyllberg, U.; Bloom, P. R.; Qian, J.; Lin, C.-M.; Bleam, W. F. Complexation of Mercury(II) in Soil Organic Matter: Exafs Evidence for Linear Two-Coordination with Reduced Sulfur Groups. *Environ. Sci. Technol* **2006**, *40* (13), 4174–4180.

(90) Schuster, E. The Behavior of Mercury in the Soil with Special Emphasis on Complexation and Adsorption Processes - a Review of the Literature. *Water Air Soil Pollut* **1991**, *56* (1), 667–680.

(91) Liu, D.; Qu, W.; Chen, W.; Zhang, W.; Wang, Z.; Jiang, X.; Sensitive, H. Colorimetric Detection of Mercury(II) in Aqueous Media by Quaternary Ammonium Group-Capped Gold Nanoparticles at Room Temperature. *Anal. Chem* **2010**, *82* (23), 9606–9610.

(92) Thomas, K. G.; Zajicek, J.; Kamat, P. V. Surface Binding Properties of Tetraoctylammonium Bromide-Capped Gold Nanoparticles. *Langmuir* **2002**, *18* (9), 3722–3727.

(93) Dawson, A.; Kamat, P. V. Complexation of Gold Nanoparticles with Radiolytically Generated Thiocyanate Radicals ((Scn)2•. *J. Mater. Chem. B* **2000**, *104* (50), 11842–11846.

(94) Johnson, C. J.; Dujardin, E.; Davis, S. A.; Murphy, C. J.; Mann, S. Growth and Form of Gold Nanorods Prepared by Seed-Mediated, Surfactant-Directed Synthesis. *J. Mater. Chem* **2002**, *12* (6), 1765–1770.

(95) Fan, Z.; Huang, X.; Han, Y.; Bosman, M.; Wang, Q.; Zhu, Y.; Liu, Q.; Li, B.; Zeng, Z.; Wu, J.; Shi, W.; Li, S.; Gan, C. L.; Zhang, H. Surface Modification-Induced Phase Transformation of Hexagonal Close-Packed Gold Square Sheets. *Nat. Commun* **2015**, *6* (1), 6571.

(96) Diroll, B. T.; Schaller, R. D. Shape-Selective Optical Transformations of Cdse Nanoplatelets Driven by Halide Ion Ligand Exchange. *Chem. Mater* **2019**, *31* (9), 3556–3563.

(97) Antanovich, A.; Achtstein, A. W.; Matsukovich, A.; Prudnikau, A.; Bhaskar, P.; Gurin, V.; Molinari, M.; Artemyev, M. A Strain-Induced Exciton Transition Energy Shift in Cdse Nanoplatelets: The Impact of an Organic Ligand Shell. *Nanoscale* **2017**, *9* (45), 18042–18053.

(98) Guo, C.; Yarger, J. L. Characterizing Gold Nanoparticles by NMR Spectroscopy. *Magn. Reson. Chem* **2018**, *56* (11), 1074–1082.

(99) Hens, Z.; Martins, J. C. A Solution NMR Toolbox for Characterizing the Surface Chemistry of Colloidal Nanocrystals. *Chem. Mater* **2013**, *25* (8), 1211–1221.

(100) Qian, H.; Zhu, M.; Gayathri, C.; Gil, R. R.; Jin, R. Chirality in Gold Nanoclusters Probed by NMR Spectroscopy. *ACS Nano* **2011**, *5* (11), 8935–8942.

(101) Gautier, C.; Bürgi, T. Chiral Gold Nanoparticles. *ChemPhysChem* **2009**, *10* (3), 483–492.

(102) Noguez, C.; Garzón, I. L. Optically Active Metal Nanoparticles. *Chem. Soc. Rev* **2009**, *38* (3), 757–771.

(103) Hong, Y.; Lee, E.; Choi, J.; Oh, S. J.; Haam, S.; Huh, Y.-M.; Yoon, D. S.; Suh, J.-S.; Yang, J. Gold Nanorod-Mediated Photothermal Modulation for Localized Ablation of Cancer Cells. *J. Nanomater* **2012**, 825060.

(104) Mahmoud, N. N.; Alhusban, A. A.; Ali, J. I.; Al-Bakri, A. G.; Hamed, R.; Khalil, E. A. Preferential Accumulation of Phospholipid-Peg and Cholesterol-Peg Decorated Gold Nanorods into Human Skin Layers and Their Photothermal-Based Antibacterial Activity. *Sci. Rep* **2019**, *9* (1), 5796.

(105) Schuetze, B.; Mayer, C.; Loza, K.; Gocyla, M.; Heggen, M.; Epple, M. Conjugation of Thiol-Terminated Molecules to Ultrasmall 2nm Gold Nanoparticles Leads to Remarkably Complex 1h-NMR Spectra. *J. Mater. Chem. B* **2016**, *4* (12), 2179–2189.

(106) Stocker, H.; Nabers, A.; Perna, L.; Möllers, T.; Rujescu, D.; Hartmann, A.; Holleczek, B.; Schöttker, B.; Gerwert, K.; Brenner, H. Prediction of Alzheimer's Disease Diagnosis within 14 Years through Aβ Misfolding in Blood Plasma Compared to APOE4 Status, and Other Risk Factors. *Alzheimer's & Dementia* **2020**, *16* (2), 283–291. https://doi.org/10.1016/j.jalz.2019.08.189.

(107) Zhu, L.; Yang, X.; Cao, Y. Preparation of Surface-Imprinted Polymer Magnetic Nanoparticles with Miniemulsion Polymerization for Recognition of Salicylic Acid. *Analytical Letters* **2013**, *46* (6), 982–998. https://doi.org/10.1080/00032719.2012.745089.

(108) Erdem, Ö.; Saylan, Y.; Andaç, M.; Denizli, A. Molecularly Imprinted Polymers for Removal of Metal Ions: An Alternative Treatment Method. *Biomimetics* **2018**, *3* (4), 38. https://doi.org/10.3390/biomimetics3040038.

(109) Shiomi, T.; Matsui, M.; Mizukami, F.; Sakaguchi, K. A Method for the Molecular Imprinting of Hemoglobin on Silica Surfaces Using Silanes. *Biomaterials* **2005**, *26* (27), 5564–5571. https://doi.org/10.1016/j.biomaterials.2005.02.007.

(110) Cumbo, A.; Lorber, B.; Corvini, P. F.-X.; Meier, W.; Shahgaldian, P. A Synthetic Nanomaterial for Virus Recognition Produced by Surface Imprinting. *Nat Commun* **2013**, *4* (1), 1503. https://doi.org/10.1038/ncomms2529.

(111) Riskin, M.; Tel-Vered, R.; Lioubashevski, O.; Willner, I. Ultrasensitive Surface Plasmon Resonance Detection of Trinitrotoluene by a Bis-Aniline-Cross-Linked Au Nanoparticles Composite. *J. Am. Chem. Soc.* **2009**, *131* (21), 7368–7378. https://doi.org/10.1021/ja9001212.

(112) Matsui, J.; Akamatsu, K.; Hara, N.; Miyoshi, D.; Nawafune, H.; Tamaki, K.; Sugimoto, N. SPR Sensor Chip for Detection of Small Molecules Using Molecularly Imprinted Polymer with Embedded Gold Nanoparticles. *Anal. Chem.* **2005**, *77* (13), 4282–4285. https://doi.org/10.1021/ac050227i.

(113) Plasmonics & Surface Plasmon Resonance.

(114) Crockett, J. R.; Win-Piazza, H.; Doebler, J. E.; Luan, T.; Bao, Y. Plasmonic Detection of Mercury via Amalgamation on Gold Nanorods Coated with PEG-Thiol. *ACS Appl. Nano Mater.* **2021**, *4* (2), 1654–1663. https://doi.org/10.1021/acsanm.0c03134.

(115) Fathi, F.; Jalili, R.; Amjadi, M.; Rashidi, M.-R. SPR Signals Enhancement by Gold Nanorods for Cell Surface Marker Detection. *Bioimpacts* **2019**, *9* (2), 71–78. https://doi.org/10.15171/bi.2019.10.

(116) Latour, R. A. The Langmuir Isotherm: A Commonly Applied but Misleading Approach for the Analysis of Protein Adsorption Behavior. *Journal of Biomedical Materials Research Part A* **2015**, *103* (3), 949–958. https://doi.org/10.1002/jbm.a.35235.

(117) Kelly, K. L.; Coronado, E.; Zhao, L. L.; Schatz, G. C. The Optical Properties of Metal Nanoparticles: The Influence of Size, Shape, and Dielectric Environment. *J. Mater. Chem. B* **2003**, *107* (3), 668–677.

(118) Burda, C.; Chen, X.; Narayanan, R.; El-Sayed, M. A. Chemistry and Properties of Nanocrystals of Different Shapes. *Chem. Rev* **2005**, *105* (4), 1025–1102.

(119) Zeng, J.; Zhang, Q.; Chen, J.; Xia, Y. A Comparison Study of the Catalytic Properties of Au-Based Nanocages, Nanoboxes, and Nanoparticles. *Nano Lett* **2010**, *10* (1), 30–35.

(120) Fan, F.-J.; Wu, L.; Yu, S.-H. Energetic I–III–VI2 and I2–II–IV–VI4 Nanocrystals: Synthesis, Photovoltaic and Thermoelectric Applications. *Energy & Environmental Science* **2014**, *7* (1), 190–208.

(121) Xue, J.; Zhou, Z.-K.; Wei, Z.; Su, R.; Lai, J.; Li, J.; Li, C.; Zhang, T.; Wang, X.-H. Scalable, full-colour and controllable chromotropic plasmonic printing. *Nature Communications* **2015**, *6* (1), 8906.

(122) Bian, P.; Zhou, J.; Liu, Y.; Ma, Z. One-Step Fabrication of Intense Red Fluorescent Gold Nanoclusters and Their Application in Cancer Cell Imaging. *Nanoscale* **2013**, *5* (13), 6161–6166.

(123) Zhang, X.; Xiao, X.; Dai, Z.; Wu, W.; Zhang, X.; Fu, L.; Jiang, C. Ultrasensitive SERS Performance in 3D "Sunflower-like" Nanoarrays Decorated with Ag Nanoparticles. *Nanoscale* **2017**, *9* (9), 3114–3120.

(124) Khoury, C. G.; Vo-Dinh, T. Gold Nanostars For Surface-Enhanced Raman Scattering: Synthesis, Characterization and Optimization. *J. Phys. Chem. C* **2008**, *112* (48), 18849–18859.

(125) Jin, R.; Charles Cao, Y.; Hao, E.; Métraux, G. S.; Schatz, G. C.; Mirkin, C. A. Controlling Anisotropic Nanoparticle Growth through Plasmon Excitation. *Nature* **2003**, *425* (6957), 487–490.

(126) Fan, Z.; Bosman, M.; Huang, X.; Huang, D.; Yu, Y.; Ong, K. P.; Akimov, Y. A.; Wu, L.; Li, B.; Wu, J.; Huang, Y.; Liu, Q.; Eng Png, C.; Lip Gan, C.; Yang, P.; Zhang, H. Stabilization of 4H Hexagonal Phase in Gold Nanoribbons. *Nature Communications* **2015**, *6* (1), 7684.

(127) Zhang, C. -y; Lu, Y.; Zhao, B.; Hao, Y. -w; Liu, Y. -q. Facile Fabrication of Ag Dendrite-Integrated Anodic Aluminum Oxide Membrane as Effective Three-Dimensional SERS Substrate. *Appl. Surf. Sci* **2016**, *377*, 167–173.

(128) Jasuja, K.; Berry, V. Implantation and Growth of Dendritic Gold Nanostructures on Graphene Derivatives: Electrical Property Tailoring and Raman Enhancement. *ACS Nano* **2009**, *3* (8), 2358–2366.

(129) Ding, Y.; Chen, M.; Erlebacher, J. Metallic Mesoporous Nanocomposites for Electrocatalysis. *J. Am. Chem. Soc* **2004**, *126* (22), 6876–6877.

(130) IOST, R. M.; MARTINS, M. V. A.; CRESPILHO, F. N. Dendritic Gold Nanoparticles Towards Transparent and Electroactive Electrodes. *Anais da Academia Brasileira de Ciências* **2019**, 91.

(131) Pan, M.; Sun, H.; Lim, J. W.; Bakaul, S. R.; Zeng, Y.; Xing, S.; Wu, T.; Yan, Q.; Chen, H. Seeded Growth of Two-Dimensional Dendritic Gold Nanostructures. *Chem. Commun* **2012**, *48* (10), 1440–1442.

(132) Bai, X.; Zheng, L. A Facile Synthesis of Two-Dimensional Dendritic Gold Nanostructures at the Air/Water Interface. *Crystal Growth & Design* **2010**, *10* (11), 4701–4705.

(133) Shin, Y.; Lee, C.; Yang, M.-S.; Jeong, S.; Kim, D.; Kang, T. Two-Dimensional Hyper-Branched Gold Nanoparticles Synthesized on a Two-Dimensional Oil/Water Interface. *Scientific Reports* **2014**, *4* (1), 6119.

(134) Wang, X.; Yang, D.; Chen, L.; Liu, B.; Teng, Z.; He, N.; Wang, Z. 2D Dendritic Gold Nanostructures Formed on Silica Nanosheets: Transferability, Clean Surface, and Their Biomedical Application. *Particle & Particle Systems Characterization* **2018**, *35* (10).

(135) Ding, H.-P.; Wang, M.; Chen, L.-J.; Fan, W.; Lee, Y.-I.; Qian, D.-J.; Hao, J.; Liu, H.-G. Gold Hierarchical Nanostructures Formed at the Solid/Liquid Interfaces via Electroless Deposition and Their SERS Properties. *Colloids and Surfaces A: Physicochemical and Engineering Aspects* **2011**, *387* (1), 1–9.

(136) Huang, T.; Meng, F.; Qi, L. Controlled Synthesis of Dendritic Gold Nanostructures Assisted by Supramolecular Complexes of Surfactant with Cyclodextrin. *Langmuir* **2010**, *26* (10), 7582–7589.

(137) Wang, W.; Han, Y.; Gao, M.; Wang, Y. Facile Synthesis of Two-Dimensional Highly Branched Gold Nanostructures in Aqueous Solutions of Cationic Gemini Surfactant. *CrystEngComm* **2013**, *15* (14), 2648–2656.

(138) Wu, H.-L.; Chen, C.-H.; Huang, M. H. Seed-Mediated Synthesis of Branched Gold Nanocrystals Derived from the Side Growth of Pentagonal Bipyramids and the Formation of Gold Nanostars. *Chem. Mater* **2009**, *21* (1), 110–114.

(139) Li, J.; Wu, J.; Zhang, X.; Liu, Y.; Zhou, D.; Sun, H.; Zhang, H.; Yang, B. Controllable Synthesis of Stable Urchin-like Gold Nanoparticles Using Hydroquinone to Tune the Reactivity of Gold Chloride. *J. Phys. Chem. C* **2011**, *115* (9), 3630–3637.

(140) Jiang, C.; Markutsya, S.; Tsukruk, V. V. Collective and Individual Plasmon Resonances in Nanoparticle Films Obtained by Spin-Assisted Layer-by-Layer Assembly. *Langmuir* **2004**, *20* (3), 882–890.

(141) Frens, G. Controlled Nucleation for the Regulation of the Particle Size in Monodisperse Gold Suspensions. *Nature Physical Science* **1973**, *241* (105), 20–22.

(142) Ballarin, B.; Cassani, M. C.; Tonelli, D.; Boanini, E.; Albonetti, S.; Blosi, M.; Gazzano, M. Gold Nanoparticle-Containing Membranes from in Situ Reduction of a Gold(III)−Aminoethylimidazolium Aurate Salt. *J. Phys. Chem. C* **2010**, *114* (21), 9693–9701.

(143) Viswanath, B.; Kundu, P.; Halder, A.; Ravishankar, N. Mechanistic Aspects of Shape Selection and Symmetry Breaking during Nanostructure Growth by Wet Chemical Methods. *J. Phys. Chem. C* **2009**, *113* (39), 16866–16883.

(144) Xia, H.; Bai, S.; Hartmann, J.; Wang, D. Synthesis of Monodisperse Quasi-Spherical Gold Nanoparticles in Water via Silver(I)-Assisted Citrate Reduction. *Langmuir* **2010**, *26* (5), 3585–3589.

(145) Ansari, J. R.; Singh, N.; Ahmad, R.; Chattopadhyay, D.; Datta, A. Controlling self-assembly of ultra-small silver nanoparticles: Surface enhancement of Raman and fluorescent spectra. *Opt. Mater* **2019**, *94*, 138–147.

(146) Barabasi, A.-L.; Albert, R.; Albert. R.: Emergence of Scaling in Random Networks. *Science* **1999**, *286*, 509–512.

(147) Barabási, A.-L.; Vicsek, T. Tracing a Diffusion-Limited Aggregate: Self-Affine versus Self-Similar Scaling. *Physical Review A* **1990**, *41* (12), 6881–6883.

(148) Witten, T. A.; Sander, L. M. Diffusion-Limited Aggregation. *Physical Review B* **1983**, *27* (9), 5686–5697.

(149) Witten, T. A.; Sander, L. M. Diffusion-Limited Aggregation, a Kinetic Critical Phenomenon. *Phys. Rev. Lett* **1981**, *47* (19), 1400–1403.

(150) Sirajuddin, M.; A., T.; J., A. A.; Nafady, A.; Lee, C.-Y.; Bond, A. M.; O'Mullane, A. P.; Bhargava, S. K. The Formation of Gold Nanoparticles Using Hydroquinone as a Reducing Agent through a Localized PH Change upon Addition of NaOH to a Solution of HAuCl4. *Colloids and Surfaces A: Physicochemical and Engineering Aspects* **2010**, *370* (1), 35–41.

(151) Malel, E.; Mandler, D. Localized Electroless Deposition of Gold Nanoparticles Using Scanning Electrochemical Microscopy. *J. Electrochem. Soc* **2008**, *155* (6), 459–467.

(152) Tyagi, H.; Kushwaha, A.; Kumar, A.; Aslam, M. A Facile PH Controlled Citrate-Based Reduction Method for Gold Nanoparticle Synthesis at Room Temperature. *Nanoscale Research Letters* **2016**, *11* (1), 362.

(153) Hau, N.; Yang, P.; Liu, C.; Wang, J.; Lee, P.-H.; Feng, S.-P. Aminosilane-Assisted Electrodeposition of Gold Nanodendrites and Their Catalytic Properties. *Scientific Reports* **2017**, *7*, 39839.

(154) Lin, T.-H.; Lin, C.-W.; Liu, H.-H.; Sheu, J.-T.; Hung, W.-H. Potential-Controlled Electrodeposition of Gold Dendrites in the Presence of Cysteine. In *Chemical communications*; Cambridge, England, 2011; Vol. 47, pp 2044–2046.

(155) Draine, B. T.; Flatau, P. J. Discrete-Dipole Approximation For Scattering Calculations. *J. Opt. Soc. Am. A* **1994**, *11* (4), 1491–1499.

(156) Sheng, C.; Pengyu, X.; Yue, L.; Junfei, X.; Song, H.; Weihui, O.; Yaping, D.; Weihai, N. Rapid Seedless Synthesis of Gold Nanoplates with Micro-Scaled Edge Length in a High Yield and Their Application in SERS. *Nano-Micro Letters* **2016**, *8*, 3.

(157) Nie, S.; Emory, S. R. Probing Single Molecules and Single Nanoparticles by Surface-Enhanced Raman Scattering. *Science* **1997**, *275* (5303), 1102–1106.